

https://dspace.org/

A magnetic nanowire platform for site specific treatment of testicular cancer

Nana, Abu Bakr Ahmed

2022

https://hdl.handle.net/10539/34257

Downloaded from a DSpace repository. https://dspace.org/

A Magnetic Nanowire Platform for Site Specific Treatment of Testicular Cancer

Abu Bakr Ahmed Nana

A dissertation submitted to the Faculty of Health Sciences, University of the Witwatersrand, in fulfilment of the requirements for the degree Master of Pharmacy.



Supervisors:

Professor Yahya E. Choonara
University of the Witwatersrand, Department of Pharmacy and Pharmacology, Johannesburg, South Africa

Associate Prof. Thashree Marimuthu
University of the Witwatersrand, Department of Pharmacy and Pharmacology, Johannesburg, South Africa

Associate Prof. Pierre P. D. Kondiah
University of the Witwatersrand, Department of Pharmacy and Pharmacology, Johannesburg, South Africa

Professor Lisa C. Du Toit
University of the Witwatersrand, Department of Pharmacy and Pharmacology, Johannesburg, South Africa

June 2022, Johannesburg, South Africa

DECLARATION

I, Abu Bakr Ahmed Nana, declare that this dissertation is my own, unaided work. It is being submitted for the Degree Master of Pharmacy at the University of the Witwatersrand, Johannesburg. It has not been submitted before for any degree or examination at any other University.



_____

(Signature of candidate)

20th day of June 2022 in Parktown

DEDICATION

This work is dedicated to the most Merciful, who is unique in his Majesty, whom there is nothing like, the Glorified and Exalted, in fulfilment of my covenant and in search of his Devine pleasure.

PUBLICATIONS

1. Nana, A.B.A.; Marimuthu, T.; Kondiah, P.P.D.; Choonara, Y.E.; Du Toit, L.C.; Pillay, V. Multifunctional Magnetic Nanowires: Design, Fabrication, and Future Prospects as Cancer Therapeutics. *Cancers* **2019**, *11*,1956.

2. Nana A.B.A; Marimuthu T; Kumar P; Wamwangi D, Du Toit, L.C.; Kondiah P.P.D.; Choonara Y. Synthesis, Characterisation, and *in Vitro* Cytotoxicity Fe, Pt and Fe Modulated Pt Nanowires Towards Magneto-Responsive Targeted Delivery**.**

RESEARCH OUTPUTS

Abu Bakr Ahmed Nana, Yahya Essop Choonara, Thashree Marimuthu, Lisa C. Du Toit, Pierre P. D. Kondiah, Daniel Wamwangi. Design, Synthesis, and *In Vitro* Study of Magnetic Nanowires in Testicular Cancer Treatment. ***(Poster Presentation).*** *School of Therapeutic Sciences Biennial Research Day 2021*, University of the Witwatersrand, Johannesburg, South Africa, September 14th, 2021.

Abu Bakr Ahmed Nana, Yahya Essop Choonara, Thashree Marimuthu, Lisa C. Du Toit, Pierre P. D. Kondiah, Daniel Wamwangi. Design, Synthesis, and *In Vitro* Study of Magnetic Nanowires in Testicular Cancer Treatment. ***(Poster Presentation).*** *10th Annual Nanosciences Young Researchers' Symposium (NYRS-2020/21)-National*, South Africa, October 7th, and 8th 2021.

Abu Bakr Ahmed Nana, Yahya Essop Choonara, Thashree Marimuthu, Lisa C. Du Toit, Pierre P. D. Kondiah, Daniel Wamwangi. Design, Synthesis, and *In Vitro* Study of Magnetic Nanowires in Testicular Cancer Treatment. ***(Oral Presentation).*** *BRICS Symposium - International*, South Africa, October 7th, and 8th 2021.

ABSTRACT

Testicular Cancer (TC) incidence rates are projected to increase. Although contemporary treatment strategies have successfully cured patients with TC, they provide significant disadvantages which warrant the development of testicular saving treatments with decreased adverse effects. This aligns with the paradigm shift towards personalised medicine. The use of biomaterials science in nanomedicine with a focus on targeted delivery can advance the field with high impact. This research aimed to develop a magnetically targeted delivery platform composed of iron (Fe)/platinum (Pt) composite nanowires (NWs), combining the ferromagnetic behaviour of Fe with the cytotoxic activity of Pt against TC cells. In this regard magnetically active NWs for site specific treatment of TC were engineered using Pt as the model bioactive and characterized. NWs were chosen as the base archetype of this delivery platform due to the effect of the shape anisotropy of NWs on the magnetic properties of the delivery platform. Recent studies have shown that Pt is biocompatible, cytotoxic towards various cancerous cells, and has the potential to inhibit the growth of chemotherapy-resistant tumours. Pt was selected as the model bioactive due to its activity and the known susceptibility of TC to Pt based chemotherapy.

Four types of NWs viz.; Fe-NWs, Pt-NWs, Fe-coated Pt-NWs, and dual Fe-Pt NWs were synthesised using template electro-deposition in which an anodic aluminium oxide (AAO) membrane was employed. The NWs were then characterised to analyse the physical, chemical, and structural properties using high-resolution transmission electron microscopy (HRTEM), powder X-ray diffraction (XRD), raman spectroscopy, vibrating-sample magnetometry VSM, inductively coupled plasma - optical emission spectrometry (ICP-OES), and zeta potential. The bioactivity of the synthesised NWs was determined by measuring the cell viability using the XTT assay to determine biocompatibility and cytotoxicity, and interaction between the synthesised NWs and cells was investigated using phase contrast imagery.

The synthesised magnetic NWs had a high aspect ratio in terms of morphology with the desired lengths of <4µm and minimal diameter of 40-50 nm. All three Pt containing NWs displayed a polycrystalline structure as confirmed by powdered-XRD. Interestingly, single crystal Fe-NWs was confirmed by the single powdered-XRD peak at 2 θ 44.5° with Fe-NWs and Fe-coated Pt-NWs exhibited ferromagnetic behaviour which is conducive for magnetically targeted delivery. Fe-NWs displayed a large Ms of 2.2 X 10^6 A/m while Fe-coated Pt-NWs displayed a modest Ms of 21.6 X 10^3 A/m.

The utility of the synthesised NWs was analysed for their potential use as a cytotoxic agent using TC cell line (Tera-1) and mouse fibroblast (3T3). The single crystal Fe-NWs was found to be toxic to the non-cancerous 3T3 cells while the Pt-NWs, Fe-coated Pt-NWs and dual Fe-Pt NWs were found to be non-toxic to 3T3 cells but possessed dose-dependent toxicity to Tera-1 cells. The Fe/Pt composite NWs were more potent compared to pure Pt NWs. Pt-NWs had a high IC_{50} of 354 µg/mL while Fe-coated Pt-NWs and dual Fe-Pt NWs displayed an IC_{50} of 165 µg/mL and 207 µg/mL respectively.

Fe-coated Pt-NWs displayed the most promising results in the development of a magnetically targeted delivery system aimed at treating TC. The cytotoxic activity of the platform can be enhanced with the addition of stimulus such as high and low frequency alternating magnetic fields to induce hyperthermia or mechanical cell death respectively or near IR radiation to induce hyperthermia. Thus, additional in-depth studies are warranted to assess a multimodal cell death application of the synthesised NWs in addition to extensive *in vivo* studies for the assessment of the preclinical efficacy for progression of this technology.

AKNOWLEDGEMENTS

All praise and all thanks to the most Merciful, Originator of the heavens and the earth, Possessor of Majesty and Honour who has blessed me with this opportunity and has given me the strength and ability. May peace and salutation be upon his beloved, Prophet Muhammed (may peace and blessings be upon him)

I would like to express my gratitude to Prof. Yahya E. Choonara, Prof. Thashree Marimuthu, Prof. Lisa Du Toit, Prof. Pradeep Kumar, and Prof. Pierre Kondiah for their guidance, encouragement, and useful critique to this research work.

I would especially like to thank Prof. Thashree Marimuthu for her dedicated support and continuous encouragement.

My sincere gratitude, thanks and appreciation goes to my parents of which no acknowledgement can be sufficient and whose support was unyielding, and compassion was all-embracing, my siblings who were my pillars and my extended family for their never-ending prayers in my favour.

I would like to thank my colleagues who continuously assisted me irrespective of the difficulties they were facing and my heartfelt gratitude to the technical and support team at the Department of Pharmacy and Pharmacology for the time and efforts made to assist me.

I would like to thank the National Research Foundation (NRF) of South Africa for their funding of this work.

I would like to thank the Almighty yet again as without his mercy I am unable to accomplish anything.

TABLE OF CONTENTS

CHAPTER 1. INTRODUCTION AND OVERVIEW OF THE STUDY

1.1 Introduction 1
1.2 Rationale and Motivation 2
1.3 Novelty of the Study 3
1.4 Aims and Objectives 4
1.5 Overview of the Dissertation 5

CHAPTER 2. Multifunctional Magnetic Nanowires: Design, Fabrication, and Future Prospects as Cancer Therapeutics

2.1 Introduction 6
2.2 Considerations and Applications of Magnetic Nanowires for Cancer Therapeutics 8
2.2.1 Considerations of the Microenvironment of Cancerous Tissue for the Design of Magnetic Nanowire Therapeutic Systems 9
2.2.2 Cancer Therapeutic Applications Employing Magnetic Nanowires 9
2.2.2.1 The Application of Magnetic Nanowires as Magnetic Drug Targeting Agents in Cancer Therapeutics 10
2.2.2.2 The Application of Magnetic Nanowires as Hyperthermic Agents in Cancer Therapeutics 12
2.2.2.3 The Application of Magnetic Nanowires as Magnetic Actuation Agents in Cancer Therapeutics 13
2.2.3 Magnetic Multifunctional Nanowire Systems in Cancer Therapeutics 16
2.2.3.1 The Use of Magnetic Nanowire Magnetic-Chemo-Photothermal Systems in Cancer Therapeutics 17
2.2.3.2 The Use of Magnetic Nanowire Magnetic Actuation-Chemotherapeutic Systems in Cancer Therapeutics 18
2.2.3.3 The Use of Magnetic Nanowire as a Theragnostic System in Cancer 19
2.3 NW Fabrication and Synthesis of Magnetic Nanowire Drug Delivery Systems 19
2.3.1 Fabrication Methods of Magnetic Nanowires 19
2.3.1.1 Electrodeposition of Magnetic Nanowires 21
2.3.1.2 Pulsed Laser Deposition of Magnetic Nanowires 22
2.3.1.3 Other Synthetic Techniques of Magnetic Nanowires 23
2.3.2 Magnetic Properties and Advantages of Nanowires in Drug Delivery Systems 24
2.3.3 Stabilization and Functionalization of the Magnetic Nanowires 24
2.3.4 Chemotherapeutic Drug Loading and Release of Magnetic Nanowire Systems 26
2.4 Cellular Interactions and Toxicity Between Magnetic Nanowires and Cells 27
2.4.1 Cellular Internalization of Magnetic Nanowires 27
2.4.2 Cellular Toxicity of Magnetic Nanowires and Drug Loaded Magnetic Nanowires 29
2.4.3 Cellular Degradation of Magnetic Nanowires 31
2.5 Conclusions and Future Prospects 31

CHAPTER 3. Synthesis, Characterisation and Cytotoxic Evaluation of Fe NWs and Pt NWs

3.1 Introduction 33
3.2 The Concept of Magnetic Biomaterials: Magnetic Properties and Hysteresis 34
3.2.1 Magnetism 34
3.2.2 Magnetic Properties of Biomaterials 35
3.2.3 Magnetic Properties of NWs 38
3.2.4 Magnetic Hysteresis 38
3.3 Process of Electrodeposition 41
3.4 Experimental Setup for Electrodeposition 44
3.5 Rationale for Selecting Elemental Fe and Pt to Synthesise a Magnetic NW Advanced Delivery System 45
3.6 Basis of Cytotoxicity Studies 47
3.7 Materials and Methods 48
3.7.1 Materials 48
3.7.2 Chemical Electrodeposition Prototype for NW Synthesis 48
3.7.2.1 Synthesis of Fe NW 48
3.7.2.2 Synthesis of Pt NW 49
3.7.3 Removal of the NWs from the AAO template, storage, and preparation for cytotoxic analysis 49
3.7.4 Characterisation of the synthesised Fe NWs and Pt NWs 50
3.7.4.1 Quantification of the Synthesised NW Using ICP-OES 50
3.7.4.2 Morphological Characterisation of the Synthesised NWs 50
3.7.4.3 Quantification of the surface charge of the synthesised NWs 50
3.7.4.4 Determination of the Crystalline Properties of the Synthesised NWs 51
3.7.4.5 Determination of the Outer Surface Composition of the Synthesised NWs 51
3.7.4.6 Characterisation of the Magnetic Properties of the Synthesised NWs 51
3.7.4.7 Evaluation of the Biocompatibility, Cytotoxicity, and Cellular Internalisation of Fe NWs and Pt NWs 51
3.8 Results and Discussion 53
3.8.1 Synthesis, Morphological Analysis, and Stability of Fe NWs 56
3.8.2 Synthesis, Morphological Analysis, and Stability of Pt NWs. 60

3.8.3 Analysis of the Crystalline Structure, Crystallite Size and Interplanar Spacing of Fe NWs and Pt NWs Using Powder XRD 64
3.8.4 Analysis of the Outer Surface Composition of Fe NWs and Pt NWs Using Raman Spectroscopy 67
3.8.5 Evaluation of the Magnetic Properties and MTD Potential of Fe NWs and Pt NWs Using VSM 68
3.8.6 Cytotoxicity and Cellular Internalisation of the Synthesised NW Platforms 70
3.8.6.1 Cytotoxicity of NW Platforms on Mouse Fibroblasts 70
3.8.6.2 Cytotoxicity Assessment of the Synthesised NWs 72
3.9 Concluding Remarks 74

CHAPTER 4. Modulation of Fe NWs and Pt NWs to enable multifunctionality through the Development of Fe/Pt Composite NWs

4.1 Introduction 75
4.2 Basis for the Synthesis of Regular and Modified NWs Using Template Electrodeposition as Established in the Literature 76
4.3 Methods and Materials 77
4.3.1 Materials 77
4.3.2 Synthesis of Fe coated Pt NW 77
4.3.2.1 Step One of Fe Coated Pt NW Synthesis: Deposition of Pt into the Channels of the AAO Template 78
4.3.2.2 Step Two of Fe Coated Pt NW Synthesis: Pore Widening of the AAO Template Nanopores with Deposited Pt 78
4.3.2.3 Step Three of Fe Coated Pt NW Synthesis: Deposition of Fe in the Space Created During the Pore Widening Step 78
4.3.3 Synthesis of Alloy Fe-Pt NW 78
4.3.4 Release of the Synthesised Fe/Pt Composite NW Platforms from AAO Template 79
4.3.5 Quantification of Synthesised Fe/Pt Composite NW Platforms Using ICP-OES 79
4.3.6 Morphological Characterisation of Synthesised Fe/Pt Composite NW Platforms Using TEM and HRTEM 79
4.3.7 Determination of the Crystalline Properties of the Synthesised Fe/Pt Composite NW Platforms Using Powder XRD 80
4.3.8 Determination of the Outer Surface Composition of the Synthesised Fe/Pt Composite NW Platforms Using Raman Spectroscopy 80
4.3.9 Study of the Effects of Fe Modulation on the Magnetic Properties of the Fe/Pt Composite NW Platforms Using VSM 80
4.3.10 Cytotoxicity and Cellular Internalisation Analysis of the Fe/Pt Composite NW Platforms 81
4.4 Results and Discussion 81
4.4.1 Synthesis, Morphological Analysis, and Stability of Fe Coated Pt NWs 81
4.4.2 Synthesis, Morphological Analysis, and Stability of Fe-Pt NWs 85
4.4.3 Analysis of the Crystalline Structure, Crystallite Size, and Interplanar Spacing of Fe/Pt Composite NWs Using Powder XRD 88

4.4.4 Analysis of the Outer Surface Composition of the Fe/Pt Composite NWs Using Raman Spectroscopy 90
4.4.5 Study of Magnetic Properties and Determination of MTD Suitability of Fe Coated Pt NWs and Fe-Pt NWs Using VSM 91
4.4.6 Cytotoxicity Evaluation and Cellular Internalisation of the Fe/Pt Composite NW Platforms 94
4.4.6.1 Cell Viability After Fe Coated Pt NWs and Fe-Pt NWs Treatment on Mouse Fibroblasts (3T3) to Determine Biocompatibility 95
4.4.6.2 Determination of the Suitability of Fe Coated Pt NWs and Fe-Pt NWs as a Therapeutic Agent for TC by Evaluating Cell Viability Employing Tera-1 Cells. 96
4.5 Concluding Remarks 97

CHAPTER 5. CONCLUSIONS, RECOMMENDATIONS, AND FUTURE PROSPECTS

5.1 Conclusions 98
5.2 Recommendations and Future Prospects 99

REFERENCES 101

APPENDICES 114

Appendix A: Publications 114
Appendix B: Research Outputs (Oral and Poster Presentations) 115
Appendix C: Similarity Report 118

LIST OF TABLES

Table 2.1: Overview of fabrication techniques applied for the synthesis of Magnetic NWs.. 20

Table 3.1: Critical material attributes with the corresponding critical process parameters and critical quality attributes of the synthesised NWs. 53

Table 3.2: Analyses and interpretation of obtained powder XRD diffractograms using Scherrer equation for crystallite size and Braggs law for d-value..... 66

Table 4.1: Summary of obtained XRD data and interpretation using Scherrer equation for crystallite size and Braggs law for d-value. 90

LIST OF FIGURES

Figure 2.1: Schematic showing doxorubicin loaded nanowires being internalized into the cytoplasm and releasing the drug from the pH stimuli from the endo/lysosome. Where P-gp is P-glycoprotein. Adapted with permission from Peng et al. (4). 7

Figure 2.2: Diagram showing proposed mechanism of action for magnetic actuation stimulating a magneto-mechanical cell death in the presence of an alternating magnetic field. Adapted with permission from (67). 14

Figure 2.3: (**a**) Microscopy of unfunctionalized Co nanowires (NWs) portraying a rough morphology. (**b**) Microscopy of stimuli responsive graphene oxide (GO) functionalized Co NW. (**c**) Microscopy of GO-polyethylene glycol (PEG)-functionalized Co NW. Reproduced with permission from (55). 17

Figure 2.4: Figure showing surface modifications on magnetic NWs for stabilization. (**A**) (3-aminopropyl) triethoxysilane (APTES)-coated Fe NW. (**B**) Bovine serum albumin (BSA)-coated Fe NW. Reproduced with permission from (13). Scale bars: 50 nm… 25

Figure 2.5: Cellular internalization and accumulation of magnetic NWs into cells. (**A**, **B**) Internalized Fe NW in HeLa cells. Adapted with permission from (126). Scales bars: 10 µm. 28

Figure 3.1: Summary of the basic types of magnetic behaviour in the presence (H≠0) and absence (H=0) of a magnetic field at a given orientation. Arrows represent spin orientation. Thicker spin arrows for ferromagnetic materials at H≠0 indicate a stronger magnetisation. 36

Figure 3.2: Ordering phenomenon of magnetic domains in ferromagnetic material. Domain walls are represented by the solid lines. The arrows depict the orientation of the magnetic moment. 37

Figure 3.3: Representation of a hysteresis loop typical of ferromagnetic material. Adapted from (152). 39

Figure 3.4: M-H loops of different behaviours of magnetic materials. **A)** represents diamagnetic materials, **B)** represents paramagnetic materials, **C)** represents

superparamagnetic materials, and **D)** represents ferromagnetic materials. Adapted from Contreras (153,154) 40

Figure 3.5: Image of a standard Current vs Time graph depicting the different stages of NW growth. 43

Figure 3.6: Representation of diffusion phases during NW growth within a nanopore: **A)** linear diffusion, **B)** linear diffusion with three-dimensional hemispheric diffusion front outside the nanopore, **C)** linear diffusion with planar diffusion front outside the nanopore (Adapted from Blanco et al. (159)) 44

Figure 3.7: Two-dimensional representation of the electrochemical cell setup for NW electrodeposition. **1)** Holder for AAO template, **2)** Reference electrode, **3)** Counter electrode. 45

Figure 3.8: Schematic of the longitudinal cross-section of the prototype Fe NWs depicting the layout of the core shell structure 48

Figure 3.9: Schematic of the longitudinal cross-section of the prototype Pt NW. 49

Figure 3.10: A and B) Images of preliminary NWs of inconsistent dimensions and structure synthesised during this study. Scale bar: 500 nm 55

Figure 3.11: Graph of CV analyses of electrolytic bath of Fe NWs 56

Figure 3.12: Image showing Current vs Time graph monitoring the growth of Fe NWs 57

Figure 3.13: TEM image of Fe NWs showing large length variance of Fe NWs. Scale bar: 9 µm 58

Figure 3.14: HRTEM image of Fe NWs depicting its morphology. Scale bar: 0.5 µm 58

Figure 3.15: High magnification HRTEM image showing core shell structure of Fe NWs. Scale bar: 20 nm. 59

Figure 3.16: CV analyses for electrolytic bath of Pt NWs. **A)** Pt^{4+} reduction, **B)** hydrogen evolution 60

Figure 3.17: Current vs Time graph monitoring growth of Pt NWs 61

Figure 3.18: TEM image showing length distribution of Pt NWs. Scale Bar: 10 µm. 62

Figure 3.19: HRTEM images of Pt NWs depicting the morphology of Pt NWs. Scale bar: 500 nm. 63

Figure 3.20: High magnification HRTEM image of Pt NWs showing the polycrystalline nature of Pt NWs. Scale bar: 20 nm. 64

Figure 3.21: Powder XRD diffractograms of Fe NWs and Pt NWs embedded in AAO template. **(A)** Fe NWs**, (B)** Pt NWs..... 65

Figure 3.22: Raman spectrums of the initial scan of Fe NWs with a high laser power, Fe NWs, a reference scan for heating magnetite with a laser, magnetite, and haematite. 67

Figure 3.23: Normalised M-H Loop of Fe NWs with the long axis of the NW parallel and transverse to the direction of the applied field. 69

Figure 3.24: Normalised M-H Loop of Pt NWs with the long axis of the NW parallel and transverse to the direction of the applied field. 69

Figure 3.25: % cell viability of 3T3 cells **A)** after 24 hrs treatment with Fe NWs, **B)** after 48 hrs treatment with Fe NWs, **C)** after 24 hrs treatment with Pt NWs, **D)** after 48 hrs treatment with Pt NWs..... 70

Figure 3.26: Phase contrast images of 3T3 cells after **A)** 48 hrs treatment with Fe NWs, **B)** 48 hrs treatment with Pt NWs. Scale bar: 20 µm 72

Figure 3.27: % cell viability of Tera-1 cells **A)** after 24 hrs treatment with Fe NWs, **B)** after 84 hrs treatment with Fe NWs, **C)** after 24 hrs treatment with Pt NWs, **D)** after 48 hrs treatment with Pt NWs. 73

Figure 3.28: Phase contrast images of Tera-1 cells after **A)** 48 hrs treatment with Fe NWs, **B)** 48 hrs treatment with Pt NWs. Scale bar: 20 µm 74

Figure 4.1: Schematic of the longitudinal cross-section of the prototype Fe coated Pt NWs depicting the layout of the core shell structure 78

Figure 4.2: Schematic of the longitudinal cross-section of the prototype Fe-Pt NWs depicting the layout of the core shell structure 79

Figure 4.3: Image of Current vs Time graph monitoring the growth of Pt in the nanopores of the AAO template. 81

Figure 4.4: SEM image showing surface view of AAO template **A)** after Pt deposition, **B)** after controlled AAO dissolution for nanopore widening. Scale bar: **A)** 200nm, **B)** 200nm. 82

Figure 4.5: Image of Current vs Time graph monitoring the growth of Fe coating the Pt NWs in the widened nanopores of the AAO template. 83

Figure 4.6: Image of **A)** HRTEM, **B)** TEM; low magnification images of Fe coated Pt NWs showing its morphology and length distribution. Scale Bar: **A)** 0.5 µm, **B)** 10 µm (red scale bar) 83

Figure 4.7: Image of **A)** HRTEM, **B)** TEM; high magnification images of Fe coated Pt NWs showing its morphology, outer oxide layer, core shell and polycrystalline structure. Scale bar: **A)** 20 nm **B)** 20 nm (red bar)..... 84

Figure 4.8: A) TEM image where EDX spectrum was taken for Fe coated Pt NWs, **B)** EDX spectrum of Fe coated Pt NWs showing the presence of Pt, Fe, and O from Fe coated Pt NWs and C and Cu from the grid used in sample preparation. 85

Figure 4.9: Current vs Time graph monitoring the growth of Fe-Pt NWs in the nanopores of the AAO template. 86

Figure 4.10: A) HRTEM, **B)** TEM; low magnification images of Fe coated Pt NWs showing its morphology and length distribution. Scale bar: **A)** 500 nm, **B)** 10 µm. 87

Figure 4.11: High magnification HRTEM image of Fe-Pt NWs showing its morphology, outer oxide layer, core shell and polycrystalline structure. 88

Figure 4.12: Image showing powder XRD diffractogram obtained for **A)** Fe coated Pt NWs and **B)** Fe-Pt NWs. 89

Figure 4.13: Raman spectrum obtained for Fe coated Pt NWs and Fe-Pt NWs..... 91

Figure 4.14: M-H loop of Fe coated Pt NWs within the AAO template in the parallel and transverse orientation. 93

Figure 4.15: M-H loop of Fe coated Pt NWs within the AAO template in the parallel and transverse orientation. 94

Figure 4.16: % cell viability of 3T3 cells treated with Fe coated Pt NWs and Fe-Pt NWs after **A)** 24 hrs, **B)** 48 hrs. 95

Figure 4.17: % cell viability of Tera-1 cells treated with Fe coated Pt NWs and Fe-Pt NWs after **A)** 24 hrs, **B)** 48 hrs. 96

Figure 4.18: Phase contrast images of Tera-1 cells after **A)** 48 hrs treatment with Fe NWs, **B)** 48 hrs treatment with Pt NWs. Scale bar: **A)** 20 µm, **B)** 20 µm 97

LIST OF EQUATIONS

Equation 3.1: Equation showing the relation between B, H and M. 34

Equation 3.2: Equation defining volume susceptibility. 35

Equation 3.3: Equation for the calculation of % Cell Viability 53

Equation 3.4: Bragg's equation used to calculate d spacing: 65

Equation 3.5: Scherrer equation used for the calculation of crystallite size: 66

LIST OF ABBREVIATIONS

TC	Testicular Cancer
NW	Nanowire
EPR	Enhanced Permeation and Retention
MTD	Magnetic Targeted Delivery
HRTEM	High Resolution Transmission Electron Microscopy
TEM	Transmission Electron Microscopy
SEM	Scanning Electron Microscopy
XRD	X-Ray Diffraction
EDX	Energy-Dispersive X-Ray Spectroscopy
NWs	Nanowires
PVA	Polyvinyl Alcohol
GO	Graphene Oxide
PEG	Polyethylene Glycol
RF	Radio Frequency
DOX	Doxorubicin
BSA	Bovine Serum Albumin
APTES	(3-aminopropyl) triethoxysilane (APTES)
MRI	Magnetic Resonance Imaging
PLD	Pulsed Laser Deposition
ICP-MS	Inductively Coupled Plasma Mass Spectrometry
B	Magnetic Field
H	Magnetic field strength
M	Magnetisation
X	Magnetic Susceptibility
M_R	Remnant Magnetisation
M_s	Magnetic Saturation
Hc	Coercivity
AAO	Anodic Aluminium Oxide
CV	Cyclic Voltammetry
ALD	Atomic Layer Deposition
ICP-OES	Inductively Coupled Plasma - Optical Emission Spectrometry
MMU	Microscopy and Microanalysis Unit
VSM	Vibrating Sample Magnetometer
PBS	Phosphate Buffered Saline

CHAPTER 1.
INTRODUCTION AND OVERVIEW OF THE STUDY

1.1 Introduction

Testicular cancer (TC) is a common malignancy in reproductively aged men (1). The incident rates for TC have increased over the past few years and is likely to continue increasing as suggested by Park *et al.* (2). TC patients have high survival rates, with five-year survival rates being ≥95% (2).

Although there is a high survival rate, there is a need to improve treatment techniques of TC. The current treatments of TC comprise of the removal of the spermatic cord and testicle, retroperitoneal lymph node dissection, removal of metastatic lesions surgically, and chemotherapy or radiotherapy depending on the tumour (3–5). These treatments are major contributors to long and short term sequelae including male infertility (6,7).

A pertinent area of concern is that although orchiectomy during standard treatment is a viable option for most patients with TC, it can be impractical for patients with bilateral testicular tumours or in patients with only a singular testis. Orchiectomy creates both psychological and physical issues for TC survivors. The testes possess a symbolic nature, the loss of which, results in emotional distress and feelings of inadequacy, loss, or shame (8,9). TC survivors also have an apparent reduction of masculinity (8). The physical concerns of long-term TC survivors experienced include decreased libido, feeling less attractive, erectile dysfunction and problems with ejaculation (10).

To combat this challenge, a multifunctional magnetic nanowire (NW) platform centring on magnetically targeted delivery and selective cytotoxicity was developed and characterised. NWs were chosen for this study due to their inherent advantages and widespread applications of which its use in cancer therapeutics is of particular interest (11–13). Magnetic NWs have been studied to enhance magnetic targeted delivery, transportation of chemotherapeutic drugs and to induce magnetic hyperthermia (14–16). Compared to nanoparticles, NWs provide larger surface areas and greater magnetic moments due to its shape anisotropy which is advantages to magnetic targeted delivery (12).

Pt nanoparticles are comparatively new agents in cancer therapy which have shown intrinsic cytotoxicity against cancerous tissue (17). This cytotoxicity of Pt nanoparticles is caused

through strand breaks in the chromosomal DNA ultimately leading to the inhibition of cell replication and apoptosis (17).

This study focuses on improving targeted delivery via iron (Fe)/platinum (Pt) composite NWs as a platform for future targeted drug delivery systems to be engineered for patient-centric treatment options. The addition of functionalities such Magnetic Resonance Imaging (MRI), photothermal therapy, magnetic actuation and magnetic hyperthermia was kept in mind as future applications on this novel platform.

Targeted drug delivery involves the transportation of a drug to the required site of action increasing the concentration of the active at the required site. Traditional targeted delivery systems include active and passive targeted delivery systems and are instrumental in the rapidly developing paradigm shift to personalised medicine (18). Active targeting of tumour cells using nanotechnology is achieved by attaching a molecule to a nanoparticle carrying an active drug, that has selective interactions to surface structures on the targeted tumour cell. This is done to allow for the selective uptake of the targeted delivery system into the target cell allowing the target cell direct access to the required drug. The downside of this approach is that this selectivity works at a microscale. The targeted delivery system needs to be within 0.5 nm of the target cell for the attached molecule to interact with the target cell (19). Passive targeting of tumour cells involves the use of tumour vasculature. The tumour vasculature is comprised of convoluted and immature vessels that are defined by a disordered, irregular structure and morphology. Passive targeting takes advantage of the disorder of the tumour vessels, compromised integrity of the basement membrane and discontinuous endothelial lining to allow for the penetration of large molecules and nanoparticles independent of their characteristics through the blood-tissue barrier and accumulate in the tumour tissue. This phenomenon is called the Enhanced Permeability and Retention effect (EPR effect) and was first described by Y. Matsumura and H.A. Maeda (20). The EPR effect is well manifested in fast-growing experimental tumours in animals. However, this has not been successfully translated for all human solid tumours (21).

1.2 Rationale and Motivation

Magnetic Targeted delivery (MTD) has the potential to improve targeted delivery systems by allowing the tumour to be actively targeted, providing a testis-saving treatment option. MTD is a physical method of targeting rather than receptor-based and is cantered on transporting magnetic nanoparticles with loaded actives to the tumour site utilizing an external magnetic field (22). MTD treatment is ideal for localised diseases such as cancerous tumours. In MTD, the magnetic platform is injected at an appropriate site in the bloodstream for transportation to

the blood supply of the diseased tissue. External magnetic fields are then used to extract the MTD platforms from the bloodstream and conducted towards the tumorous tissue. This is advantages in the treatment of testicular cancer tumours as direct injection to the testis could lead to the production of anti-sperm antibodies and fibrosis leading to a decrease in fertility (23). The externally applied magnetic field possesses an advantage when compared to other stimuli such as ultrasound for physical targeted delivery systems with regards to its penetration depth (22,24). External magnetic fields can be safely applied with field strengths of 8 T for adults and 4 T for children (25).

The Fe/Pt composite NWs were fabricated employing electrodeposition and an anodic aluminium oxide template to control the shape, growth, and composition of the NWs. The NWs are simple to manufacture and easily reproducible using this method. The NWs were then characterised to determine their magnetic properties for their applicability as an MTD system, composition, morphology, and crystallite structure. The cytotoxicity of the NWs was analysed during *in vitro* studies using mouse embryonic fibroblasts (3T3) to simulate the effect of the NWs in noncancerous tissue and epithelial-like human testicular cells derived from germ cells (Tera-1) to simulate the cytotoxicity of the NWs against the most common histology of testicular cancer, Germ Cell Tumours.

1.3 Novelty of the Study

The novelty of this study is evident by the following points:

- Modification of the formulation of the electrolyte used in the synthesis of Fe NWs resulting in tailored composition and structural properties.
- A new method developed utilising modified template electrodeposition protocols for the fabrication of Fe coated Pt NWs and Fe-Pt NWs.
- First report on cytotoxicity studies tested on Tera-1 cells by Fe NWs, Pt NWs, Fe coated Pt NWs and Fe-Pt NWs.
- First report on cytotoxicity studies tested on 3T3 cells by Pt NWs, Fe coated Pt NWs and Fe-Pt NWs.
- New knowledge generation on the physicochemical properties of the synthesised Fe NWs, Pt NWs; and the Fe/Pt composite NWs: Fe coated Pt NWs and Fe-Pt NWs.

1.4 Aims and Objectives

This research sought to engineer and synthesise Fe/Pt composite NWs that will combine the ferromagnetic behaviour of Fe with the cytotoxic activity of Pt against testicular cancer cells (Tera-1). NWs of various compositions and morphologies was synthesised and evaluated to produce NWs that was suitable for MTD and possesses selective activity against testicular cancer cells while leaving the option open for the addition of multiple functionalities when tailoring the NWs to the treatment of other cancers. The research objectives were:

1) Synthesized Fe NWs, Pt NWs; and the Fe/Pt composite NWs, Fe coated Pt NW, and an alloy of Fe and Pt NW using templated assisted electrodeposition for the development of reproducible synthetic protocols.

2) Characterised the morphological structure of the NWs using high-resolution transmission electron microscopy (HRTEM) and transmission electron microscopy (TEM), and to determine the crystallographic structure of the synthesised NW platforms using powder X-ray diffraction (XRD) to establish that the NWs obtained were of expected size, shape, and structural composition.

3) Assessed the degree of oxide formation on the synthesised NWs surface employing HRTEM and Raman spectroscopy respectively to ensure that magnetism was maintained.

4) Determined the composition of the NW platforms using energy-dispersive X-ray spectroscopy (EDX) and inductively coupled plasma - optical emission spectrometry (ICP-OES) to confirm the successful synthesis and ascertain the exact concentration of the synthesised NWs for *in vitro* studies.

5) Performed *in vitro* studies with the NW platforms to determine cellular internalisation and cell cytotoxicity against 3T3 and Tera-1 to establish the effectiveness of the systems as cytotoxic agents in the treatment of TC.

1.5 Overview of the Dissertation

Chapter 1 of this dissertation presents a succinct introduction and background to the challenges faced in the treatment of testicular cancer. An innovative solution addressing the identified challenges using MTD, namely, the Fe/Pt composite NWs, is then defined, and expounded upon. To conclude the chapter, the aims and objectives of this research are summarised and elucidated.

Chapter 2 of this dissertation presents a comprehensive examination of multifunctional magnetic NWs in the use of biomedical applications. This review explores the approaches taken by researchers to combat the challenges experienced in cancer therapeutics with a focus on magnetic NWs and the functionalities added to them conforming with the paradigm shift towards patient-centric precision medicine.

Chapter 3 of this dissertation presents a background and pre-formulation study. A basic background of important magnetic concepts in this research is provided. Then template electrodeposition, the technique chosen to synthesise the NW platforms is explained and justified. The design of the experimental setup is explained and presented. Lastly, the chapter focuses on the design, synthesis, and characterisation of Fe NWs and Pt NWs. The composition, morphology, crystalline structure, and magnetic properties are explored in detail. The cytotoxic activity is evaluated against a cell line derived from human TC germ cell tumour and a non-cancerous cell line.

Chapter 4 of this dissertation presents the design, synthesis, and characterisation of two versions of Fe/Pt composite NWs. The novel synthesis method of a core-shell Pt NW enclosed in a Fe nanotube employing a modification of the well-studied, cost-effective template electrodeposition is described. The composition, morphology, and crystalline structure of the Fe/Pt composite NWs are explored. The cytotoxic activity and magnetic properties of the Fe/Pt composite NWs are evaluated for its potential application as a selectively active MTD platform for the treatment of TC.

Chapter 5 of this dissertation examines the suitability of the synthesised Fe/Pt composite NW platforms developed in the treatment of TC. Future recommendations on additional functionalities incorporated into the synthesised NW platforms are discussed for the potential application in localised diseases.

CHAPTER 2.
Multifunctional Magnetic Nanowires: Design, Fabrication, and Future Prospects as Cancer Therapeutics

2.1 Introduction

Cancer is amongst the most pernicious diseases known, due to the high mortality and incidence rates reported (26).Traditional treatment such as chemotherapy, radiation therapy, and surgery has provided successful treatment and control of cancer to a certain extent (27). However, each approach comes with its own difficulties, notably being invasive or unspecific in its killing effect leading to grave adverse effects. Alternative therapies such as carbon ion therapy and proton therapy are more specific and carries a lower side effect risk when compared to X-ray radiotherapy. The limitation of these therapies is that they require specialized equipment and personnel, thus resulting in high cost and constrained treatment accessibility (28). Chemotherapy, when looked at in isolation, has further shortcomings such as short half-life, acquired drug resistance, nonspecific bio-distribution in cells and tissues, rapid metabolism, and excretion. This leads to a low therapeutic index due to the destruction of healthy cells and potent toxicity (26).

Multifunctional nanosystems has been of recent interest in anti-cancer-therapy for the purpose of developing safe, effective, and efficacious drug delivery systems, due to the potential of overcoming the disadvantages of traditional strategies. Amongst the most promising multifunctional nanosystems include the use of magnetic drug targeting, actuation, or hyperthermia in amalgamation with triggered drug release strategies as well as their combination with diagnostic methods such as MRI and fluorescence imaging. This can lead to a theragnostic approach personalizing cancer treatment for patients. Amongst the various nanoparticles and nanocarriers that multifunctional nanosystems are comprised of, nanowires (NWs) are of key interest due to their shape anisotropy and large surface area. **Figure 2.1** shows a NW system, in which stimuli release the drug in the presence of a decreased pH after cellular internalization.

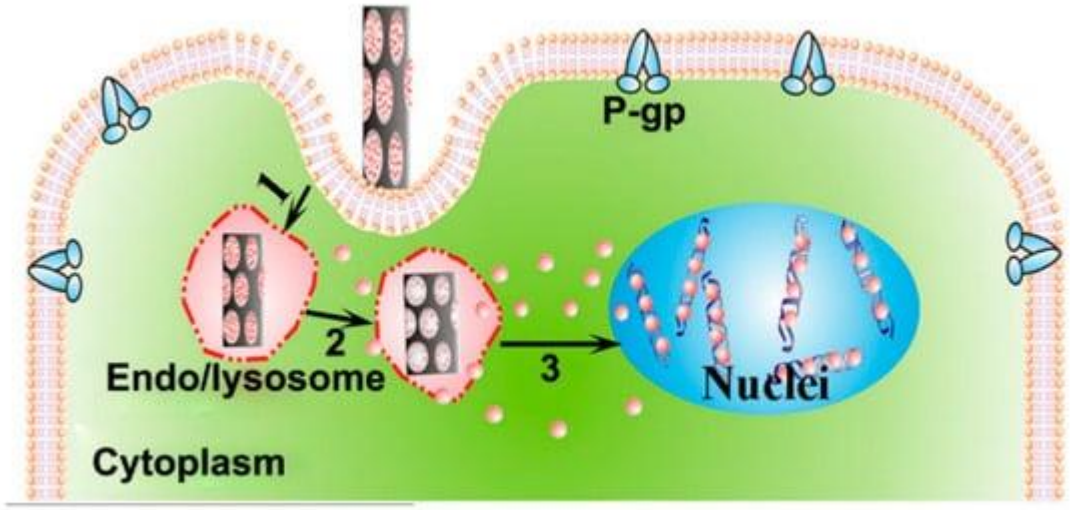


Figure 2.1: Schematic showing doxorubicin loaded nanowires being internalized into the cytoplasm and releasing the drug from the pH stimuli from the endo/lysosome. Where P-gp is P-glycoprotein. Adapted with permission from Peng et al. (4).

NWs have widespread applications in various fields including drug delivery (29), sensors (30), biomedicine (31), water purification (32), magnetic storage (33), and electronics (34). NW application in drug delivery includes the use in both targeted drug delivery systems such as magnetically responsive platforms (13,22) and triggered release systems such as pH responsive systems (35). NWs are also used to induce non-chemotoxic cell death by using magnetic actuation and induced localized hyperthermia in the presence of an alternating magnetic field.

NW are structurally characterized as one-dimensional geometry, involving large lengths reaching micrometre range and small diameters in the nano-range (~10–200 nm). Their length-to-diameter ratio (aspect ratio) is usually large (36), which differentiates them from nanorods.

These intrinsic properties of NW provide specific advantages in terms of drug delivery, which is of particular interest with regards to cancer therapeutics, such as a large surface-area-to-volume ratio and increased biocompatibility by its ability to camouflage and be coated with various biocompatible and biodegradable coatings (biopolymers and semi-synthetic polymers) increasing its solubility, stability, and its ability to be functionalized. NWs therefore provide an efficient platform for drug delivery systems to be based on. The large surface-area-to-volume ratio allows for greater drug loading and attachment of targeting molecules while the small

diameters provide the ability to pass through narrow capillaries (37). With regards to magnetically responsive NW, the elongated shape brings inherent advantages that can be exploited. Their anisotropic magnetic and physical properties allow for easy magnetization, greater magnetic moments when compared to spherical particles, and NWs also have large remnant magnetization. The large remnant magnetization intensifies the effectiveness and range of the magnetic interactions due to its favourable energy configuration (38), which results in magnetic navigation being able to be carried out at deeper locations inside the body (14).

There are multiple fabrication methods for synthesizing NWs. These include chemical methods, physical methods, electrodeposition, and electroless deposition (39), which use both the bottom-up and top-down approaches. In the top-down approach, which is a subtractive technique, material is carved of a larger starting material block, revealing the NW. On the other hand, the bottom-up approach is an additive-type synthesis in which smaller particles are bound together to synthesize the NW (40).

This chapter focused on design of multifunctional systems of magnetic NWs, including the fabrication methods of magnetic NWs; strategies and application of magnetic NW-based nanosystems for cancer therapeutics; characterization of the magnetic NW nanosystems including toxicity, cell internalization, drug loading, and release; and critical evaluation of the performance for NW-based multifunctional nanosystems, for improved therapeutic outcomes.

2.2 Considerations and Applications of Magnetic Nanowires for Cancer Therapeutics

In order to design effective cancer therapeutic systems, the applications of the magnetic NWs must be tailored to achieve in the appropriate microenvironment of the targeted cancer, which the therapeutic system is designed for. Thereafter, the most appropriate applications of magnetic NWs must be synergistically combined to validate the rationale of incorporating the NW into a multifunctional system. Below, the general considerations of tumour microenvironment will be discussed as well as the applications of magnetic NWs in a therapeutic system.

2.2.1 Considerations of the Microenvironment of Cancerous Tissue for the Design of Magnetic Nanowire Therapeutic Systems

Tumour microenvironments play an important role in the biological impact of nanosystems as well their distribution (41). For nanosystems to be efficacious for cancer therapeutics, it needs to attain a homogenous distribution intratumorally, however nanosystems need to overcome the tumour microenvironment's barriers, which are summarized by Fernandez and co-workers (42). Although the enhanced permeability and retention effect promotes extravasation of nanosystems intratumorally, they must first overcome the high interstitial pressure, abnormal tumour vasculature, and dense stroma, so that they may be efficacious. Explicit pathophysiological conditions of the targeted tumour, such as functional proteins and levels of amino acids, as well as endogenous factors of the tumour microenvironment must be considered in the design of optimal-nanosystems. These factors include acidosis, hypoxia, hyperthermia, oxidative stress, enzyme activity, redox potential, and high interstitial fluid pressure. However, these factors can also be exploited in the drug delivery design of nanosystems. For instance, nanosystems can be designed to take advantage of the tumour acidic environment, which differs from physiological pH to initiate drug release. This can be achieved by bonding the drug to the nanosystems using acid hydrolysis sensitive covalent bonds (43). Active targeting can also be achieved using pathophysiological conditions of the targeted tumour. This is accomplished by binding specific antibodies that bind to receptors expressed on the tumour cell such as attaching anti-Her2/neu antibody to the nanosystem, which binds to Her2/neu receptors on the tumour cell membrane. Aptamers and ligands can also be used in a similar regard (44). A promising potential application of magnetic NW drug delivery systems is the attachment of Wnt inhibitors. Traditionally, Wnt inhibitors are restricted by high toxicity and inefficient drug delivery systems (45). However, these limitations can be overcome by a targeted and stimuli-release drug delivery system, which nanotechnology, and in particular magnetic NWs, can achieve (45).

2.2.2 Cancer Therapeutic Applications Employing Magnetic Nanowires

Nanocarriers have been greatly reviewed and have shown to have great therapeutic benefits. These advantages include the ability to increase the permeation of drugs across the epithelial lining of the gut wall, half-life, and solubility of hydrophobic drugs (46,47). Nanosystems, on the other hand, are favoured due to its ability to overcome the limitations of conventional therapy. For example, being able to selectively release drug, increase accumulation in the target organ, and design a targeting ability within the nanosystems. Nanosystems also have

the capability to perform multiple roles, such as theragnostics, measuring dose response, and drug efficacy.

NWs can be integrated into such multifaceted drug delivery systems coalescing the inherent properties of NW and the efficacy of nanosystems, producing an advanced, modifiable, and functionalisable platform for drug delivery. These platforms are most commonly in a hybrid inorganic-polymer NW orientation or synthesized as a silicon core. The NW being the inorganic core while the surface coatings bring about a variety of biomedical properties. These surface coatings use various stimuli to illicit responses in a way that allows the systems to become targeted, selective, and stimulate drug release in order to increase therapeutic outcomes and decrease adverse effects of therapy.

This combination is effective in the development of drug delivery platforms for cancer treatment due to the unique merits it provides. It can enhance therapeutic effects by combating multiple drug resistance in cancers or provide a synergistic combination of therapeutic effects. This combination also allows for the accumulation of drug at the targeted tumour sites, thus reducing adverse effects of treatment (48–51).

2.2.2.1 The Application of Magnetic Nanowires as Magnetic Drug Targeting Agents in Cancer Therapeutics

Drug accumulation at specific tumour sites can be achieved when an external magnetic field is used to draw out and trap magnetically active, drug-loaded nanoparticles from the circulatory system. It is promising for its potential of increasing the saturation of drug at the required site while decreasing the saturation in healthy tissue. Thus, reducing adverse effects and increasing therapeutic outcomes. Magnetic targeting is thus dependent on two factors, a nanocarrier that is magnetically responsive and a magnetic field gradient (52). Magnet systems employed in magnetic targeting fall into two classes, the use of an external magnet and the combination of an external magnet with an implanted magnet near the target area (52). Magnetic NW systems that are delivered into the blood stream must overcome the viscous drag force of the blood stream. Therefore, the magnetic NW systems will potentially be captured from the capillary blood flow by the external magnet to the target area. The large magnetic moments of magnetic NWs reduce the field gradient required to capture the NW (14). To provide the magnetic field and magnetic field gradient, there are currently two categories of magnet systems: static field magnet systems and varying field magnet systems. Static field magnet systems are low cost, convenient, and simple but lack targeting accuracy,

while varying field magnet systems have high targeting accuracy, which make it possible for employing three dimensional (3-D) precise targeting but are energy consuming and require complex hardware systems and exact calculations (53).

Magnetic NWs have an inherent advantage over spherical nanoparticles such as superparamagnetic iron oxide nanoparticles, as the anisotropy of NW allow for deeper tumours to be targeted and have a higher drug loading capacity(22,54). Pondman et al. created an iron-palladium (FePd) NW system functionalized with oleic acid. This resulted in non-immunotoxic, non-cytotoxic delivery platform granted, unsuccessful in accumulating the NW at the target site in pilot studies. Their FePd NW dimensions were 1.9 ± 0.3 µm in length and 88 ± 15 nm in diameter resulting in an aspect ratio of 22. When a magnetic field was applied to the NW inside the template in three different directions, 0°, 45°, and 90° to the NW direction, the wires showed remanence in all three directions and when tested in random orientations, provided a saturation magnetization (M_s) ± 80 $A.m^2/kg$ and a remnant magnetization (M_R) ± 25 $A.m^2/kg$ (14). Pondman and co-workers performed *in vivo* studies using Their FePd NW on rats. No negative reactions were shown after intravenous administration with no FePd NW found in the kidneys and liver. The studies suggested a high circulation time due to the immune response and first pass filtration of the kidneys not removing the FePd NW system. However, they were not able to prove significant localization of their NW system at target site. This was likely caused by the removal of blood from the rat in the fixation process (14). Alsharif et al. iron (Fe) NW with an aspect ratio of 75 had a Fe_2O_3 layer surrounding the Fe NW and provided much larger M_s and M_R of 427 $A.m^2/kg$ and 388 $A.m^2/kg$, respectively. This confirmed its permanent magnetic properties and is indicative of its greater potential as a magnetic targeting agent when compared to the FePd NW. However, the Fe NWs will have a greater degree of aggregation, which will need to be overcome in order to be effective and safe as a drug delivery system (11). The magnetic properties of the cobalt (Co) NW and functionalized Co NW of Zhu et al. was not characterized by a magnetometer. However, its potential for providing targeted chemotherapy was shown by suspending the Co NW, GO-Co NW, and GO-PEG-Co NW in polyvinyl alcohol (PVA) solution (where GO is graphene oxide and PEG is polyethylene glycol) and placed near an external magnet. This resulted in each group being attracted to the external magnet within one minute (55)

2.2.2.2 The Application of Magnetic Nanowires as Hyperthermic Agents in Cancer Therapeutics

The use of NW as hyperthermic agents is promising due to its ability to be optimally structured to provide thermal response to stimuli such as low-frequency alternating magnetic fields and of near-infrared irradiation (56). Hyperthermia involves the energy insertion into malignant tumours resulting in the death of the cancer cells. It can be characterized into three states: diathermy (greater than 41 °C), apoptosis (between 42 °C and 46 °C), and thermoablation (greater than 46 °C). Diathermy stimulates tumour growth, apoptosis is the ideal range for cancer cell destruction, while thermoablation stimulates heat-induced necrosis (16).

There are two modes of inducing magnetic hyperthermia in the presence of an alternating magnetic field. These are the Brownian relaxation mechanism and the Néel relaxation mechanism (57). The Brownian mechanism involves the NW rotation-vibration towards the direction of the external magnetic field. This results in a mechanical friction caused by the magnetic NW in its suspended medium, inducing the hyperthermia. The Néel mechanism involves the rotation of the magnetic moment within the NW in an external magnetic field. Néel's mechanism therefore induces hyperthermia by the "internal friction" caused by the magnetic moment movement. The Néel mechanism provides a more specific cell death mechanism as it induces minor mechanical damage to cells when compared to the Brownian mechanism, which is non-selective in its mechanical damage of cell membranes. In addition, heat induced in terms of hysteresis losses is dependent on the particular reversal mechanism. This is usually mediated by the nucleation and propagation of a magnetic domain wall. The domain wall is dependent on both the specific materials and geometry and can be of two types, vortex, or transverse domain wall. The domain wall dynamics influences the heating performance of the NW and creates a certain maximum frequency in which a heating response is elicited (58). Magnetic heating has strong dependence on the magnetic properties of the magnetic NWs (59). Specific absorption rate, which is used to quantify the heating efficiency, is increased when an alternating magnetic field equal to or lower than the coercive field is applied. Therefore, metallic NWs such as Nickel (Ni) and Fe have greater heating power when compared to Co due to their coercivity. The coercive field is also influenced by the geometry of the NW. Consequently, the heating efficiency of thicker NW will be greater than that of thinner NW and longer NW will be greater than shorter NW (59,60).

The recommended frequencies of electromagnetic fields lie between 50 kHz < f < 1 MHz as physiological responses such as muscle (skeletal and peripheral) and cardiac stimulation

occur with increasing frequencies (61). Choi et al. produced Ni NWs and successfully induced hyperthermia in HEK-293 cells. This was achieved using radio frequency (RF) electromagnetic fields. The Ni NW was internalized by the cells and after the application of a RF of 810 MHz (62). Lin and co-workers fabricated Fe NW with a coercive force of about 9.7 Oe. This provided a high saturated heating temperature of 73.8 °C at a concentration of 500 ppm. During their cytotoxicity studies investigating hyperthermia derived from Fe NW, they revealed a mortality rate of 80% for EMT-6 cells. This highlights the feasibility of using Fe NW in hyperthermia therapy (57). Alonso et al. synthesized FeCo NW to study their potential in magnetic hyperthermia. They found that the Specific absorption rate increased with an increase in length and obtained remarkable specific absorption rate values of ~1500 W/g (60). Hopkins et al. produced Ni-gold (Au) core-shell NW and for RF initiated hyperthermia for thermotherapy (63). During *in vivo*, the NiAu core-shell NW was intratumorally injected into the mice. A RF of 950 MHz and power of 10 W was then applied for 30 min with the mice under injectable anaesthesia with a second and third treatment carried out at day 20 and day 30, respectively, after the first treatment. This resulted in significant damage to the malignant solid tumour on the mice.

2.2.2.3 The Application of Magnetic Nanowires as Magnetic Actuation Agents in Cancer Therapeutics

Magnetic NWs can induce cell death without a heat dependent mechanism in a magneto-mechanical process as depicted in **Figure 2.2** (64,65). The first study of magnetic actuation induced cytotoxic effects arising from alternating magnetic fields at low frequencies was studied by Zablotskii and colleagues (66). They applied a high-gradient magnetic field with a low frequency (1–10 Hz) as well as mechanical vibration on incubated mesenchymal stem cells. Their results suggested that both the mechanical vibration and alternating magnetic field played an active role in the F-actin remodelling and succeeding down-regulation of the audiogenic genes adiponectin AP2 and PPARγ.

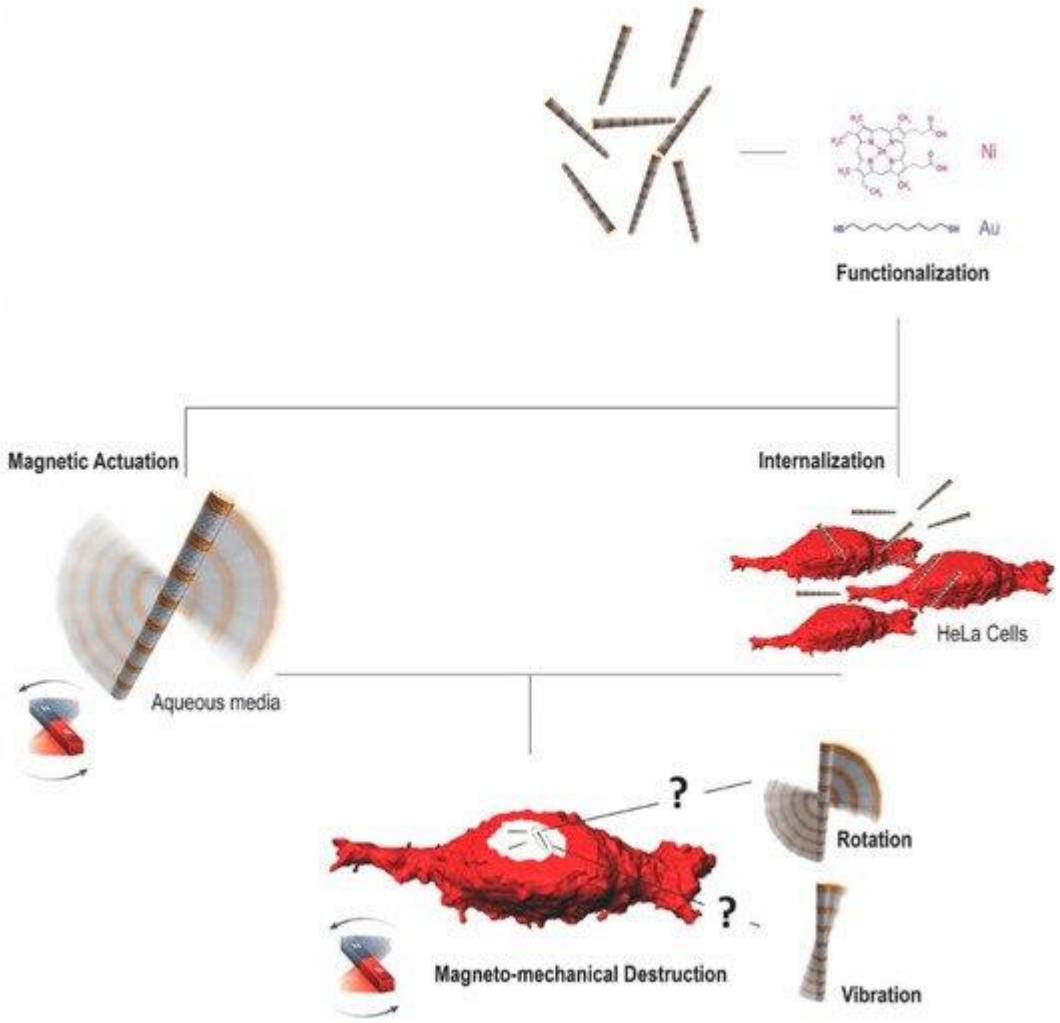


Figure 2.2: Diagram showing proposed mechanism of action for magnetic actuation stimulating a magneto-mechanical cell death in the presence of an alternating magnetic field. Adapted with permission from (67).

This mechanism was later applied to a more cancer therapeutic approach by researchers. The exemplary study of Contreras and co-workers exhibited the use of Ni NW for a non-chemotoxic approach to cancer cell death. They fabricated Ni NWs with a length 4.1 ± 1.4 µm and a diameter of 30 to 40 nm. The M_S value measured was 46.7 A.m^2/kg, which is lower than the reported literature value for bulk Ni, which is 54.3 A.m^2/kg (68). This phenomenon was associated with the surface oxidation of the Ni NW according to Contreras and co-workers. When comparing the array Ni NW to a single Ni NW, the M_S increased to 47.4 A.m^2/kg as the single Ni NW acts as a permanent magnet and is free from magnetostatic interactions, which the array experiences and thus show single domain properties (69). The behaviour of magnetic NWs is administrated by its magnetization in the presence of an alternating magnetic

field. In the case of Ni NW, it is determined by the shape anisotropy and the NW axis (magnetic easy axis) (65,70). This results in the Ni NW producing a torque when trying to align their magnetic moment with the alternating magnetic field. This mechanism is applicable for all magnetic NWs with the same characteristic. Therefore, when the NWs are exposed to an alternating magnetic field, they will experience torque, while trying to align the magnetic moment with the field. This torque results in a force being applied on the cell, which leads to its death in the presence of an alternating magnetic field as shown in **Figure 2.2**. Serrà et al. fabricated a multi-component Au/Ni–nickel oxide (NiO) NW using pulsed potentiostatic electrodeposition. They incubated the NW with HeLa cells for 24 h, after which 70% of the NW were internalized. They observed 24% cell death after an alternating magnetic field of 14 and 35 mT and 20 Hz was applied for 15 min. The segmentation of the NW assisted in tailoring the M_R, which in turn decreased the NW agglomeration, and the observed cell death was not induced by magneto-mechanical effect due to the lower M_R, but rather it was associated with the NW vibration, which further highlights the association of magnetization and NW behaviour (67).

Specific loss power (heat produced) frequency dependence is linear for ferromagnetic particles (71). Therefore, in order to produce the heat required for thermoablation, the amplitude of the alternating magnetic field necessary is ~10 kA/m and around 100 kHz frequency is required (72,73). Magnetic actuation cell deaths were induced at ranges largely below those thresholds. The Fe NW systems of Martínez-Banderas and co-workers used a 1 mT, 10 Hz alternating magnetic field to induce cell death while Contreras and co-workers used alternating magnetic fields of 0.5 mT and 0.1, 1, and 10 Hz to induce cell death. This low amplitude and frequency requirement translate into lower cost of magnetic actuation cancer treatment and increased safety of patients by reducing the risk of thermoablation (64).

This principle of inducing magneto-mechanical cell death by magnetic actuation can be applied to cancer therapeutics to induce non-chemotoxic destruction to a malignant tumour. The advantage of this is that it not only can reduce or eliminate chemotherapeutic side effects, but it can also be used as an alternative cell killing mechanism in multi-drug resistant cancer.

2.2.3 Magnetic Multifunctional Nanowire Systems in Cancer Therapeutics

The core principle behind formulating NW systems using a magnetic core is magnetic navigation (14,74,75). The ability to localize a delivery system using a non-invasive and relatively safe force is highly remunerative in cancer therapy, as it allows the progression from the limitations of traditional cancer chemotherapy by allowing therapeutic effects to be directly targeted at the tumour site, thus reducing secondary effects. In addition to magnetic navigation, magnetic NWs are used for inducing cell death by magneto-mechanical means using magnetic actuation (64) and induced local hyperthermia (76) by applying a low- and high-frequency alternating magnetic field, respectively.

Magnetic NW cores are functionalized by their surface modifications. These modifications alter the pharmacokinetics of the magnetic NW systems, adjust the cytotoxicity, allow for attachments of biomolecules such as ligands, and allow for the conjugation or entrapment of drugs (77). Surface modifications are also used to input a responsive behaviour to the system usually to provide effects such as triggered drug release or hyperthermia. The stimuli used to initiate such behaviour include a change in pH and radiation. The coalescence of the magnetic NWs and stimuli-responsive surface coatings create multifunctional magnetic NW systems that have potential advantages over traditional cancer therapy. **Figure 2.3 (a)** depicts Co NWs while **Figure 2.3 (b), (c)** depicts Co NWs with surface modifications that were designed to increase the biocompatibility, enable drug loading using electrostatic means, and provide photothermal responsiveness from a stimulus (near-infrared irradiation).

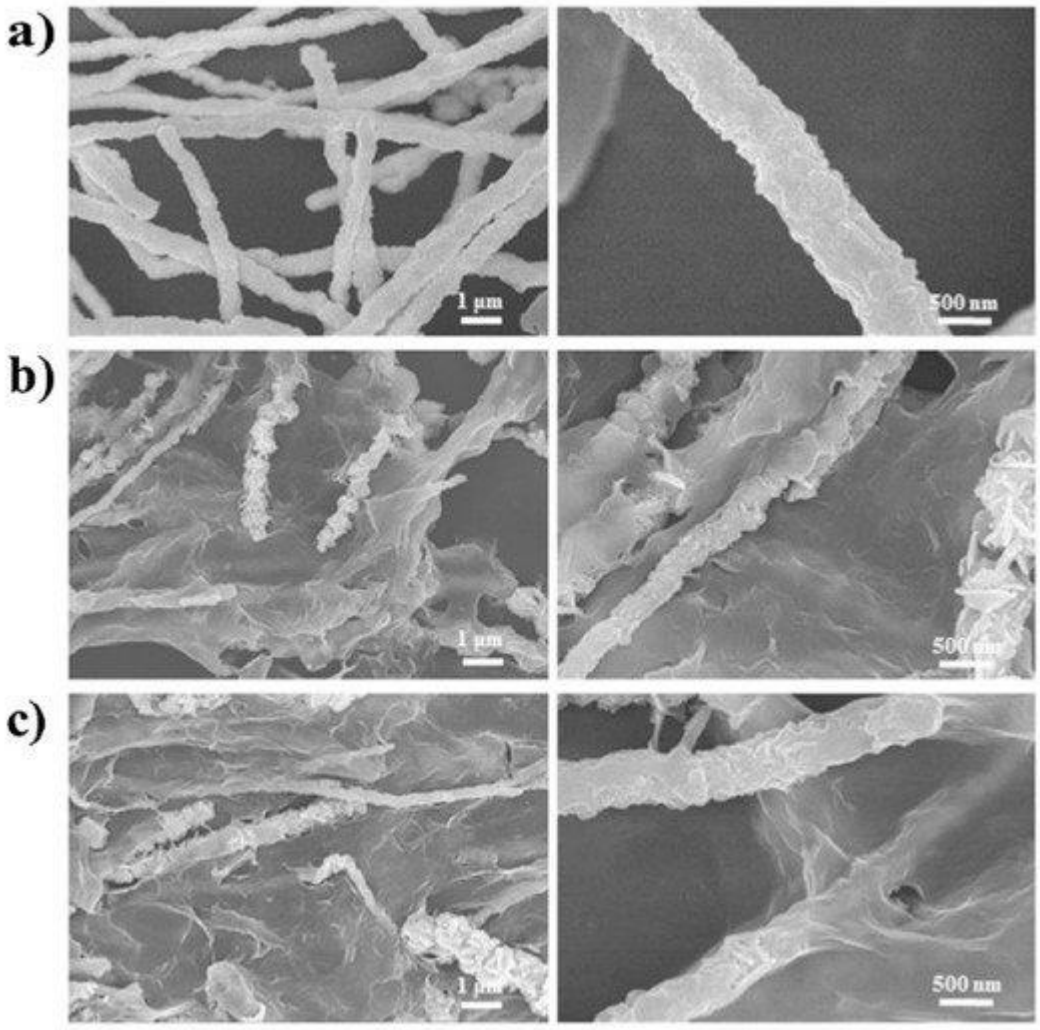


Figure 2.3: (**a**) Microscopy of unfunctionalized Co nanowires (NWs) portraying a rough morphology. (**b**) Microscopy of stimuli responsive graphene oxide (GO) functionalized Co NW. (**c**) Microscopy of GO-polyethylene glycol (PEG)-functionalized Co NW. Reproduced with permission from (55).

2.2.3.1 The Use of Magnetic Nanowire Magnetic-Chemo-Photothermal Systems in Cancer Therapeutics

The use of a multifunctional system that is magnetically targeted to deliver a chemotherapeutic load to the tumour site, in addition to inducing a local hyperthermia in the tumour to induce cell death in synergy to the chemotherapeutic drug, is advantageous for the following reasons: it decreases drug adverse and side effects, enhances the efficacy of tumour destruction, and can potentially be used to combat multi-drug resistance in chemotherapy. This approach was

explored by Zhu et al. (55). They built this multifunctional nanowire system on Co nanowires treated with GO and PEG, which provided the desired responsiveness to pH, magnetic fields, and near-infrared irradiation. A template-free reduction method was used to synthesize the CO NWs in the presence of a magnetic field. This produced unordered, irregular, and rough NWs on which the PEG and GO were coated. Three different groups were produced, namely Co NWs, Co NWs-GO, and Co NWs-GO-PEG, and were characterized by their drug loading ability, toxicity magnetic, and photothermal properties, which are discussed in the relevant sections below. They produced a system that can potentially be magnetically targeted to a tumour site, thereafter, release the loaded drug due to the combined decrease in pH at the tumour site, and an application of near-infrared irradiation, which both stimulates drug release and local hyperthermia; thus, inducing cell death by both the drug and the local temperature increase. This is a promising model; however, further studies need to be carried out to determine the *in vitro* and *in vivo* magnetic targeting ability so that this system can be phased into clinical trials.

2.2.3.2 The Use of Magnetic Nanowire Magnetic Actuation-Chemotherapeutic Systems in Cancer Therapeutics

Martínez-Banderas et al. conducted a study, which used the combined chemotherapeutic effects of doxorubicin (DOX) and mechanical disturbances, induced by a low-frequency alternating magnetic field, of their magnetic NWs to prompt cancer cell death. Their system was built upon Fe NWs with an average length of 6.4 ± 1.3 μm and a diameter of 30 to 40 nm. The Fe NWs were coated with bovine serum albumin (BSA) and (3-aminopropyl) triethoxysilane (APTES) independently and additionally functionalized with DOX. The Fe NWs were synthesized using electrodeposition and formed NWs of a monocrystaline nature. An interesting aspect of these Fe NWs was that it was found to have a 4–10 nm thick layer of iron oxide on its surface (monocrystaline Fe NW surface oxide layer caps at 10 nm) (78) as compared to completely oxidized, which occur to polycrystalline Fe NW over time. This ensures that an Fe core will remain. The oxidation most likely occurred when dissolving the template in sodium hydroxide (NaOH) as the NaOH provides very good oxidizing conditions for Fe. The Fe oxide interphase is important for two reasons. The first being that the remnant magnetizations and magnetic saturation depend on the oxide thickness. The second being it provides a site for the covalent attachment of surface coating. Martínez-Banderas and colleagues thus created a system in which cell death was caused by the cytotoxic effect of DOX and structural damage to the cells by the magneto-mechanical disturbances as shown when tested on MDA-MB-231 cells (13,79).

2.2.3.3 The Use of Magnetic Nanowire as a Theragnostic System in Cancer

It is important to note the role of magnetic NWs in theragnostic, a paradigm shift promoting personalization of treatment through the combination of diagnostics and therapeutics. The role of magnetic NW platforms in therapeutics encompasses targeted and triggered release drug delivery, photothermal therapy, and magnetic actuation systems as discussed above (80). In terms of diagnostics, the large surface area of NW increases the efficacy of fluorescence labelling while in terms of magnetic NWs, it increases the magnetic moment, making it attractive in fluorescence imaging and MRI, respectively. Contrast agents for MRI are grouped into two categories, namely T_1 and T_2. The distinguishing factor between T_1 and T_2 agents is that T_1 is based on longitudinal magnetization recovery while T_2 is based on transverse magnetization decay (81). In this regard, Fe and Ni NW have been shown to be useful T_2 contrast agents with Ni NW being comparable to commercial agents (82,83). The effectiveness of NW in both therapeutics and diagnostics makes NW and magnetic NWs an attractive prospect for designing theragnostic systems for cancer.

2.3 NW Fabrication and Synthesis of Magnetic Nanowire Drug Delivery Systems

2.3.1 Fabrication Methods of Magnetic Nanowires

There are two main approach strategies for the fabrication of NW. Namely, the bottom-up and top-down approaches. The bottom-up approach involves the spontaneous assembly of small substrates (atoms or molecules) into the desired nanostructure while the top-down approach involves the breakdown of a suitable starting material until the desired nanostructure is formed (84).

A common top-down technique is lithography. Lithography is further divided into various techniques including photolithography and electron beam lithography. The main principle of these techniques is that a pattern is engraved onto an underlying substrate and the desired material is transferred onto the pattern. Therefore, these techniques are a hybrid of the top-down and bottom-up approaches.

These techniques have the advantage of easily being scaled up and can be used for the production of one- and two-dimensional particles that has at least one lateral dimension in the nanoscale range, however the resolution achieved is low and has etching and coating constraints, thus making it impractical for the use in drug delivery (84,85).

Bottom-up techniques enable the synthesis of complex structures such as non-straight vertical structures, structures made up of multiple components, and structures that have changes in the chemical composition. The main advantage provided by bottom-up techniques is the ability to synthesize structures with high aspect ratios. Bottom-up techniques employ chemical (55,86), physical (87), and electrochemical (88) methods to produce nanowires.

The NW fabrication techniques are summarized in **Table 2.1**, noting the advantages and disadvantages of each while selected fabrication techniques of promising methods used for the NW synthesis in drug delivery are discussed in further detail below, further highlighting the advantages and disadvantages of the technique and evaluating the potential for each technique to advance drug delivery.

Table 2.1: Overview of fabrication techniques applied for the synthesis of Magnetic NWs.

Fabrication Technique	**Top-Down/ Bottom-Up**	**Magnetic NW Composition Achievable by This Technique**	**Remarks on Technique**	**References**
Electrodeposition	Bottom-up	Fe and Fe-based compounds Co and Co-based compounds Ni and Ni-based compounds	Cost effective. Enables synthesis of accurate dimensions and complex structure. Individualistic growth on non-planar surfaces	(89–91)
Atomic Layer deposition	Bottom-up	Fe and Fe oxides Co and Co oxides Ni and Ni oxides	Cost effective. Enables complex structure synthesis. Slow deposition rate	(91,92)
Chemical vapor deposition	Bottom-up	Single-crystalline Ni and Ni alloys single-crystalline Co and Co alloys single-crystalline Fe and Fe alloys	Cost effective. Enables complex structure synthesis. Difficult to deposit multicomponent constituents.	(91,93)
Pulsed laser deposition	Bottom-up	Fe and Fe oxides Co and Co oxides Ni and Ni oxides	Cost effective. Enables complex structure synthesis. Difficult to control dimensions of NW.	(91,94)
Focused Electron Beam Induced Deposition	Bottom-up	Fe deposits Co deposits	Cost effective Enables complex structure synthesis. Lack of control in final composition of NW.	(91,95)
Chemical reduction	Bottom-up	Fe and Fe-based materials	Cost effective. Difficult to control NW	(91,96)

		Ni and Ni-based compounds	dimensions and morphology.	
Solvothermal	Bottom -up	Co and Co-based compounds Ni and Ni-based compounds Fe and Fe-based compounds	Difficult to control NW dimensions and morphology. Requires high temperatures and pressures.	(91,96)
Hydrothermal	Bottom -up	Fe and Fe-based compounds Co and Co-based compounds Ni and Ni-based compounds	One step synthesis. Difficult to control NW dimensions and morphology.	(91,96)
Sol-Gel	Bottom -up	Fe and Fe-based compounds Co and Co-based compounds Ni and Ni-based compounds	Cost effective. Scalable. Can form defects in products.	(91,97)
Lithography Techniques	Top-down	Fe and Fe-based compounds Co and Co-based compounds Ni and Ni-based compounds	Flexible in designing nanoparticles. Low resolution. High cost.	(91,98)

2.3.1.1 Electrodeposition of Magnetic Nanowires

A very convenient and common method for nanoparticle synthesis is electrodeposition. It was traditionally used as a conventional surface modification method for adjustments of surface morphology and characteristics and can be used to fabricate nanoparticles of single or multiple composition (99–102). Electrodeposition is the formation and deposition of solids through electrochemical reactions. These solids are usually formed by the reduction of an electroactive species contained in an electrolyte by applying a potential. This distinguishes it from electroless deposition in which a reducing agent replaces the applied potential (103).

A further distinction can be made in the electrodeposition of NW; deposition using templates and template-less deposition (91). There are two types of templates, soft templates, and hard templates. Soft templates are non-rigid structures that are used to control the direction of growth and therefore resultant shapes of nanoparticles produced. Soft templates include surfactant aggregates, micelles, and co-block polymers, and can be used to generate porosity and texture control of the resultant NW. The downside of soft templates is that the baths containing the soft templates usually express a low conductivity, which in turn hinders the electrodeposition process. Hard templates are rigid structures that are conductive on one end

and regulate the size and shape of the synthesized nanoparticles by the shape of the template itself. The pioneering work of Possin first demonstrated this principle of fabricating small diameter NW in porous membranes (104). Hard templates are extremely versatile, convenient, and are recurrently used in the synthesis of NW. The most common hard templates are anodized alumina, polycarbonate membranes, and mesoporous materials (105). Hard templates allow for the synthesis of freestanding NW as well as both orientated and non-orientated NW. They also facilitate the synthesis of complex one-dimensional NW (91). The downside of using hard templates include the removal of the template as it can affect the NW, diffusion of the electroactive species through the narrow diameter pore channels, difficulty in upscaling due to the difficulty of producing large templates with homogenous pore distribution (with small pore diameters), and the difficulty of producing templates with uniform pore diameters. When no physical template is used for controlling the morphology and shape of the produced nanoparticle, deposition rates are used in its place. Control of deposition rates is achieved by the modification of current density concentration of the electroactive species, temperature, and applied potentials.

Electrodeposition therefore has the potential of producing NW for effective drug delivery systems as precise control of the NW dimensions can be achieved, which is essential for positive cell interaction, control of magnetic ability, and drug loading. This technique can produce a variety of non-toxic, biocompatible NW including iron oxide, iron, and iron–palladium NWs, as well as segmented NWs in a convenient, scalable, and reproducible way; thus, providing a stable platform in which drug delivery systems can be engineered onto while keeping the inherent benefits of a NW for multifunctional systems.

2.3.1.2 Pulsed Laser Deposition of Magnetic Nanowires

Another common and valued growth mechanism for the synthesis of nanowires is pulsed laser deposition (PLD) (106–109). A pulsated high-powered laser beam is used to excite the surface energies of a target substrate in a controlled atmosphere producing an ejected plume. The vapor is then deposited onto a sample stage producing thin films or nanoparticles with the same composition as the target. PLD allows for synthesis of nanoparticles with a monocrystalline nature, high purity, and low defects to be synthesized. Other advantages of PLD are that it has a fast production rate, and it is scalable.

Shkurmanov and co-workers studied the growth of zinc oxide (ZnO) nanowires via PLD in order to understand the mechanism in which the nanowires are formed (110). They observed

that the NW growth was non-linear and can be explained in terms of the number of laser pulses applied and its interaction with four distinct flows of particles. The first flow forms the nuclei in which the NW will grow from, while the second flow is responsible for the vertical growth of the nanowire. The third flow was found to cause a backflow and decreased the length of the NW. Lastly, the fourth flow was responsible for the lateral growth of the NW. This proved that geometric parameters can be controlled when using PLD.

An exemplary study of Nikov et al. paved the way for the formation of magnetic NWs using PLD by employing the aid of a magnetic field (108). This study provided a simple method of producing magnetic NWs, which increases its industrial value. This method also produces NWs composed of smaller nanoparticles. This property can be exploited to affect drug loading capabilities of drug delivery systems potentially positively. Furthermore, Nikov and co-workers used this method to fabricated iron oxide NW (111). This study further demonstrated that the pressure and surrounding gas can be used to manipulate the type of oxide formed. Another interesting effect of the magnetic field is that it allowed the deposition of the iron oxides in arranged nanowire structures at a low pressure and a target substrate distance of 40 mm.

PLD provides an effective method of producing NW arrays, which are especially promising in implantable and transdermal drug delivery systems. It excels in producing NW composed of magnetic materials, which is a property that can be exploited in the development and commercialization of multifunctional drug delivery systems.

2.3.1.3 Other Synthetic Techniques of Magnetic Nanowires

There are various other fabrication techniques in which NWs can be synthesized. However, the most promising fabrication technique is electrodeposition due to its precise dimension control. These techniques are commented on in **Table 2.1** and include atomic layer deposition, chemical vapor deposition, pulsed laser deposition, focused electron beam induced deposition, chemical reduction, solvothermal, hydrothermal, sol-gel, and lithography techniques such as photolithography and electron beam lithography.

2.3.2 Magnetic Properties and Advantages of Nanowires in Drug Delivery Systems

NW are synthesized from both magnetic and non-magnetic substrates. Both NW and magnetic NWs offer potential advantages over nanoparticles and magnetic nanoparticles due to their larger surface area to volume ratio (high aspect ratio), which allows for greater drug loading, increased attachment sites, for decorations such as proteins, peptides, and polymers, and increased binding to cells. Magnetic NWs have greater advantages when compared to magnetic nanoparticles due to their strong shape anisotropy and energetically favourable magnetization. They provide greater magnetic moments and in the presence of an alternating magnetic field, can either provide mechanical motion by aligning to the magnetic moment with an applied low-frequency alternating magnetic field or induce a local hyperthermia at a high-frequency (~100 kHz) alternating magnetic field (13).

The most frequently used materials for synthesizing the magnetic components of magnetic NWs for drug delivery systems are Fe, Ni, Co, as well as their compounds and alloys. Magnetic NWs display specific advantages when compared to spiracle and other nanoparticles as well. The increased aspect ratio of ferromagnetic NWs provides stronger magnetic moments per unit volume and large remnant magnetizations without decreasing the mobility of the nanoparticles. The larger remnant magnetization allows the NW to be used in low-field environments, which in turn translates into NWs being able to target deeper tissues with smaller and weaker magnets as the geometry of NWs has an increasing effect on force applied by the magnetic field. NWs with aspect ratios greater than three show larger magnetic dipoles when compared same volume spherical nanoparticles (22). This results in the potential of a more efficient magnetic system to be designed for magnetic drug targeting for cancer therapeutics.

2.3.3 Stabilization and Functionalization of the Magnetic Nanowires

The surface area of NWs are decorated with coatings mainly for three intended purposes: To increase the biocompatibility of the NW, stabilize the NW (prevent NW agglomeration), and to functionalize the NW in order to tailor the NW to excel in the niche of interest (64).

The work by Zhu et al. used a coating of PEG and GO to both stabilize and functionalize their Co NW, thereby increasing its drug loading capacity and biocompatibility. Both the PEG and GO were attached to the Co NW by electrostatic adsorption using an ultrasonic dispersion method. The GO played a dual role; to enhance the photothermal therapy efficacy, as it is a

known photothermal agent, and to provide attachment points for the loaded drug (Doxorubicin) (55). When irradiated with an 808 nm laser for six minutes, the Co NW and GO-functionalized CO NW heated to a temperature of 39.1 °C and 40.6 °C, respectively, indicating the ability of GO to improve the excellent photothermal effect of Co NW.

Magnetic NWs can also be functionalized by the attachment of antibodies to target specific cells, thus increasing its selectivity. Contreras et al. successfully functionalized their Ni NWs with EGFR antibody (ab62 abcam®). This was achieved by first modifying the antibody with N-Succinimidyl S-acetyl thioacetate. Thereafter, it was further modified to introduce sulfhydryl groups so that it could attach to the Ni NW (112).

The NW system of Martínez-Banderas and research group was tested with three distinct coatings, BSA, APTES, and APTES-PEG. The BSA and APTES were covalently bonded to the surface Fe_2O_3 interphase of the Fe NW while they functionalized APTES with PEG by activating the APTES with sulfhydryl groups and the reacting with the thiol group in thiol-PEG, thus achieving disulfide bonds. The three coatings were compared using MDA-MB-231 breast cancer cells, which were incubated with the coated Fe NW and added cyanide Fe salt. Bright field imaging was used to determine the distribution, size, and morphology of the Fe NW agglomerates. All three coatings reduced the size of the agglomerates, thus ensuring a greater homogeneity of the Fe NW distribution across the sample. APTES-PEG had the least efficacy of this effect (13). **Figure 2.4** A and B depicts the transmission electron microscopy image of the APTES-NW and BSA-NW respectively, visualizing the coating on the NW.

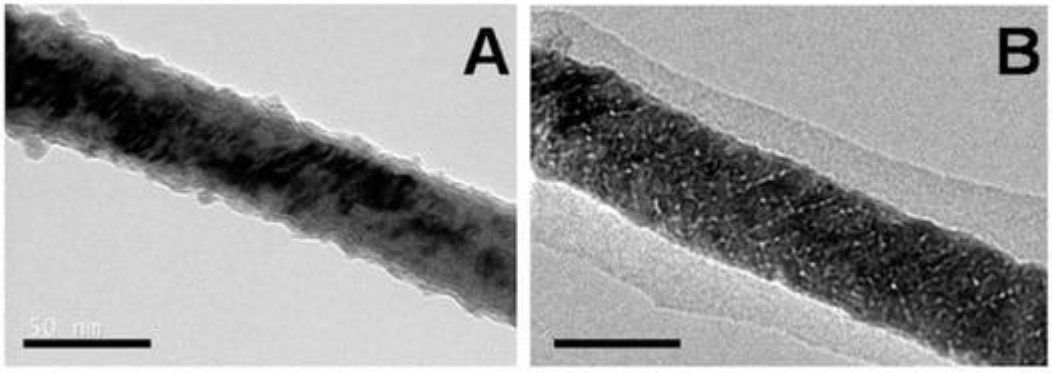


Figure 2.4: Figure showing surface modifications on magnetic NWs for stabilization. (**A**) (3-aminopropyl) triethoxysilane (APTES)-coated Fe NW. (**B**) Bovine serum albumin (BSA)-coated Fe NW. Reproduced with permission from (13). Scale bars: 50 nm.

Contreras and co-workers did not stabilize their Ni NWs with any coating, which thus caused the aggregation of the Ni NW. The Ni NW zeta potential was measured to be a low value of −15.1 mV (113). This value infers a weak electrostatic repulsive force which correlates with Contreras' observation of released Ni NW aggregating. This study highlights the efficacy of surface coatings to stabilize NW in terms of aggregation of the NW. Preventing the NW tendency to aggregate is essential as particle aggregates in the bloodstream can cause an embolism, while in tissue it can cause heterogeneous cytotoxic activity. Martínez-Banderas and research group managed to reduce the aggregation of Fe NWs, which is known to have higher remnant magnetization, which makes it inherently unstable. The stability of the Ni NW can be increased with surface modification such as coating with charged polymers or non-magnetic metal such as Au. The increase in magnetic NW stability increases its desirability in drug delivery as it will allow for safer therapy a formulation with a longer shelf life.

Stabilizing NW is therefore indispensable in the design and formulation of NW drug delivery systems as it prevents the aggregation of magnetic cored NW caused by their remnant magnetization. This, in turn, reduces the probability of mechanical obstruction in the circulatory system caused by NW aggregation. Therefore, NW coatings allow for the optimal design of multifunctional systems, which is essential in potentially improving cancer therapeutic outcomes.

2.3.4 Chemotherapeutic Drug Loading and Release of Magnetic Nanowire Systems

Large surface area has a positive influence on the drug loading capacity of nanosystems. Thus, NW morphology has a direct impact on drug loading capacity. Although NWs inherently have large surface areas, their surface area can be increased further by changing their morphology to include rough surfaces (114,115) or by synthesizing porous NWs (116,117). Guo and co-workers achieved a high drug loading of 2000 mg/g using porous NW while Zhu and co-workers achieved a high drug loading capacity of 992.91 mg/g with their Co NW, which had a rough morphology. The GO in the functionalized Co NW of Zhu and research group provided attachment points for DOX or other therapeutic agents as it is decorated with many functional groups on its surface such as hydroxide radicals. In the case of DOX, it is hypothesized that it is also able to absorb directly onto the GO via π-π interactions. Their NW system also exhibited a higher drug release profile in acidic environments and after near infrared radiation when compared to the control (55). The decrease in PH made the DOX more hydrophilic and soluble due to the protonation of the NH_2 group on it, thus causing the release

from the Co NW-GO. They also proved a direct correlation between drug release and laser power intensity.

The BSA and APTES coated Fe NW of Martínez-Banderas and colleagues were functionalized using PH responsive covalent bonds. This was achieved by introducing free thiol groups to the coated Fe NW by reacting 2-IT and amine groups on the coated Fe NW. The free thiol groups were then reacted to the maleimide group of a DOX derivative (5-Maleimidovaleroyl) hydrazone of Doxorubicin in order to attach it. This yielded low loading capacities of 50 µmol DOX/g Fe (27 mg/g) for the DOX-APTES-Fe NW and 25 µmol DOX/g Fe (13.6 mg/g) in the case of DOX-BSA-Fe NW (13). The low loading was due to the relatively smooth surface of the Fe NW, highlighting the importance of morphology on drug loading.

2.4 Cellular Interactions and Toxicity Between Magnetic Nanowires and Cells

2.4.1 Cellular Internalization of Magnetic Nanowires

Cellular internalization of NW supports the NW utilization and efficacy. There are three main potential uptake mechanisms for nanoparticles; receptor-mediated endocytosis, pinocytosis, and phagocytosis (118). NW suffers an inherent disadvantage when compared to spherical nanoparticles in terms of cell internalization. It is speculated that the different curvatures between the two shapes have a direct effect on cell binding. When the longitudinal axis of NW is bound to the cell membrane, the larger surface contact area blocks available membrane receptors, thus reducing cell internalization. There are many factors that govern cell internalization of nanoparticles besides shape. These are extensively discussed in a review conducted by Murugan et al. of the Wits Advanced Drug Delivery Platform, South Africa (119). Briefly, in order to design smart nanosystems, an understanding of physicochemical properties is essential. Other determinant factors in terms of cell internalization include uptake pathways and interaction of the nanoparticles with receptors. Neutral and cationic nanoparticles have higher transport efficiency into the cells when compared to negatively charged nanoparticles (120,121). This phenomenon is the result of anionic particles having smaller binding efficiency to cell surfaces when compared to cationic and neutral particles, leading to a reduction in membrane-wrapping phenomena resulting in a decrease in cellular internalization (120,122,123). Hydrophilic outer protective layers increase circulation time while nanoparticles functionalized with proteins or peptides directly increase cellular uptake by localizing the nanoparticle at the targeted site, receptor-mediated endocytic pathways, and direct cell penetration. Nanoparticle size also plays an important role in cellular uptake; 95–200 nm is

the ideal size according to the literature for increased cellular uptake (124). In terms of NWs, high aspect ratio NWs can also be internalized (125).

Fe NW also have good cell internalization as shown by (126) and further demonstrated by Martínez-Banderas and co-workers. Martínez-Banderas and co-workers had a total cell internalization for their APTES-Fe NW and BSA-Fe NW of 19% and 15%, respectively. These values were determined using Inductively Coupled Plasma Mass Spectrometry (ICP-MS) measurements on their incubated cells with the coated Fe NWs. The results yielded no significant difference for the APTES-Fe NW and BSA-Fe NWs in the cellular internalization (13). **Figure 2.5 (A)** and **Figure 2.5 (B)** shows the cellular uptake using HeLa cells of uncoated, positively charged, non-uniformly sized Fe NWs of Song and co-workers. The weakly negatively charged Ni NW of Contreras and research group also had a high affinity to cell internalization. Similar results were achieved for other Ni NWs, including those with large lengths (127). The cellular uptake of FePd NW of Guo and co-workers was studied on RAW264.7 and HeLa cells. Both cell lines took up both single NW and NW clusters with RAW264.7 cells having greater cell internalization, suggesting rapid removal from blood stream.

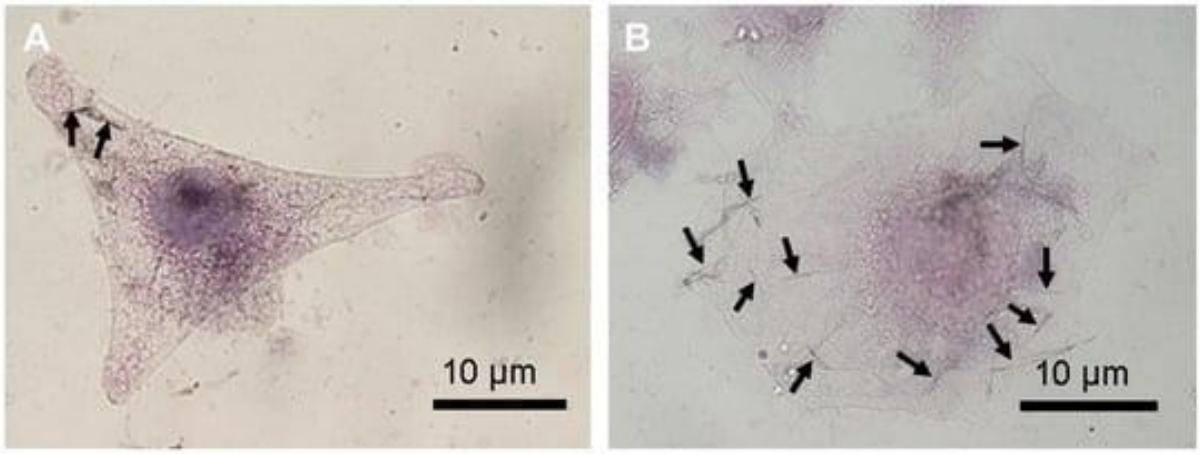


Figure 2.5: Cellular internalization and accumulation of magnetic NWs into cells. (**A**, **B**) Internalized Fe NW in HeLa cells. Adapted with permission from (126). Scales bars: 10 µm.

2.4.2 Cellular Toxicity of Magnetic Nanowires and Drug Loaded Magnetic Nanowires

Toxicity is important when designing nanosystems. The coatings used in NW systems are usually well-known biocompatible molecules used to counter the toxicity of toxic inorganic NW. Common NWs used in NW systems are silicon, Au, silver, Co, Fe, and Ni, amongst which Co, Fe, and Ni and their compounds produce magnetic NWs. From these, Co and Ni are the most toxic while Fe and silicon are deemed biocompatible. However, in comparison to Fe NW, a large number of studies have been conducted on Ni NW despite Ni's known cytotoxicity, carcinogenicity, and genotoxicity (128,129), and the literature reveals that Fe is less toxic. The reason for this is that the large remnant magnetization of Fe NWs causes stronger aggregation and thus limits its use in the single NW form. Metal alloys are also used to synthesize NWs, such as iron palladium (FePd) NWs. FePd NWs are non-toxic and do not readily undergo oxidation (14,130). Si NWs are also known to be non-toxic, have high biocompatibility, improve hydrophilicity, and can be made magnetic by decorating with Fe oxide nanoparticles. In terms of the effect of the NW length on cellular toxicity, Donaldson et al. reviewed the effect of fiber like particles and found that longer fibres were more toxic then shorter fibers (131). However, Song et al. showed that at the same concentration, Fe NWs of shorter lengths (2 μm) were more toxic then longer lengths (5 μm) of Fe NWs (126). According to Song et al., this was attributed to smaller size particles having greater cellular internalization (132).

The toxicity of magnetic NWs can be altered by surface modifications of the NW. Zhu et al. conducted biocompatibility tests of their GO and PEG decorated Co NW by determining its cytotoxicity using 3T3 and 4T1 cells and hemocompatibility by determining if the Co NWs, Co NWs-GO, and Co NWs-GO-PEG caused thrombosis or haemolysis. The Co NW itself was found to be very toxic. However, the addition of GO and PEG decreased the cytotoxicity of the system to a great extent. The cell viability of 3T3 and 4T1 cells after culturing with the NW was 35% and 32%, respectively, for the Co NW, while it increased to 96% and 89%, respectively, for the Co NWs-GO-PEG for both at 50 μg/mL concentration. Their results also show no significant difference in the thrombosis time and did not cause haemolysis (55).

Applying an alternating magnetic field to magnetic NWs while it is incubated with cells increases the toxicity of the NW. When incubating their Ni NW with HCT116 cells, Contreras and co-workers measured no significant drop in cell viability using 2.4 μg/mL of Ni NW without the presence of an alternating magnetic field, while at a concentration of 12 μg/mL, the cell viability dropped to slightly below 90%. When an alternating magnetic field is applied at 1 Hz, 0.5 mT for 1 h, the cell viability for 2.4 μg/mL drops to around 75% while using a concentration

of 12 μg/mL causes the cell viability to drop to slightly below 70%. This shows that higher concentrations of magnetic NWs have a greater effect at inducing cell death (64).

The cellular toxicity of magnetic NWs increases when functionalized with cytotoxic agents both with and without the presence of an alternating magnetic field. Martínez-Banderas and co-workers conducted cell studies for their Fe NW systems using Alamar Blue assay and MDA-MB-231 cells to determine their systems ability to induce cell death in cancer by combining the cytotoxicity of DOX and the mechanical motion provided by the low-frequency alternating magnetic field. Their results showed that alternating magnetic field without the Fe NW systems had no effect on the cell viability and cytotoxicity of DOX. The coated Fe NW systems without the alternating magnetic field present had no significant decrease in the cell viability, which is testament to its biocompatibility while when in the presence of an alternating magnetic field produced a significant decrease in cell viability of 23% and 28% for the and APTES- Fe NW (26 μg of Fe/mL) and BSA-Fe NW (28 μg of Fe/mL), respectively, showing possible cancer cell death by magnetic actuation. For the DOX-Fe NW systems, they showed a decrease in cell viability of 54% and 58% for DOX-APTES-Fe NW (26 μg of Fe/mL, 1.3 μM DOX) and DOX-BSA-Fe NW (28 μg of Fe/mL, 0.73 μM DOX), which is indicative of their selective intracellular drug release and the efficacy of Fe NW as nanocarriers. The addition of an alternating magnetic field to the DOX loaded Fe NW systems yielded a further 10% and 8% reduction in cell viability for DOX-APTES-Fe NW (26 μg of Fe/mL, 1.3 μM DOX) and DOX-BSA-Fe NW (28 μg of Fe/mL, 0.73 μM DOX), respectively, showing a weak additive effect instead of a synergistic effect for the combination of chemotherapy and magneto-mechanically induced cancer cell death (13).

It is interesting to note that although the BSA-Fe NWs had a lower drug loading capacity compared to APTES-Fe NWs, their efficacy in cytotoxic activity was similar. This was attributed, according to Martínez-Banderas and research group, to the greater cell internalization of the BSA-Fe NWs. Another point of interest is that NW can be used for the separation of biomolecules, their purification, and manipulation, which is applicable in the development of biosensors. This technology can lead to the ability to effectively detect circulating tumour cells leading to a better prognosis for cancer patients (133).

2.4.3 Cellular Degradation of Magnetic Nanowires

Understanding carrier degradation or metabolism is important in nanoparticle drug delivery to ensure high therapeutic efficacy (134). The innovative work by Safi et al. revealed that cells are able to degrade NWs as well as decrease the size of the aggregates with their remains found directly dispersed in the cytosol or in vesicular compartments. Singular NWs, on the other hand, were found in endosomal compartments only (135). Fe NWs and Ni NWs have oxidized surfaces and continue to be oxidized, degraded, and dissolved intracellularly by the lysosomal compartments. Perez et al. reported that ~2% of the Ni NWs dose was dissolved intracellularly after 71 h (136) and Fe experienced the same fate with the lysosomes without cytotoxic contribution. The fate of both the degraded and non-degraded NWs is potentially renal clearance. High aspect ratio nanoparticles have been found to be renally clearable with high efficiency of elimination. This is caused by the flow orientation of high aspect ratio nanoparticles, which aligns the long axis of the nanoparticle to point to the glomerular capillary pore openings (137).

2.5 Conclusions and Future Prospects

The application of magnetic NWs has great potential for improving therapeutic outcomes for cancer therapy. They provide the benefits of traditional nanoparticles in addition to the inherent advantages of NW, thus making NW an ideal platform to build multifunctional nanosystems upon. However, the full potential of magnetic NWs in drug has yet to be reached as further applications and functionalisation's that can be moulded onto the versatile magnetic NWs platform such as Wnt inhibitor delivery systems, attachment of ligands in order to increase the selectivity, and a theragnostic system that includes the attachment of fluorescent compounds, chemotherapeutic drugs, and modifications that increase cancer cell selectivity, require further research. Effective *in vivo* studies for multifunctional NW nanosystems are essential for the progression of this technology into the pre-clinical phase. The magnetic applications of NWs such as magnetic hyperthermia, magnetic actuation, and magnetic drug targeting has shown great potential for improving cancer therapeutics and therefore requires further research to optimize an efficacious multifunctional therapeutic system that will better the prognosis and increase the quality of life for cancer patients. The control of induced temperature change in hyperthermia therapy needs to be studied and optimized in *in vivo* studies. Improvements can be made in tumour targeting so that magnetic NWs can be accumulated into the tumour using a three-dimensional targeting model. This will be beneficial in the development of alternate treatment strategies for TC that will have lower associated adverse reactions and is testicular

saving. This potential benefit of using NWs in the treatment of TC warrants the further study of these platforms.

CHAPTER 3.
Synthesis, Characterisation and Cytotoxic Evaluation of Fe NWs and Pt NWs

3.1 Introduction

Magnetically active systems incorporating nanoparticles is a promising approach in aligning cancer therapeutics towards the paradigm shift transitioning to the personalisation of medicine. Magnetic nanoparticles can be engineered to create actively targeted delivery systems. MTD physically guides the drug or drug carrier to the localised disease site with the aid of an external magnetic field, increasing the concentration of the nanosystem at the target site (138).

In MTD, nanosystems are introduced at an appropriate vessel to the bloodstream that will allow for the expedient transportation of the nanosystems to the target area utilising systemic blood flow. An external magnetic field is then used to trap and remove the nanosystem in the capillary system where there are weaker forces for the nanosystem to overcome (14). The nanosystem is then accumulated in the target area through the external magnetic field. Iron oxide nanoparticles have been extensively studied regarding MTD as well as a variety of other biomedical applications including MRI contrast agents due to their unique magnetic properties (139).

Nanowires (NWs) have significant advantages compared to nanoparticles for MTD and allows for additional biomedical functionalities (12). Magnetic NWs have intrinsic magnetic advantages due to their shape anisotropy, provide greater coercivity values, and high magnetic moments per volume. This allows for the application of greater force and torque values applied during MTD and magnetic actuation therapy for bioactive accumulation and mechanical cell death (140,141).

One-dimensional magnetic NWs creates better heating efficiencies when compared to magnetic nanoparticles due to the provision of greater frictional reactive areas in magnetic NWs (140). As a foundation in the design of a therapeutic platform, magnetic NWs allow for the attachment of multiple functionalities such as selective bioactive release, active targeted drug delivery, magnetic actuation, hyperthermic agent, MRI contrast agents, and MTD (12). Magnetic NWs have been well studied and are attractive in biotechnological applications such as cell manipulation (142) and separation (143).

This chapter focused on the synthesis and characterisation of elemental Fe and Pt NWs. The synthesised NWs were subsequently characterised to determine their structural properties and composition. The inherent cytotoxic activity was then evaluated on two cell lines i.e., Tera-1 and 3T3.

3.2 The Concept of Magnetic Biomaterials: Magnetic Properties and Hysteresis

3.2.1 Magnetism

Flowing electric currents produce magnetic fields. This current flow can be provided from the flow of current in a conductor, the motion of electrons spinning around its own axis, or the orbit of electrons around an atom. The total magnetic field (B) also known as magnetic flux density or magnetic induction is defined by Lorentz force law in terms of a force on a moving charge.

When a generated magnetic field passes through a magnetic material, the magnetic material contributes to the magnetic field. The magnetic field strength (H), also known as magnetising force, is a magnetic quantity that specifically describes the magnetic field derived from the external current (144). The magnetic quantity H is independent of the response of the magnetic material. The SI unit for H is A/m. However, H is sometimes represented as oersted (Oe). 1 Oe = 79.5774715459 A/m.

Another important concept is magnetization (M). M is a vector quantity which quantifies the density of the induced or permanent magnetic dipole moments in a material. Magnetisation can be expressed in terms of either mass or volume. The SI unit for mass magnetisation is A.m2 /kg or Wb·m/kg. it can also be expressed as emu/g. Volume magnetisation can be expressed as emu/cm^3 and the SI unit is A/m.

The relationship between B, H, and M can be expressed as shown in **Equation 3.1** (145).

Equation 3.1: Equation showing the relation between B, H and M.

$$B = \mu_0(H + M)$$

μ_0 is a constant known as magnetic permeability of free space. The exact value of which is $4\pi \times 10^{-7}$ N/A^2. Therefore, the total magnetic field (B) inside of a material is related to the

combination of the applied external magnetic field (H) and the magnetisation of the material (M).

The measure of the magnetisation value at a given applied magnetic field (H) for a material is given by the magnetic quantity, magnetic susceptibility (X). Magnetic susceptibility is dependent on a material and can be expressed as shown in Equation 3.2 where M is the magnetisation of the material and H is the external magnetic field strength. This relation is specifically for volume susceptibility (146).

Equation 3.2: Equation defining volume susceptibility.

$$\mathrm{X} = \frac{M}{H}$$

3.2.2 Magnetic Properties of Biomaterials

Biomaterials can be characterised by the response that they exhibit in the presence of an applied magnetic field. The main types of magnetic materials can be classified as either ferromagnetic, diamagnetic, or paramagnetic. **Figure 3.1** summarises the behaviour of magnetic materials in the presence of an external magnetic field (H≠0) and when the external magnetic field is removed (H=0).

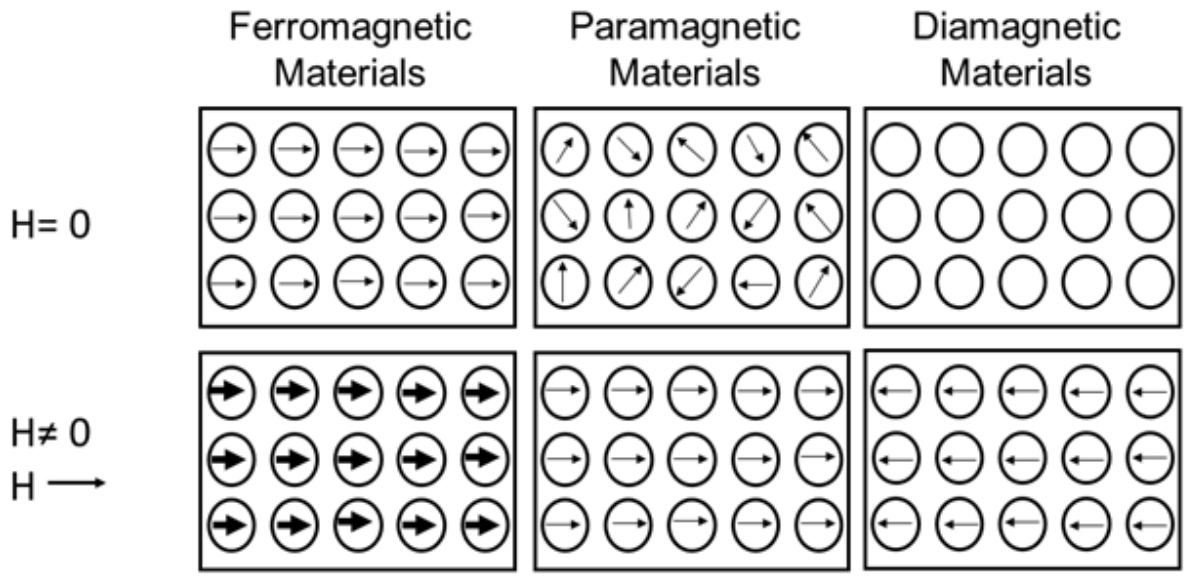


Figure 3.1: Summary of the basic types of magnetic behaviour in the presence (H≠0) and absence (H=0) of a magnetic field at a given orientation. Arrows represent spin orientation. Thicker spin arrows for ferromagnetic materials at H≠0 indicate a stronger magnetisation.

When the internal magnetization created by the applied magnetic field opposes the applied field, the material is characterised as diamagnetic. Diamagnetic materials have very small and negative susceptibility (χ) values. Their atoms exhibit no magnetic moments, they are weakly repelled in the presence of a magnet and once the applied magnetic field is removed, diamagnetic materials do not retain their magnetic properties (145).

When the internal magnetization created by the applied magnetic field aligns with the applied field, the material is either paramagnetic or ferromagnetic. Paramagnetic materials have very small and negative susceptibility values as well. Their atoms exhibit magnetic moments that are randomly orientated (145). Paramagnetic materials are weakly attracted by an external magnetic field and their magnetic properties are not preserved when the external magnetic field is removed.

Ferromagnetic materials have large and positive susceptibility values. Their atoms exhibit magnetic moments parallel to the applied field and ferromagnetic materials are strongly attracted by an external magnetic field (145). However, when the external magnetic field is removed, ferromagnetic materials retain some of their magnetic properties as shown in **Figure 3.2**.

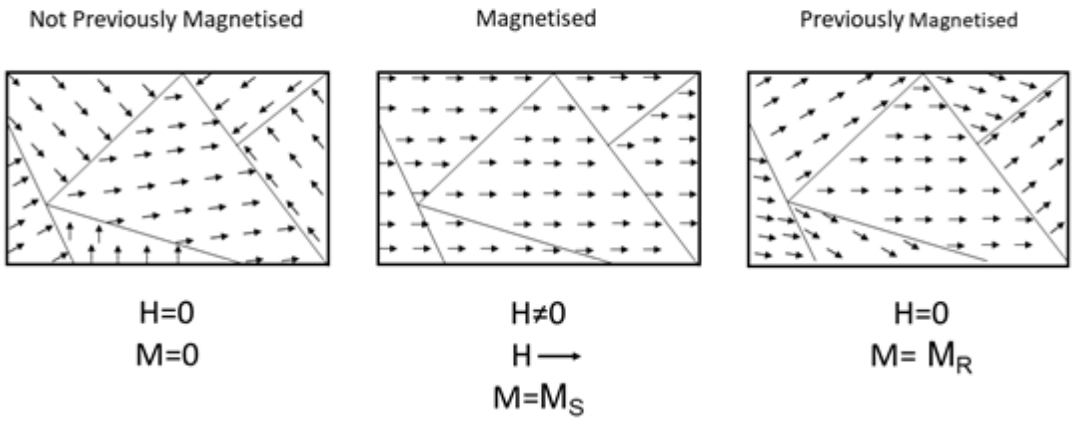


Figure 3.2: Ordering phenomenon of magnetic domains in ferromagnetic material. Domain walls are represented by the solid lines. The arrows depict the orientation of the magnetic moment.

Ferromagnetic materials have a characteristic ordering phenomenon (147). The spin of unpaired electrons lines up in a parallel orientation in small volume regions resulting in magnetic moments within these regions being aligned. These regions are called magnetic domains. Magnetic domains are separated from each other by domain boundaries.

If a ferromagnetic material has not been previously magnetized by an external magnetic field, the alignments of the magnetization of adjacent magnetic domains are randomly arranged to result in a zero net magnetization. When an external magnetic field is applied to a ferromagnetic material, the magnetization of these domains gradually lines up parallel to the applied magnetic field. When the magnetisations in all the domains line up, magnetic saturation (M_S) is achieved. In ferromagnetic materials that were previously exposed to an external magnetic field, the net magnetisation of the material does not return to zero. The fraction of retained magnetisation is termed as remnant magnetisation (M_R). This phenomenon will be further discussed in the section titled magnetic hysteresis.

A similar type of magnetic property to ferromagnetism is ferrimagnetism and anti-ferromagnetism. Ferrimagnetic materials comprise of adjacent magnetic moments that are unequal. Their atoms exhibit magnetic moments anti-parallel to the applied field. When ferrimagnetic materials are exposed to an applied magnetic field below Curie temperature, the induced magnetisation is permanent as in ferromagnetic materials. At temperatures greater than Curie temperature, the magnetic moments can be randomised by thermal agitation. Anti-

ferromagnetic materials have atoms that exhibit mixed magnetic moments parallel and anti-parallel to the applied field.

An additional type of magnetic property is relevant to this work, superparamagnetic (139). Superparamagnetic materials display similar behaviour to paramagnetic materials. In terms of nanoparticles, superparamagnetic occurs when ferromagnetic or ferrimagnetic nanoparticles are reduced in size. The susceptibility of superparamagnetic materials is much larger compared to paramagnetic materials. They are magnetised in the presence of a magnetic field and when the external magnetic field is removed, thermal fluctuation flips the magnetization creating a zero net magnetisation. Thus, making remnant magnetisation non-existent in superparamagnetic materials.

3.2.3 Magnetic Properties of NWs

NWs are cylindrical nanoparticles with large aspect ratios. This shape anisotropy (aspect ratio) is a vital feature of magnetic NWs. This is a main contributor to the high coercivity (Hc) and magnetic moments that magnetic NWs display compared to magnetic nanoparticles (142,148). An important property of magnetic NWs is the tunability of their magnetic properties including M_S, M_R, Hc, Curie temperature, and orientation of magnetic easy axis. This can be achieved by adjusting the length, diameter, crystalline properties, or composition of the NWs (84,140,149,150). NWs can be synthesised as alloys, multi-layered with materials of different properties, and core shelled.

3.2.4 Magnetic Hysteresis

After a ferromagnetic material is magnetised along a given direction in an external applied magnetic field, the magnetization of the ferromagnetic material will not relax back to zero when the magnetising field is removed (remnant magnetisation). The magnetising field needs to be reversed for the magnetisation of the ferromagnetic material to reach zero. Ferromagnetic materials can be manipulated using an external magnetic field and are therefore useful in targeted gene and drug delivery (151). **Figure 3.3** shows a typical hysteresis loop when a ferromagnetic material is placed in an alternating magnetic field (150).

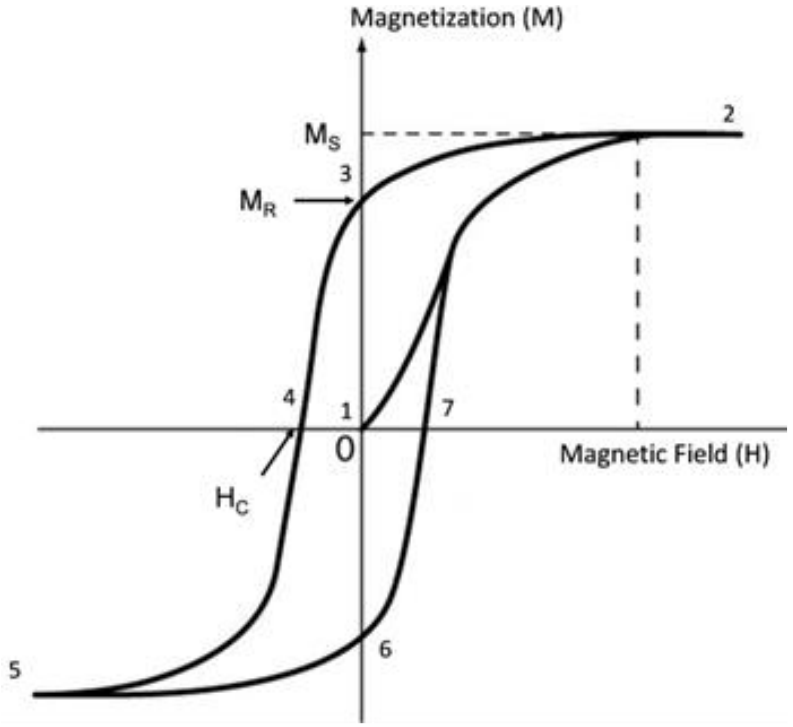


Figure 3.3: Representation of a hysteresis loop typical of ferromagnetic material. Adapted from (152).

If a ferromagnetic material is exposed to a magnetic field and then the applied magnetic field is reversed, reducing the magnetic field from saturation, a hysteresis loop develops. The Loop starts from the origin (Point 1) when a non-magnetised ferromagnetic material is exposed to an applied magnetic field. The magnetisation value rises until it plateaus at point 2. At this point, all magnetic moments within the ferromagnetic material align with the applied magnetic field and the magnetisation reaches M_S (Point 2).

The magnetic field is then reversed and as the field decreases, the alignment of the magnetic moments begins to become disordered. When the applied magnetic field reaches zero, the magnetisation of the ferromagnetic material does not reach the origin. The magnetisation when the field is equal to zero is known as remnant magnetisation (M_R) (Point 3). When the magnetic field is applied in the negative direction, the ordering of the magnetic moments continues to decrease until the magnetisation reaches zero. This point is known as coercivity (Hc) (Point 4).

The magnetic field continues increasing in the negative direction which cause the magnetic moments to align yet again until saturation is reached (Point 5). When the magnetic field is

now applied in the positive direction, the same magnetic behaviour is observed but in a symmetrical fashion, points 6 and 7 correspond to points 3 and 4 respectively. The shape of hysteresis loops tends to be distinct depending on the magnetic material type being measured. **Figure 3.4** shows the M-H curves for common types of magnetic materials.

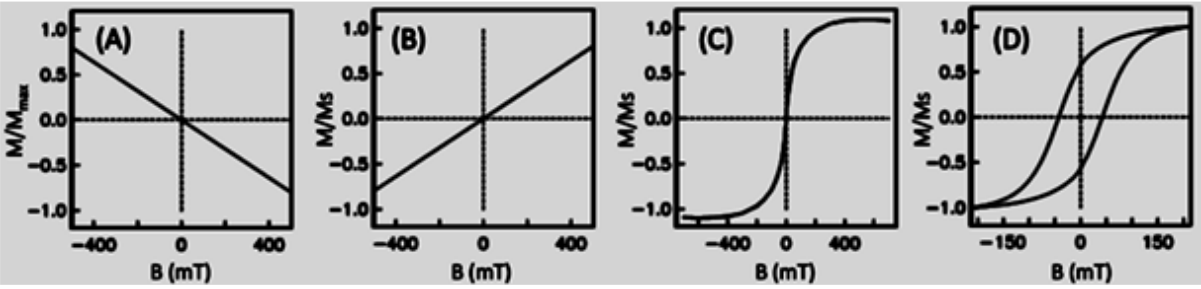


Figure 3.4: M-H loops of different behaviours of magnetic materials. **A)** represents diamagnetic materials, **B)** represents paramagnetic materials, **C)** represents superparamagnetic materials, and **D)** represents ferromagnetic materials. Adapted from Contreras (153,154)

Ferromagnetic and ferrimagnetic biomaterials are suitable in magnetic hyperthermia. Magnetic hysteresis is a suitable measurable characteristic for biomaterials. Hysteresis loss is represented by the energy lost during the oscillation of the biomaterial between the positive and negative magnetic fields. This energy loss can be dispersed as heat during hyperthermia therapy. Although superparamagnetic particles do not exhibit hysteresis losses, they can dissipate heat for hyperthermia applications through Neel relaxation (155). Ferromagnetic, ferrimagnetic and superparamagnetic biomaterials are applicable in the use of MTD. This is due to their ability to be manipulated using an external magnetic field (external force) which allows for targeted delivery to the required zone (155). The application of MTD in TC will allow for an increase in the concentration of actives in the targeted cells while decreasing the concentration of the active in healthy cells. Thus, potentially leading to greater therapeutic outcome and a decrease in adverse reactions.

3.3 Process of Electrodeposition

One of the most widely used techniques to synthesise magnetic NWs is electroplating the desired material into an insulating membrane that is nano porous (156). The membrane acts as a template which controls and contains the growth of the NWs creating a high aspect ratio one-dimensional structure by providing limited space for nucleation growth within the nanopores of the template. This constrained area of growth can give rise to consistent production of uniform NWs. This is advantageous for reproducibility and consistency of dosing.

Anodic Aluminium Oxide (AAO) templates are extensively used in the production of nanostructures due to the self-organization nature of the nanoporous structure and high customisation ability in terms of the nanopores length and diameter. This creates great flexibility of the templates that allow for nanopores with small diameters (~10 nm) to larger diameters (~250 nm) and high pore densities.

The thickness of the AAO templates depends on the oxidation time during the multi-step anodic oxidation used the fabricate the AAO templates. This allows for membrane thicknesses of between ~1 µm to ~100 µm. This membrane thickness controls the maximum length of the synthesised NWs. The fabrication process of AAO templates have been well established and their production has already reached commercialisation.

Template electrodeposition allows for the fabrication of a wide variety of NWs from metals and alloys to electroactive polymers as well as a composite between them. This technique has been first described by Possin *et al* in 1970 (104). In 1987 the pioneering work of Penner et al. introduced template synthesis to synthesise one-dimensional NW in polycarbonate membranes (157). After years of successful achievements and optimisation, template electrodeposition has currently become a cheap and straightforward method for synthesising one-dimensional NWs.

Template electrodeposition of NWs consists of two phases, the electrochemical reduction of the positive cations from an electrolyte bath in the nanopores of the template, and thereafter the removal of the NW from the template by dissolving the template. The electrodeposition of NW is usually carried out in a three-electrode system consisting of the working electrode (cathode), counter electrode (anode), and the reference electrode.

During electrodeposition, cations are transferred from the bulk solution (electrolyte) to the cathodic interface which is the template coated on one side with a conductive material. The ions are adsorbed onto the cathodic surface and after complete charge transfer form atoms that diffuse to vacant lattice sites through growth and nucleation mechanisms until complete pore filling has been achieved.

The ions are transferred through three main mechanisms, diffusion, migration, and convection. Diffusion takes place when the cations from a higher concentration in the electrolyte bulk travel to the lower concentration inside the template and is the main contributor of mass transport during NW growth. The cations diffuse from the electrolyte towards the cathodic surface. Migration occurs due to a potential gradient caused by a strong electric field. The positive cations travel towards the negatively charged cathode. Convection arises from the motion of the ions in the electrolyte and is dependent on the cell design.

Template electrodeposition follows a well-defined sequence following four stages which can be illustrated on a Current vs Time graph for potentiostatic electrodeposition (**Figure 3.5**) and diffusion phases that facilitate mass transport (**Figure 3.6**) (156,158). In stage one, which is the pre-growth phase, a sudden drop of current is observed when a potential is applied to the electrochemical cell. This current reduction is attributed to the limitations of the mass transfer of the ions in the electrochemical cell. The main mass transport mechanism in this phase is the first phase of diffusion where the diffusion front is one-dimensional and is inside of the AAO nanopores. In this stage, nucleation starts within the nanopores at the cathodic surface (conductive layer connecting the template to the circuit).

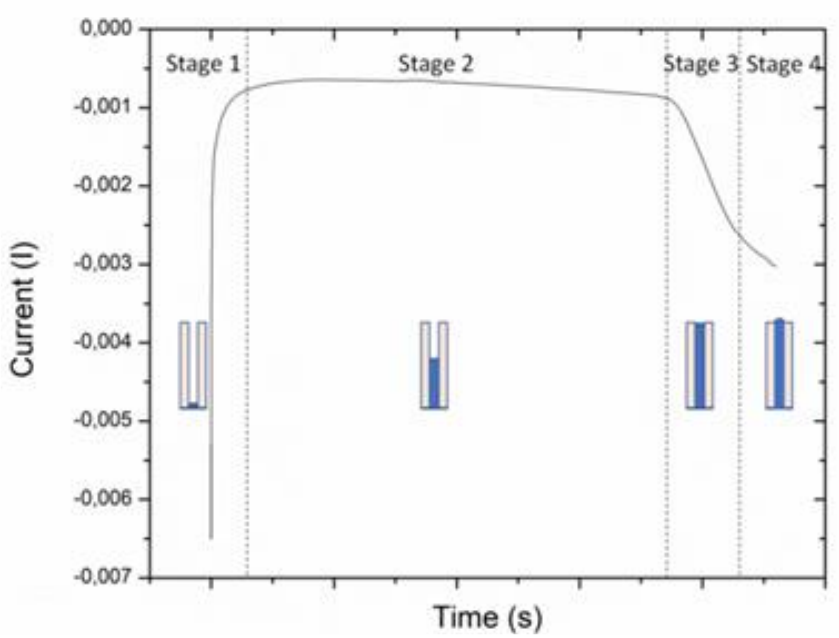


Figure 3.5: Image of a standard Current vs Time graph depicting the different stages of NW growth.

In stage two, The NW growth continues within the nanopores one-dimensionally and a steady slope of increasing current is observed until the nanopores have been filled. Two mechanisms of diffusion occur in this stage, phase two of diffusion where there is still linear diffusion in the nanopores of the template. However, the diffusion front reaches the opening of the nanopores, and a three-dimensional hemispheric front is created. Thereafter phase three diffusion starts where linear diffusion continues inside the one-dimensional nanopores. However, the three-dimensional hemispheric diffusion front across each nanopore on the template merge and form a planner diffusion outside the pore (**Figure 3.6**).

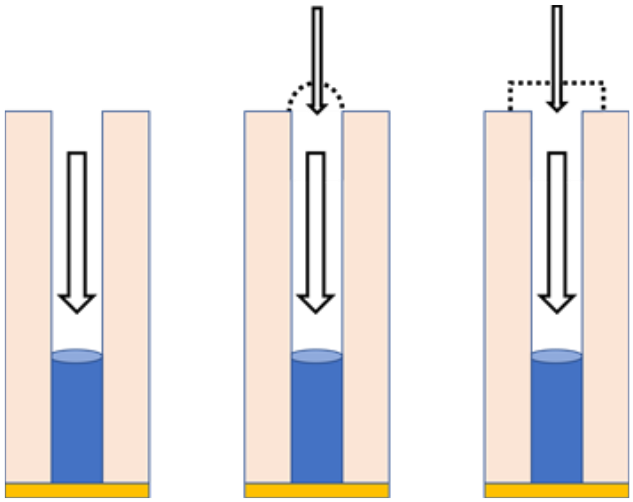


Figure 3.6: Representation of diffusion phases during NW growth within a nanopore: **A)** linear diffusion, **B)** linear diffusion with three-dimensional hemispheric diffusion front outside the nanopore, **C)** linear diffusion with planar diffusion front outside the nanopore (Adapted from Blanco et al. (159))

In stage three of the NW growth. The growth of the NWs extends beyond the nanopores, and a hemispherical cap is formed on each NW which join forming a film which covers the surface of the template. In the last stage of the NW growth, a rapid increase in current is observed due to the increase of the effective area of the cathode.

3.4 Experimental Setup for Electrodeposition

The experimental setup used (**Figure 3.7**) was a three-electrode electrochemical cell consisting of a connected sense and working electrode, a counter electrode, and a reference electrode which all potentials were measured with respect to. The working electrode was an AAO holder which the Au coated AAO template was placed in (1). The Au coat maintained electrical contact with the holder which was connected to the circuit while the open pores were exposed to the electrolyte to enable mass transfer of the metallic ions within the nanopores. The counter electrode was a small Pt plate (2), and the reference electrode was Ag/AgCl reference electrode (Metrohm) using 3 M KCl (3).

The electrodes were connected to a Autolab PGSTAT302N to provide a constant potential as measured between the reference electrode and sense electrode. The current was measured between the counter electrode and the working electrode. The reference electrode was placed

≤1cm to the working electrode to decrease the uncompensated resistance and ohmic losses arising from the uncompensated resistance.

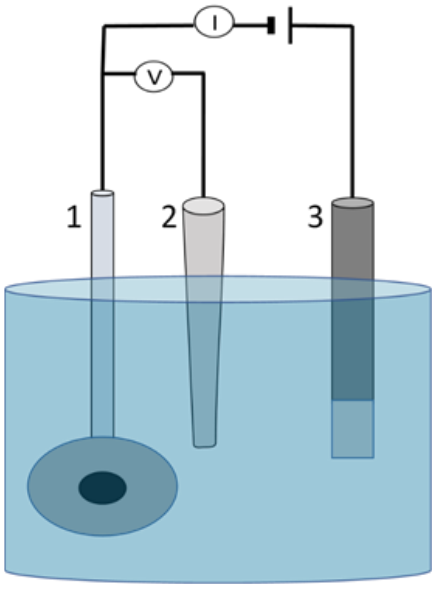


Figure 3.7: Two-dimensional representation of the electrochemical cell setup for NW electrodeposition. **1)** Holder for AAO template, **2)** Reference electrode, **3)** Counter electrode.

3.5 Rationale for Selecting Elemental Fe and Pt to Synthesise a Magnetic NW Advanced Delivery System

Magnetic NWs are well studied and traditionally composes of magnetic materials of Iron (Fe), Cobalt (Co), and Nickel (Ni). Fe magnetic NWs in particular have favourable characteristics which make them desirable in biomedical applications such as magnetically active targeted therapeutic systems. Fe is a well-known material that possesses ferromagnetic behaviour. Polycrystalline bulk Fe has a high M_s of 217.6 emu/g or ~1.7 X 10^6 A/m and thus favourable for MTD. They exhibit ferromagnetic behaviour, are biocompatible and their magnetic properties can easily be altered by manipulating the thickness of the outer oxide layer of the core shell Fe NWs (82,149).

Fe NWs are regarded to have low toxicity as high concentrations are required for them to exhibit cytotoxic effects. Their toxicity has been tested in HeLa cells by Song *et. al.* and found to have low overall toxicity at high concentrations of 10000 NW per cell (126). Fe NWs have been traditionally surface functionalized with chemotherapeutic drugs to provide cytotoxic activity against cancerous cells due to the low inherent cytotoxicity of Fe NWs.

Platinum (Pt) nanoparticles have high potential in biomedical applications. They are used in nanomedicine (160), radiation dose enhancement (161), and photothermal therapy (162). Pt nanoparticles have shown low toxicity to noncancerous cell lines such as peripheral blood mononuclear cells (PBMC) at concentrations of 200ug/ml (163). However, they exhibited a dose dependent toxic effect on cancerous cell lines such as prostate cancer cells (LNCaP), ovarian teratocarcinoma (PA-1), lung adenocarcinoma (A549), pancreatic cancer (Mia-Pa-Ca-2), breast cancer cells (MDA-MB-231), and human neuroblastoma cancer cells (SH-SY5Y) (163,164).

The toxicity of platinum (Pt) nanoparticles depends on multiple factors. This includes their size, shape, zeta potential and structure design (165). Needle-like nanoparticles like NW causes greater cell death when compared to nanoparticles due to their ability to damage cells upon direct contact (165,166). Pt nanoparticles are also found in alloys with other metals or in combination with metallic nanoparticles, which affects their toxicity (167). Pt containing yolk-shell nanocrystals have been found to have greater killing potency against HeLa cells (168). Jacob *et. al*. suggested that pure Pt nanoparticles cause cell death through apoptosis (SiHa/U251) and bimetallic (Au-Pt) mechanism of cell death (SiHa) was cell shrinkage, chromatin condensation and intra-nucleosomal DNA fragmentation (169). Zeng *et. al.* suggested that Pt nanoparticles can act as anticancer agents and be effective against chemotherapy-resistant tumours through activating apoptosis and decreasing intracellular glutathione (170).

Most studies on Pt cytotoxicity against cancer cells has been done on Pt nanoparticles (171). Cytotoxicity studies of Pt NWs attached to devises for neural signal detection have been studied with no significant cytotoxic effects of the Pt NWs found (172,173). The effect of free-standing Pt NWs structure design on toxicity has not been studied to the best of the authors knowledge. The toxicity of Pt NWs cannot be assumed to be the same as Pt nanoparticles as shown by the example of asbestos (174). Hence this study focused on the design of Pt-NWs as an alternative to enhance the bioactivity of Pt as a cytotoxic agent.

3.6 Basis of Cytotoxicity Studies

Cell based assays can be used to quantify cell proliferation or show cytotoxic effects that leads to cell death caused by test compounds. Cell viability assays such as tetrazolium reduction-based assays and resazurin reduction assay make use of markers to measure the enzymatic activity or general metabolism of viable cells.

Tetrazolium reduction-based assays employ tetrazolium compounds to detect and quantify viable cells. These compounds can be broken into two categories: a positively charged tetrazolium, MTT, which is can easily penetrate cells; and negatively charged tetrazolium's such as MTS, XTT, and WST-1 which do not readily penetrate cells. The negatively charged tetrazolium's use an intermediary compound due to them not being able to penetrate cells. This compound is usually cell permeable. Inside the cell this compound acts as an electron acceptor. The electron is then transferred to the tetrazolium to facilitate its reduction to the measurable formazan product which is florescent. The quantity of formazan product produced is directly proportional to the number of viable cells. The formazan product can therefore be easily measured using a microplate reader to quantify the cell viability (175).

Resazurin is a redox indicator dye that is cell permeable. It can be used to measure the viable cell number with protocols like that of tetrazolium reduction-based assays. Physiological buffers are used to dissolve the resazurin creating a deep blue solution. Cells with active metabolisms reduce the resazurin to a resorufin product that is fluorescent and pink in colour. As resazurin is cell permeable, an intermediate electron acceptor is not necessary for cellular resazurin reduction to occur. The fluorescent resorufin product produced which is proportional to the number of metabolically active cells (viable cells) can be measured using a microplate reader as well. Hence, the cell viability can be determined (175).

The cell viability assay chosen for this research was the tetrazolium reduction based XTT. The advantages of XTT include safe, easy to follow protocols, high accuracy, the ability to detect metabolic activity in low cell counts, and fast results achieved (176).

3.7 Materials and Methods

3.7.1 Materials

Commercially available AAO membrane with a stated diameter of 40 nm was used as a template to control the growth of the NWs and purchased from InRedox (Longmont, United States). $FeSO_4.7H_2O$, Na_2SO_4, H_3BO_3, ascorbic acid, H_2PtCl_6, $HClO_4$, NaOH, HCL, and HNO_3 was purchased from Sigma-Aldrich (Missouri, United States).

3.7.2 Chemical Electrodeposition Prototype for NW Synthesis

3.7.2.1 Synthesis of Fe NW

Core-shell Fe NWs were synthesised using a templated electrodeposition approach in a conventional tri-electrode setup. The AAO template used had a thickness of 50±2 µm, an average pore diameter of 40±4 nm, a density of 1×10^{10} cm^{-2} for the nanopores, and a porosity of 12±2%.



Figure 3.8: Schematic of the longitudinal cross-section of the prototype Fe NWs depicting the layout of the core shell structure

Firstly, a 30 nm gold (Au) layer was sputtered on to free standing AAO membrane with patent pores at both ends to create a conductive layer using a turbomolecular pumped coater (Quorum Q150T ES) in an argon (Ar) atmosphere. The Au layer acted as working electrode in the electrochemical deposition process. A Pt plate was used as counter electrode and Ag/AgCl in 3 M KCl (Metrohm Auto lab) was used as the reference electrode.

The cell design remained constant, and all electrical potentials were measured with respect to the reference electrode. The electrodes were connected to a potentiostat (Autolab PGSTAT302N). The electrolyte used comprised of 12% w/v $FeSO_4(7H_2O)$, 7.5% w/v Na_2SO_4, 2.5% w/v H_3BO_3 (to prevent hydroxide formation) and 1% w/v ascorbic acid. Fe NWs were deposited in the AAO template using a constant potential of -1.1V.

3.7.2.2 Synthesis of Pt NW

Pt NWs were synthesized using the same tri-electrode setup as described for Fe NWs. The Pt NWs was grown in a AAO template of 50±2 µm thickness, 40±4 nm average pore diameter, a pore density of 1×10^{10} cm^{-2} and a porosity of 12±2%.



Figure 3.9: Schematic of the longitudinal cross-section of the prototype Pt NW.

The template was coated with a 30 nm Au layer using a turbomolecular pumped coater (Quorum Q150T ES). The Au on the coated AAO membrane acted as the cathodic surface on the working electrode in the electrochemical cell. The electrolyte used comprised of 1% w/v H_2PtCl_6 and 7% $HClO_4$ and the Pt NWs were deposited at a constant voltage of -0.35 V.

3.7.3 Removal of the NWs from the AAO template, storage, and preparation for cytotoxic analysis

The sputter coated Au layer was removed using Aqua Regia (3:1 mixture of $HCl:HNO_3$), minimising contact time to prevent the dissolution of the synthesised NWs. The AAO templates were then dissolved using 1 M NaOH and sonicated for set periods (three 60 s intervals) to ensure the release of the NWs at the appropriate NW size from the AAO template. The released NWs were then collected using an external magnet or centrifugation for the non-ferromagnetic Pt NWs, washed thrice and suspended in ethanol for storage to preserve their magnetic properties (177).

To prepare the NWs for cytotoxic assessment, an appropriate concentration (as indicated in Chapter 3, Section 3.8.6) of NWs in suspension was aliquoted into a 2 mL Eppendorf tube prior to cell treatment. The ethanol was removed from the suspended NWs and washed thrice with deionised water.

3.7.4 Characterisation of the synthesised Fe NWs and Pt NWs

3.7.4.1 Quantification of the Synthesised NW Using ICP-OES

The Fe and Pt content of the NWs were quantified against external calibration curves using Inductively coupled plasma - optical emission spectrometry (ICP-OES) (Shimadzu ICPE-9820) so that accurate *in vitro* studies could be performed. Briefly, the sample preparation involved 100 µl of NW suspension aliquoted into a volumetric flask together with 300 µl of 32% HCl for Fe-NWs and Aqua Regia for the Pt-NWs. The HCl solution was then heated at 80°C for 40 minutes to ensure complete dissolution. The solution was then diluted to 20 mL and ran using the ICP-OES. Pt-NWs was digested using 300 µl of aqua regia instead of HCL and left at room temperature for 60 minutes. The solution was thereafter diluted to 20mL for ICP-OES analyses. The wavelength used to determine the concentration for Fe and Pt was 259.94 nm and Pt 203.646 nm respectively.

3.7.4.2 Morphological Characterisation of the Synthesised NWs

The TEM sample was prepared by diluting the magnetic NWs in suspension with absolute ethanol and then ultrasonicating it for two minutes using sonic vibra cell, (Newtown, United States). A drop of this suspension was absorbed onto a carbon coated copper grid with a filter paper being used to absorb excess sample. The copper grid was then left overnight to air dry. The samples were then analysed using a TEM (FEI Tecnai T12 TEM) at MMU and HRTEM (JEM-2100). The dimensions of the NWs were analysed using ImageJ software. The standard error of the mean (HRTEM, TEM) has been used to specify the statistical uncertainty.

3.7.4.3 Quantification of the surface charge of the synthesised NWs

Surface charge affects the physical stability and the cellular interactions of the synthesised NWs. The NWs from the ethanol dispersion was first removed from the dispersion using an external magnet or centrifugation for the non-ferromagnetic Pt NWs, rinsed three times with deionised water and then redispersed and diluted with deionised water as well. The resultant NW suspensions were then placed into a consumable cell (DTS1070) and the zeta potential was measured using Malvern Zetasizer Nano.

3.7.4.4 Determination of the Crystalline Properties of the Synthesised NWs

The crystal structure of the synthesised NWs affects both the magnetic properties of the NWs and the cellular toxicity. The X-ray diffraction patterns were acquired for analysing crystalline phases by employing a MiniFlex 600 benchtop X-ray diffractometer (Rigaku, Tokyo, Japan) with Cu Kα radiation (λ = 1.54060 Å). The X-ray tube was set at a voltage of 40kV and a current of 15mA. The region of analysis $30^\circ \leq 2\theta \leq 90^\circ$ was evaluated.

3.7.4.5 Determination of the Outer Surface Composition of the Synthesised NWs

Different forms of Fe oxides present with different magnetic behaviours. To ensure desirable magnetic properties, the outer surface composition was determined to ensure that a ferromagnetic Fe oxide was formed.

The ethanol suspended NWs were pipetted onto a clean glass microscope slide and allowed to air dry. Thereafter it was analysed using a Horiba LabRAM HR Raman spectrometer with an Olympus BX41 microscope attachment. A low laser power of 0.4 mW was used so that the magnetite will not be converted to haematite as shown by de Faria *et. al.* (178). The 514.5 nm laser wavelength used was from a Lexel Model 95-SHG argon ion laser.

3.7.4.6 Characterisation of the Magnetic Properties of the Synthesised NWs

A vibrating sample magnetometer (VSM) (Quantum Design DynaCool, 12 T Physical Property Measurement System (PPMS)) was employed to study the magnetic properties of the synthesised NW. The readings were taken with the applied field parallel and transverse to the wire axis of the NWs embedded in the AAO template. The magnetic moments measurements were taken at 300 K and the magnetic field was swept in the range of ± 10000 Oe.

3.7.4.7 Evaluation of the Biocompatibility, Cytotoxicity, and Cellular Internalisation of Fe NWs and Pt NWs

Two testicular cancer cell lines were employed in this study viz. Tera-1 (Germ Cell Derived Testicular cancer) and 3T3 (Fibroblasts) and all experiments were carried out in triplicate. Tera-1 cells were obtained from Cellonex (Johannesburg, South Africa) and revived using McCoy's 5A supplemented with 20% foetal bovine serum (FBS) incubated at 37°C and 5% CO_2.

Tera-1 was first grown in a T-25 culture flask and then transferred to a larger T-175 culture flask. Tera-1 and 3T3 were cultured using RPMI 1640 supplemented with 10% foetal bovine serum (FBS) and 1% penicillin-streptomycin incubated at 37°C and 5%. The growth media was changed two to three times a week while simultaneously washing with phosphate buffered saline (PBS).

After the cells grew to a confluency of 70-80%, the cultured cells were dislodged from the T-175 culture flask using 2 mL of TrypLE™ while being incubated at 37°C and 5% CO_2 until they released from the flask. Once the cells were confirmed to be dislodged using an Olympus CKX53 Microscope the enzyme was diluted using cell specific growth medium to inhibit its activity and the suspension was centrifuged at 1000 rpm for five minutes at room temperature to collect the cells.

The supernatant was carefully removed making sure not to dislodge the pallet. The pallet was then redispersed up-to 15 mL using specific growth medium for each cell line. The suspension was then appropriately diluted, and the cells were stained using trypan blue and left for five minutes, to stain cells with damaged cell membranes.

The cells were then counted using a haemocytometer excluding the dead cells which were dyed blue. The experimental cells were then seeded into a 96-well plate using the following concentration in each well: Tera-1 (6000 cells/well), 3T3 (5000 cells/well) and A549 (3000 cells/well). The 96-well plates were then incubated for 24 hours at 37°C and 5% CO_2 allowing the cells to attach to the bottom of the plates.

The wells were then separated into groups and treated with 10 µL of either positive control (cisplatin/5-FU/DMSO); negative control (PBS); or with Fe NWs or Pt NWs. The 96 well plates were again incubated at 37°C and 5% CO_2 for 24 and 48 hours to assess the cell viability so that biocompatibility or cytotoxicity can be determined.

The % viability of the cells was determined using the (sodium 3´- [1- (phenylaminocarbonyl)-3,4- tetrazolium]-bis (4-methoxy6-nitro) benzene sulfonic acid hydrate) (XTT) assay. Briefly, 5 mL XTT labelling reagent was mixed with 0.1 mL electron coupling reagent for each 96-well plate immediately before use. 50 µL of the XTT labelling mixture was added per well and incubated for four hours at 37°C and 5% CO_2.

Spectrophotometric analyses were carried out for each well using a microplate (ELISA) reader. The absorbance was measured using a wavelength of 450 nm and the reference wavelength was measured at 690 nm. The % viability was calculated using the following formula shown in **Equation 3.3**:

Equation 3.3: Equation for the calculation of % Cell Viability

$$Cell\ Viability\ (\%) = \frac{absorbance\ value\ of\ treated\ cells - reference\ value\ of\ treated\ cells}{absorbance\ value\ of\ untreated\ (control)\ cells - reference\ value\ of\ untreated\ cells} \times 100$$

To determine if the NWs were internalised by the 3T3 and Tera-1 cells, The Cell lines were cultured, seeded, and treated as previously mentioned in a 96-well plate. After 48 hrs, the cells were washed thrice with PBS to remove the free floating non-internalised NWs. The interaction between the synthesised NW Platforms and the Cells were then investigated and imaged using phase contrast system (Olympus CKX53).

3.8 Results and Discussion

The synthesis of nanowires required rigour and precise laboratory practices. These practices included: a) environmental, b) controlling of oxidation, c) high quality voltameter, d) maintenance of a constant distance between electrodes, and e) adherence to developed protocols. The temperature of the laboratory was recorded and maintained at 22-20 °C. **Table 3.1** identifies the critical material attributes with the corresponding critical process parameters and critical quality attributes.

Table 3.1: Critical material attributes with the corresponding critical process parameters and critical quality attributes of the synthesised NWs.

Critical material attribute	Critical process parameters	Critical quality attribute
• Diameter size of NWs.	• Use of AAO templates with appropriate diameters of the nanopores.	• Uniform diameter distribution. • Magnetic behaviour and strength. • Potency. • Biocompatibility. • Toxicity.

• Length of synthesised NWs (high aspect ratio).	Pre-wetting of AAO template: • sonication time. • Sonication frequency. • Sonication power. • wetting time. Electrodeposition Process: • Deposition time. • Deposition voltage. • Composition of electrolytic bath. • Temperature control. • pH control. Release of NWs from AAO template: • Template dissolving time. • Etchant temperature, concentration, and composition. • Sonication time. • Sonication frequency. • Sonication power.	• Consistent length distribution of NWs. • Magnetic behaviour and strength. • Potency. • Biocompatibility. • Toxicity.
• Consistent morphology. • Composition. • Crystal structure.	• Extensive control of deposition voltage. • Design of electrolytic cell. • Consistency and formulation of electrolyte. • Temperature control. • pH control.	• Potency. • Biocompatibility. • Toxicity. • Magnetic behaviour and strength.

Oxidation of Fe content in the synthesised NWs naturally occurs when exposed to the template dissolution environment and air. This oxidation impacts the properties of the synthesised NWs. Therefore, synthesis protocols were strictly abided by to maintain consistency when synthesising the NWs. A high current, high end calibrated galvanostat (PGSTAT 302n) was used. The electrochemical cell used during synthesis was designed to allow ion migration. This design remained consistent throughout all experimentation.

Preliminary synthesis performed involved the use of aluminium (Al) plated AAO templates which served as the working electrode. The Al served as the contact interface between the working electrode and the external circuit. In addition, the initial AAO templates used contained a thin barrier layer which increased the resistance of the cells as there was no direct contact

between the Al contact layer and the nanopores of the template. This resulted in poor nanowire growth, morphology and yield as shown in **Figure 3.10**. To prevent this from happening the membrane was switched to a more conductive Au plated AAO template with an etched barrier layer.

Adequate wetting of the AAO template was a major contributor to the formation of uniform length NWs throughout the template. The nanopore diameters of the AAO template created a challenge in achieving sufficient pore-wetting. The consequence of poor pore-wetting was the formation of air bubbles in the nanopores which resulted in either no NW growth, regional NW growth, heterogenous NW growth, or regional overgrowth of NWs of the template. Hydrogen evolution and ion migration at the working electrode also posed a significant challenge in the production of uniform NWs. This challenge was addressed during the design of the electrolytic solutions used during synthesis and choosing the appropriate deposition voltage and methods. To produce high-quality NWs, the prementioned conditions were optimised. The proceeding discussion presents the optimised formulation and protocol used in the NW synthesis in this study.

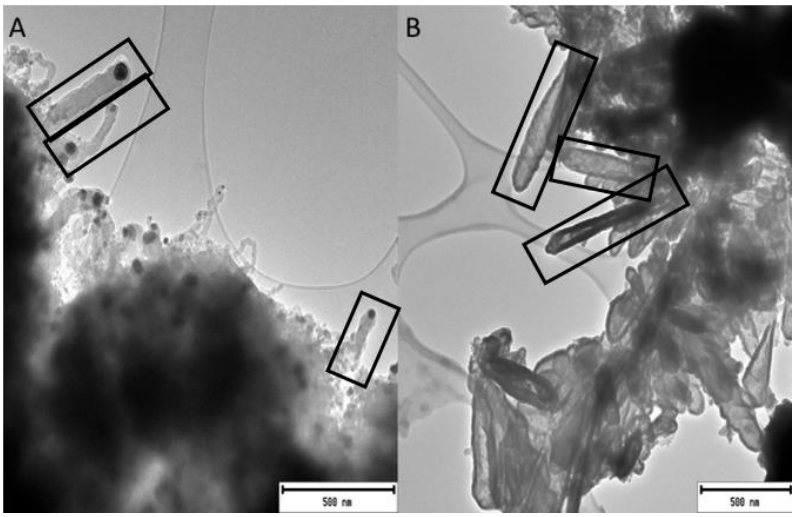


Figure 3.10: A and B) Images of preliminary NWs of inconsistent dimensions and structure synthesised during this study. Scale bar: 500 nm

3.8.1 Synthesis, Morphological Analysis, and Stability of Fe NWs

The electrolyte bath prepared for the syntheses of Fe NWs contained the following: 12% w/V $FeSO_4(7H_2O)$, 7.5% w/V Na_2SO_4, 2.5% w/V H_3BO_3 and 1% w/V $C_6H_8O_6$ (ascorbic acid). $FeSO4(7H_2O)$ provided the desired Fe^{2+} ion for the deposition of Fe NW. Na_2SO_4 acted as a supporting electrolyte, increasing the conductivity of the electrolyte. Boric acid was added to prevent the formation of hydroxide and increase hydrogen evolution overpotential while the ascorbic acid was added for its pro-oxidant activity which reduces unwanted Fe^{3+} to Fe^{2+} (179,180).

Cyclic voltammetry (CV) is a suitable technique to identify a metals growth potential from an electrolytic bath and was then used to determine the deposition potential where the Fe (II) will undergo reduction and form Fe (0) for the electrolyte of Fe NWs. A scan range for the CV analysis chosen was between 0 V to -3 V with a scan rate of 0.1 mVs^{-1}. 5 mL of the above electrolytic bath was analysed using a DropSens electrode (Metrohm DRP-C110) at 25 °C. Typically, the potential chosen for deposition was at a reducing potential where the current density begins to decrease.

Figure 3.11 is the CV analyses of the electrolyte used in the deposition of Fe NWs. As seen by the cathodic branch, the deposition potential starts to occur at -0.9 V. A deposition potential of -1.1 V was then chosen for the electrodeposition of Fe NWs which was well established in literature (78). There were two observed crossovers of the anodic and cathodic branches' current, which is typical of the nucleation process.

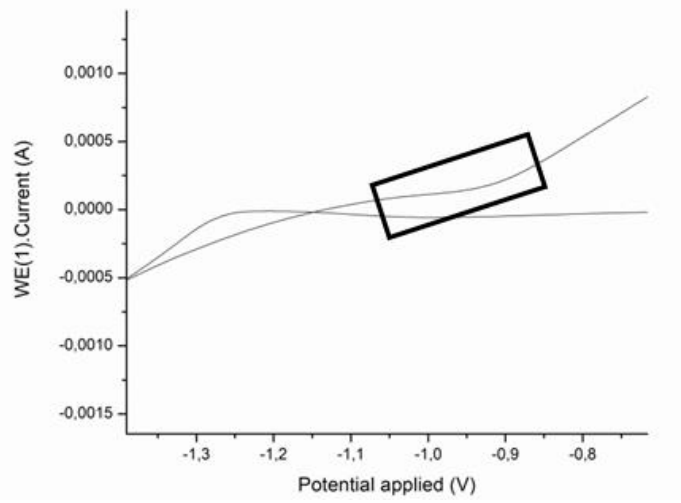


Figure 3.11: Graph of CV analyses of electrolytic bath of Fe NWs

Fe NWs was then synthesised and released using the methods and electrolytic cell previously described. The Current Vs Time profile measured for Fe NWs is shown in **Figure 3.12**. The electrodeposition of Fe NWs was halted before overgrowth from the nanopores in the AAO were observed to assist the release process of Fe NWs from the AAO template.

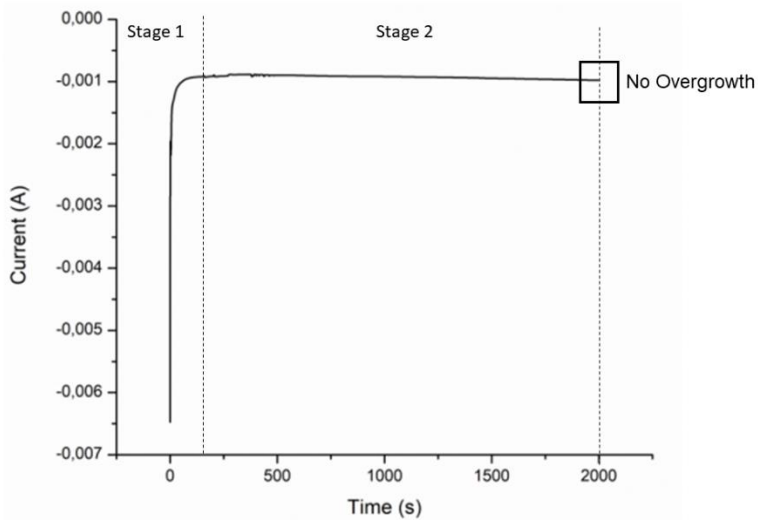


Figure 3.12: Image showing Current vs Time graph monitoring the growth of Fe NWs

The length of Fe NWs was then analysed using TEM microscopy. The desired length of Fe NWs was between 1 µm and 5 µm as it was intended for TC therapeutics. The obtained TEM images (**Figure 3.13**) were analysed using ImageJ software and a minimum of 100 NWs were measured to determine the average length. Fe NWs had an average length of 2.8 µm. However, it had a large standard deviation of 2.765 µm (Min= 0.313 µm /Max= 10.792 µm). Although standard error of the mean NW length for Iron core-shell NWs has been reported to in the range of 1.3 µm, as reported by Martínez-Banderas et al. (181).

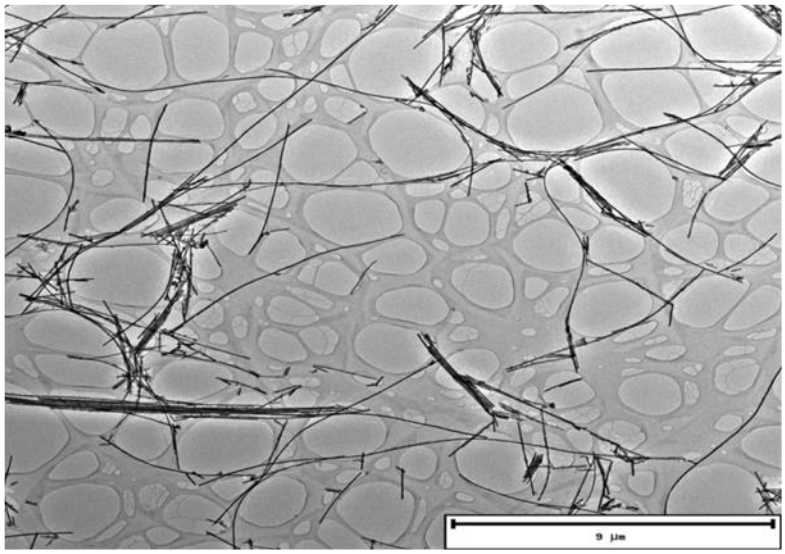


Figure 3.13: TEM image of Fe NWs showing large length variance of Fe NWs. Scale bar: 9 µm

Fe NWs was then analysed using HRTEM to determine the structural properties and morphology of the NWs. The low magnification images (**Figure 3.14**) clearly showed that NW were successfully synthesised with nominal diameters. The image illustrates that Fe NWs was less electron dense compared to Pt NWs (**Figure 3.19**). The images also show the fragmentation of Fe NWs. This was caused by the sonication step undergone during the releasing process of the NWs from the AAO template.

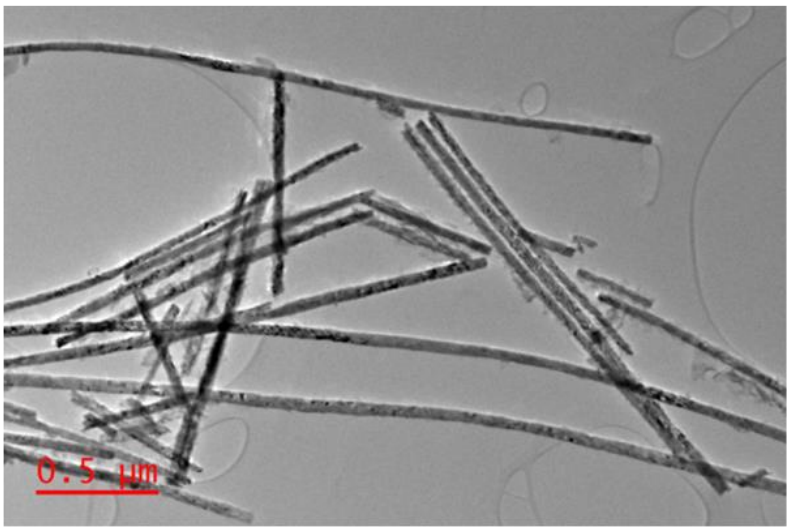


Figure 3.14: HRTEM image of Fe NWs depicting its morphology. Scale bar: 0.5 µm

The high magnification images of Fe NWs (**Figure 3.15**) depicted a clear core-shell structure with a core of Fe and an outer shell of amorphous Fe oxide which correlates to previous studies. This was due to the basic NaOH environment that the Fe from Fe NWs was exposed to during the releasing process which causes the outer layer of Fe NWs to oxidise. ImageJ was used to determine the average diameter and the thickness of the outer oxide layer using a minimum of 50 measurements for each. The outer amorphous shell had an average thickness of 3.9±0.5 nm and the average NW diameter of Fe NWs was 40±5.0 nm which was consistent with the average pore diameter of the AAO template.

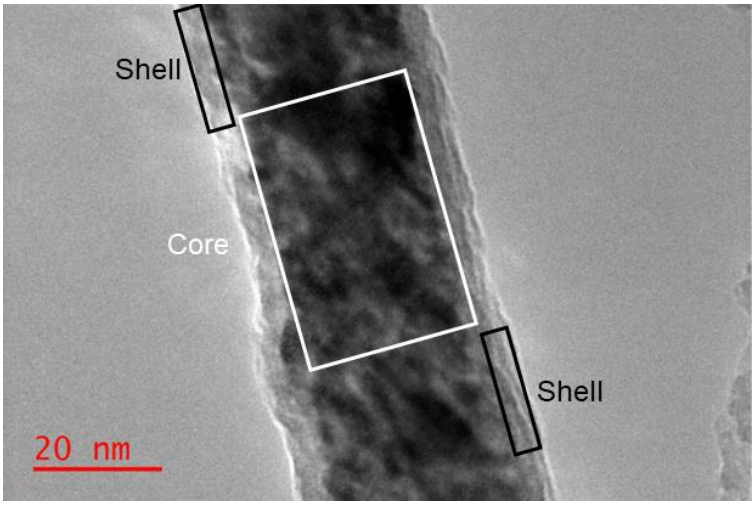


Figure 3.15: High magnification HRTEM image showing core shell structure of Fe NWs. Scale bar: 20 nm.

As seen in **Figure 3.14**, the Fe NWs tends to accumulate in clusters which was consistent with previous reports of magnetic NWs and has pharmaceutical ramifications. The clustering of Fe NWs impacted on its physical stability as the small NW clusters aggregated and sedimented in a brief period. This effect was undesirable as it affects dosing consistency, and the clusters can cause occlusions in the vascular system. However, this sedimentation effect was reversible as agitating the ethanol suspended Fe NWs, redispersed the suspension.

The physical stability of the NWs was analysed by measuring the surface charge (Zeta potential). The sample was prepared by aliquoting a determined amount of ethanol suspended Fe NWs in a 2 mL Eppendorf tube. The ethanol was then removed by collecting the ferromagnetic Fe NWs using an external magnet and removing the ethanol with a micropipette. Fe NWs was then redispersed in deionised water after three washes in deionised

water and then adequately diluted. The zetapotential measured for Fe NWs was -6.9±1.2 mV which is very close to neutral. Thus, Fe NWs was not electrostatically stable. The strong ferromagnetic behaviour of Fe NWs and the almost neutral zetapotential pronounced the sedimentation effect of Fe NWs.

3.8.2 Synthesis, Morphological Analysis, and Stability of Pt NWs.

The electrolytic bath for Pt NWs contained 1% w/v H_2PtCl_6 and 7% $HClO_4$. The chloroplatinic acid provided the Pt^{4+} ions desired for the deposition of Pt NWs. Perchloric acid acted as a supporting electrolyte by increasing the conductivity of the electrolytic bath and control the pH of the electrolytic bath. CV analyses was performed on the electrolyte used to deposit Pt NWs in the nanopores of the AAO template to determine the growth potentials for Pt using a scan rate of 0.1 V/s (**Figure 3.16**).

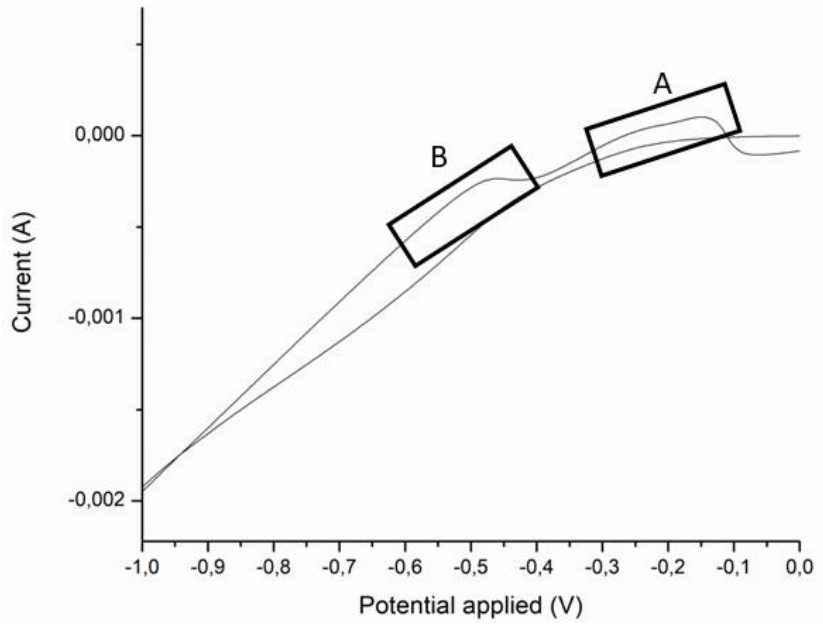


Figure 3.16: CV analyses for electrolytic bath of Pt NWs. **A)** Pt^{4+} reduction, **B)** hydrogen evolution

It was observed that the reduction potential range for the electroactive species, Pt^{4+}, started at ~-0.10 V **(A)**. The reduction of Pt^{4+} at this potential was controlled by the electron transfer rate. The current steadily decreased for an increasing negative potential until it plateaued at ~0.40 V. This indicates that the additional Pt centres were deposited on the electrode which

was regulated by the mixed control process. The observed plateaued region between ~0.40 V and ~-0.48 V indicating that Pt centres were still being deposited and regulated by mass transfer process. Beyond the plateaued region at negative potentials greater then ~-0.48 V **(B)**, there was a sharp current decrease for an increasing negative potential. At this point, a great deal of bubbles was observed being generated by the DropSens electrode which can be attributed to hydrogen evolution. The desired growth potential for Pt^{4+} in the electrolyte used to deposit Pt NWs can therefore be concluded to be between ~-0.10 V and ~-0.48 V. the potential chosen for the potentiostatic deposition of Pt NWs was -0.35 V which was previously used in the literature (182).

Pt NWs was then synthesised, released from the AAO template using the methods and electrolytic cell design previously described. The Current vs Time graph measured for Pt NWs is shown in **Figure 3.17**. The electrodeposition of Pt NWs was stopped before overgrowth from the nanopores were observed to facilitate the release process from the AAO template.

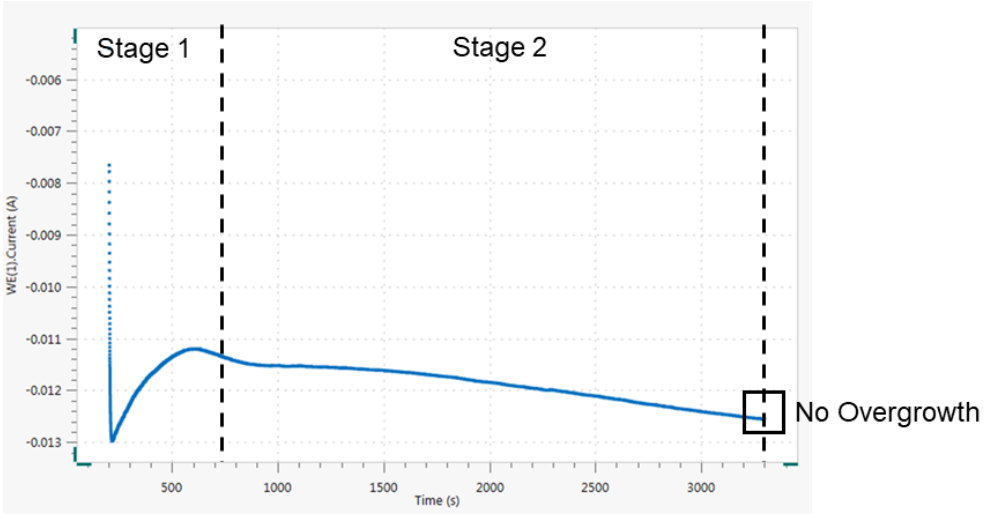


Figure 3.17: Current vs Time graph monitoring growth of Pt NWs

The length of Pt NWs was then analysed using TEM with the same target length as for Fe NWs. The obtained TEM images of Pt NWs (**Figure 3.18**) were measured for NW length using ImageJ software and a minimum of 100 NWs. Pt NWs had an average length of 2.2±1.2 µm.

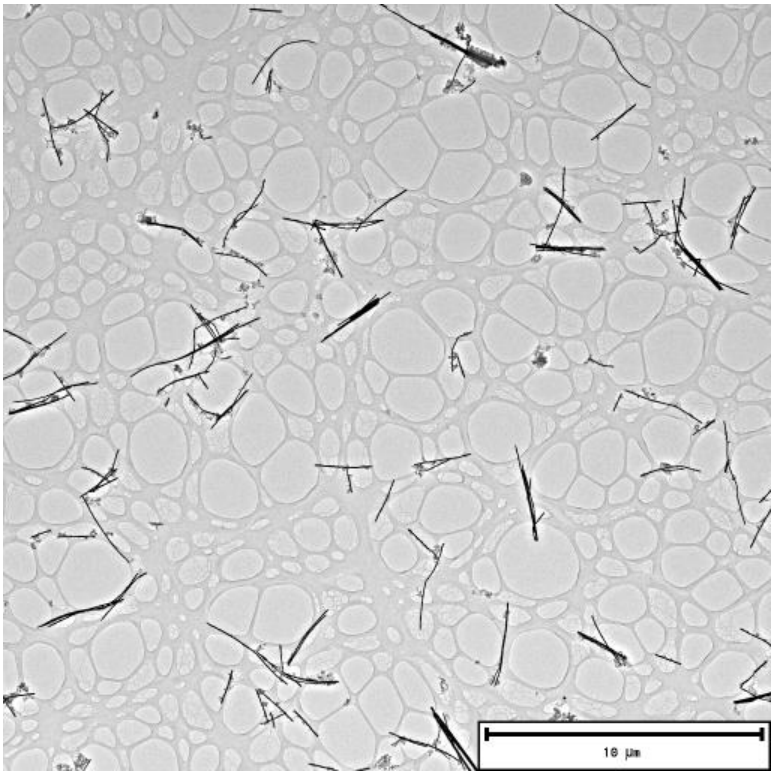


Figure 3.18: TEM image showing length distribution of Pt NWs. Scale Bar: 10 µm.

Figure 3.19 corresponds to low magnification HRTEM images of the synthesised Pt NWs. It clearly depicts the successful synthesis of NW with smooth consistent morphology with nominal diameters. The image also shows the fragmentation of Pt NWs which is accounted for by the breakup of Pt NWs during sonication process. Pt NWs also displays a greater electron density compared to Fe NWs.

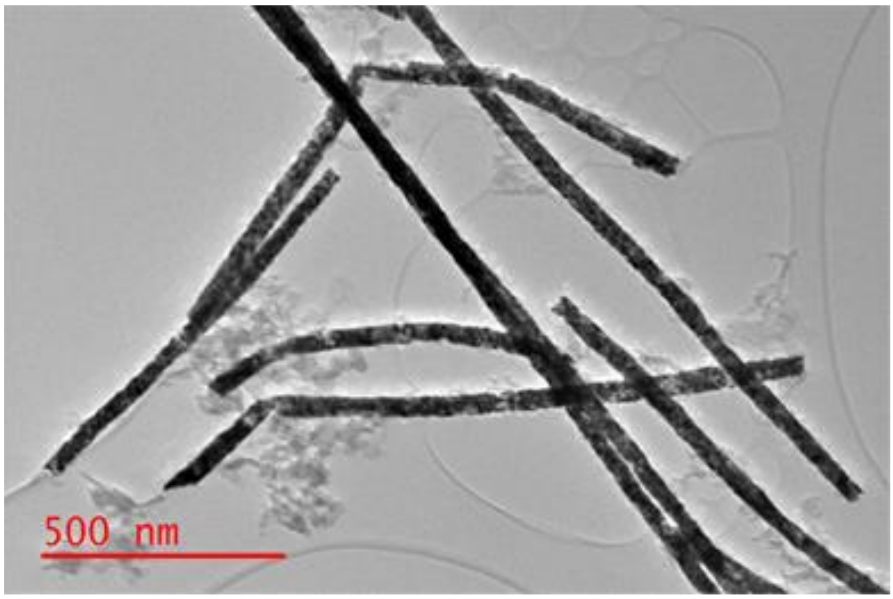


Figure 3.19: HRTEM images of Pt NWs depicting the morphology of Pt NWs. Scale bar: 500 nm.

Higher magnification images of Pt NWs were also studied using HRTEM corresponding to **Figure 3.20**. Interestingly, Pt NWs was observed to have a polycrystalline structure as shown with the planes randomly arranged and nonconstant interplanar spacing. The grains are not well defined due to the high electron density of Pt. An average NW diameter of Pt NWs was 39±2.0 nm which was consistent with the average pore diameter of the AAO template was measured using ImageJ. No outer oxide layer was observed for Pt NWs.

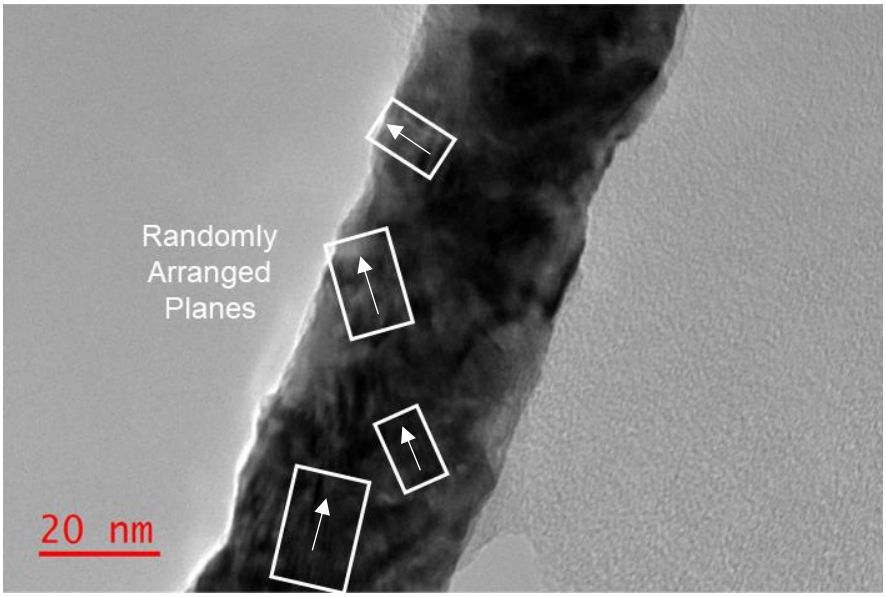


Figure 3.20: High magnification HRTEM image of Pt NWs showing the polycrystalline nature of Pt NWs. Scale bar: 20 nm.

Pt NWs was macroscopically observed to have greater physical stability compared to Fe NWs. However, they still formed a sediment which was easily reversible with slight agitation. Pt NWs was prepared for zetapotential analyses as previously described. Pt NWs had a moderate zetapotential of -22.3±1.1 mV and no remnant magnetization acting on it.

3.8.3 Analysis of the Crystalline Structure, Crystallite Size and Interplanar Spacing of Fe NWs and Pt NWs Using Powder XRD

Magnetic anisotropy is dependent on the crystallographic orientation which results in preferred orientations of magnetic moments. The crystal structure of the synthesised NWs affects the cellular toxicity of the NWs. The crystallite structure of the synthesised NWs was therefore confirmed, and the crystallite size and d-value were estimated by studying the XRD patterns of the synthesised NWs. **Figure 3.21 (A)** and **Figure 3.21 (B)** respectively depicts the obtained diffractograms for Fe NWs and Pt NWs; and **Table 3.2** summarises the calculated crystallite size (Scherrer equation) (183) and d-value (Bragg's law) (184).

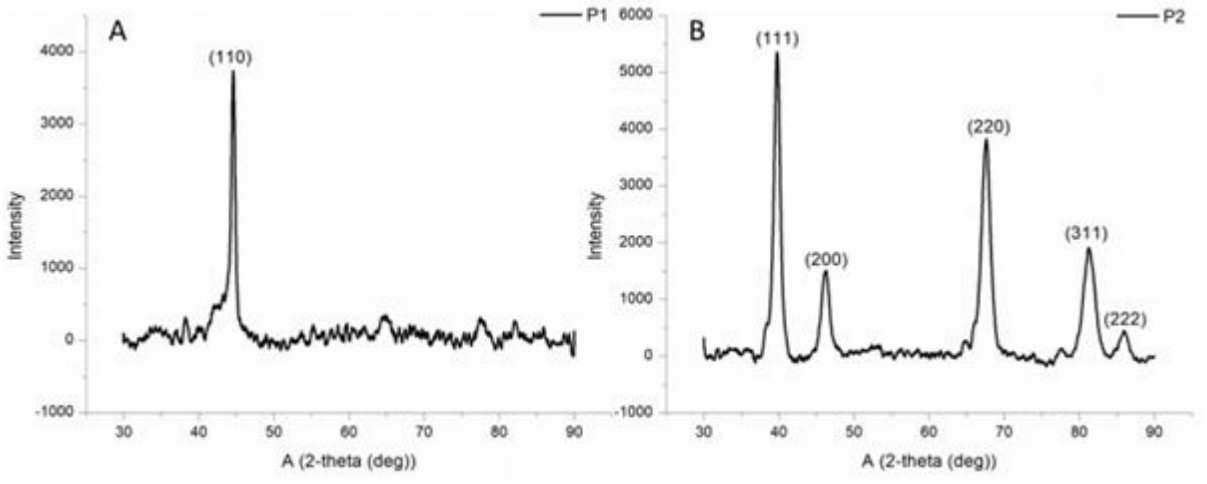


Figure 3.21: Powder XRD diffractograms of Fe NWs and Pt NWs embedded in AAO template. **(A)** Fe NWs**, (B)** Pt NWs.

Fe NWs showed an intense singular peak at 2 θ value 44 ,56° indicating that Fe NWs preferred the (110) plane in a cubic crystal system. A single crystal structure is preferable in harsh environment applications such as at a tumour site. This is due to the naturally formed outer oxide layer around a polycrystalline Fe NW continuously grows in harsh environments until the disappearance of the Fe core. The outer oxide layer of Single crystal Fe NWs on the other hand grow a finite amount (~10nm) and the Fe core is maintained (78). Thus, increasing the stability of the magnetic properties of Single crystal Fe NWs which is favourable in MTD.

Pt NWs was indexed to five main peaks at 2 θ values of 39.75°, 46.20°, 67.56°, 81.31°, and 85.90° corresponding to planes (111), (200), (220), (311), and (222) in a Pt cubic crystal system. This corresponds to the polycrystalline nature of Pt NWs imaged by the high magnification HRTEM image of Pt NWs. This was advantageous for a therapeutic system as polycrystalline Pt NWs have been shown to be chemically stable as the composition of the Pt NWs was not altered with intense pH changes (185).

Equation 3.4: Bragg's equation used to calculate d spacing:

$$n\lambda = 2d \sin\theta$$

Equation 3.5: Scherrer equation used for the calculation of crystallite size:

$$D = \frac{Ks\lambda}{\beta \cos \theta}$$

Braggs law was used to calculate the inter-planar spacing (**Equation 3.4**) where n is the diffraction order, λ is the wavelength of the X-ray source, d is the inter-planar spacing, and θ is the peak position (radians). Scherrer equation (**Equation 3.5**) was used to estimate the crystallite sizes in the deposited NWs. Ks is the shape factor, 0.9 as used by Terohid *et. al.* for tungsten oxide nanowires (183), λ is the wavelength of Cu Kα, β is the full width at half maxima (FWHM) in radians of the observed peaks, θ is the peak position in radians, and D is the crystallite size in nm. The estimated crystallite sizes were smaller than the diameter of Pt NWs (39 nm) indicating that these NWs are polycrystalline as well as confirmed by the HRTEM. Since individual crystallites have a minimum of one magnetic domain, Pt NWs, Fe coated Pt NWs, and Fe-Pt NWs can be considered to have a complex multi-domain state.

Table 3.2: Analyses and interpretation of obtained powder XRD diffractograms using Scherrer equation for crystallite size and Braggs law for d-value.

NW Platform	Composition	2 θ	β (FWHM)	Crystallite Size (nm)	d (Å)	h k l
Fe NWs	Fe	44.6	0.88795	8.28	2.03	110
Pt NWs	Pt	39.7	1.05578	7.08	2.27	111
	Pt	46.2	1.33413	5.48	1.97	200
	Pt	67.6	1.49182	4.43	1.39	220
	Pt	81.3	1.82394	3.30	1.18	311
	Pt	85.9	1.33386	4.36	1.13	222

3.8.4 Analysis of the Outer Surface Composition of Fe NWs and Pt NWs Using Raman Spectroscopy

An outer oxide layer on Fe NWs was developed during the release process of the NWs from the AAO template as observed by the HRTEM. This layer was naturally formed when the Fe from each type of NW was in the presence of NaOH and air. The oxides formed during this process has implications on the magnetic properties and the attachment potential for coatings and small molecules used in engineered smart delivery nanoparticle systems for active drug targeting. It was therefore necessary to determine the composition of the outer oxide layer which was accomplished using Raman Spectroscopy (**Figure 3.22**).

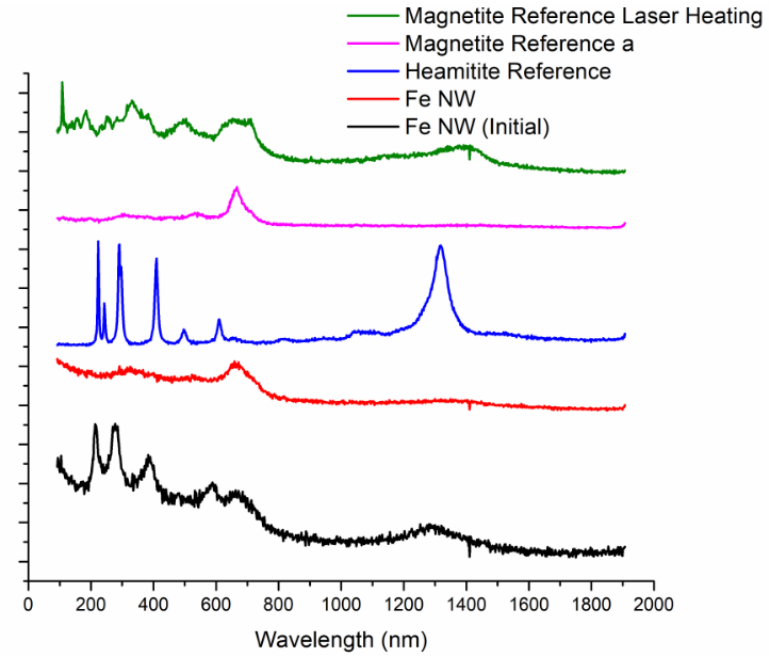


Figure 3.22: Raman spectrums of the initial scan of Fe NWs with a high laser power, Fe NWs, a reference scan for heating magnetite with a laser, magnetite, and haematite.

It is a well-known fact that when magnetite is heated, it forms haematite (186). The initial Raman scans for the Fe NWs showed the presence of both haematite and magnetite characteristic peak. The haematite characteristic peaks are located at 217 cm^{-1} (A_{1g}), 275 cm^{-1} (E_g), 386 cm^{-1} (E_g), 583 cm^{-1} (E_g), and 1304 cm^{-1} (E_g) while the magnetite characteristic peak can be seen at 669 cm^{-1} (A_{1g}) (178). When the laser intensity was decreased and larger agglomerates of Fe NWs were analysed to decrease the effect of laser heating of Fe NWs on haematite formation, only peaks characteristic of magnetite was found. The spectrum obtained from Fe NWs in the Raman spectroscopy measurements displayed peaks located at 322 cm

$^{-1}$ (E_g), 528 cm $^{-1}$ (T_{2g}), and 667 cm $^{-1}$ (A_{1g}). These peaks correspond to a typical Raman spectrum of magnetite which was desired due to its magnetic properties, good biocompatibility, and attachment potentials of biomaterials.

3.8.5 Evaluation of the Magnetic Properties and MTD Potential of Fe NWs and Pt NWs Using VSM.

The efficacy for MTD is directly proportional to the ability of the NWs to be coupled to an external magnetic field. For successful MTD, the magnetic force on the synthesised NWs will need to overcome the forces present in the capillary system, mainly the viscous drag force, where the NWs will be trapped and removed from the vascular system and guided to the target area. It is well known that shape anisotropy and crystallinity influence the magnetic properties of nanomaterials. The magnetic properties of Fe NWs and Pt NWs was therefore studied by employing a VSM at 300 K.

Figure 3.23 represents the normalised M-H loops for Fe NWs within the AAO template with the applied magnetic field parallel and transverse to the long axis of the NWs. As shown, the normalised M-H loops predominantly shows ferromagnetic behaviour. Ferromagnetic materials are strongly attracted to a magnetic field. The normalised M-H loop measured parallel to the NW long axis shows a more rectangular structure and has a squareness ratio of M_R/M_S = 0.50 compared to a more tilted M-H loop with the applied field transverse to the NW long axis with a M_R/M_S = 0.02. It can therefore be seen that the magnetic easy direction was along the long axis of the NW which was consistent with previous reports (78,140,187). This was due to the strong shape anisotropy of Fe NWs. The M_S of Fe NWs parallel to the long axis was 2.2 x 10^6 A/m and the Hc was determined to 713 Oe, indicative of soft magnetisation. A high M_R of 1.1 x 10^6 A/m was measured which was characteristic of single crystal Fe NW consistent also with single diffraction peak [110] of **Figure 3.21** (78). The M_s of Fe NWs was larger than that of bulk polycrystalline Fe which was 1.7 x 10^6 A/m (188). A similar observation was found by Al Sharif et. al. who synthesised Fe NW using pulsed electrodeposition employing −60 mA pulses of a duration of 2 ms for an hour. They measured a Ms of 427 Am^2/kg or ~3.4 x 10^6 A/m when testing Fe NW embedded in the AAO template using a VSM (11). Fe NWs also required a low magnitude applied field strength to reach saturation of 2600 Oe which can easily be supplied by modern magnets which is advantages in a MTD systems.

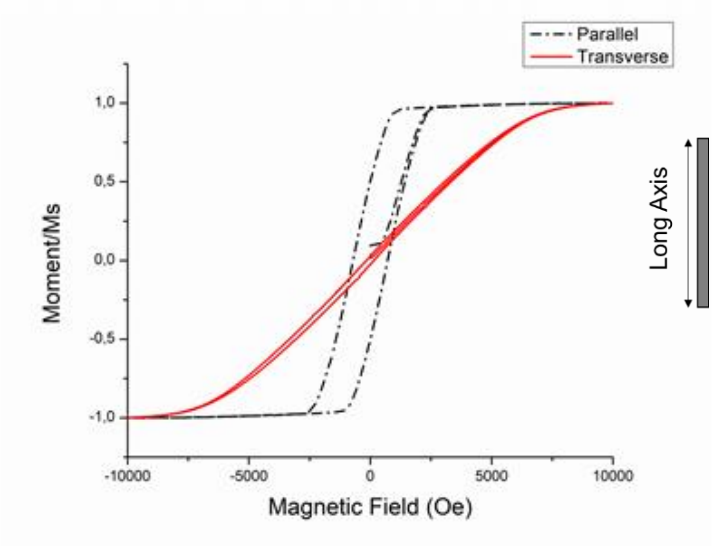


Figure 3.23: Normalised M-H Loop of Fe NWs with the long axis of the NW parallel and transverse to the direction of the applied field.

Figure 3.22 shows the normalised M-H loops for Pt NWs. Pt NWs was analysed with the field both parallel and transverse to the long axis of the NW. Interestingly, along the parallel axis, Pt NWs displayed diamagnetic properties where magnetisation decreased for increasing field strength. Along the transverse axis, Pt NWs showed superparamagnetic properties. Superparamagnetic materials are attracted to external magnetic fields.

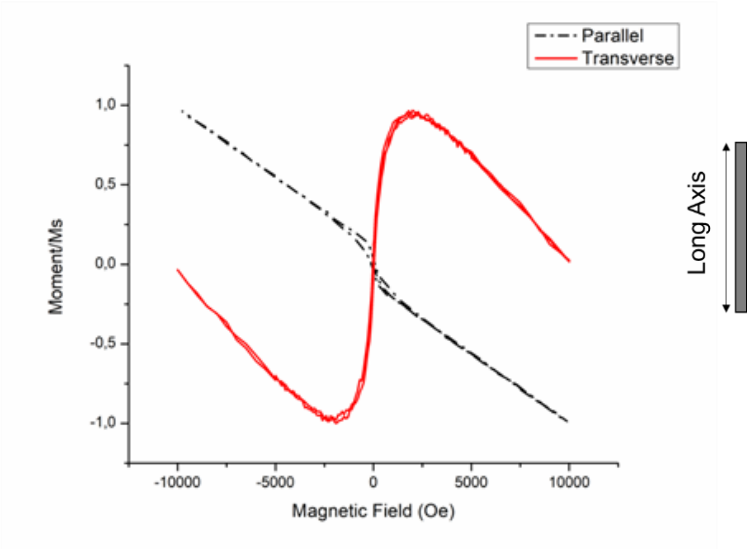


Figure 3.24: Normalised M-H Loop of Pt NWs with the long axis of the NW parallel and transverse to the direction of the applied field.

As the goal of this study was to synthesise a NW platform capable of MTD. Therefore, a platform that will be attracted towards a magnetic field with a sufficient Ms at low H was desired. This will allow the NW platform to be trapped and extracted from the bloodstream and transported to the target site. The magnetic properties of Fe NWs fit this profile and was therefore suitable as a MTD platform. Pt NWs on the other hand, displayed both diamagnetic behaviour and superparamagnetic behaviour. This competing property does not allow Pt NWs to be attracted by a magnet as the orientation of the NW cannot be controlled when released from the AAO template, thus making Pt NWs not suitable for MTD. The use of Pt NW would necessitate large magnetic field which may have adverse effects on the human tissue.

3.8.6 Cytotoxicity and Cellular Internalisation of the Synthesised NW Platforms

3.8.6.1 Cytotoxicity of NW Platforms on Mouse Fibroblasts

The biocompatibility of Fe NWs and Pt NWs was assessed by observing the effect of the synthesised NW platforms on % viability 24 hours (hrs) and 48 hrs after treatment on a non-cancerous fibroblast 3T3 cell cultures using the XTT assay (**Figure 3.25**). The concentrations for treatment used for Fe NWs were 32, 16, 8, 4, and 2 µg/mL while the concentrations used for the Pt NWs was 320, 160, 80, 40, and 20 µg /mL.

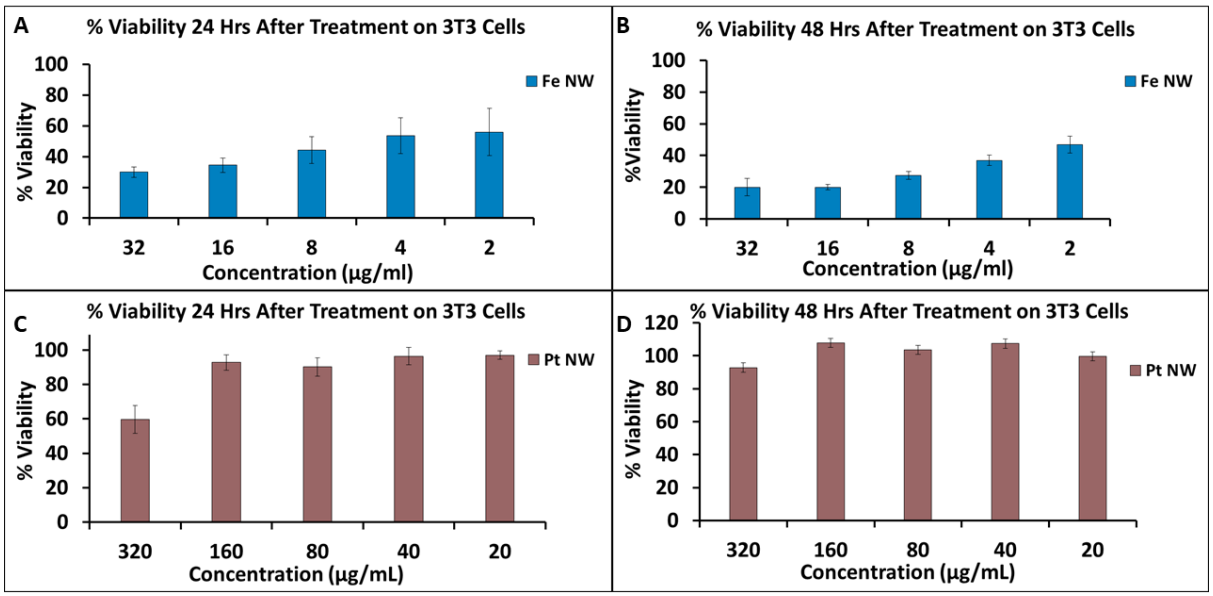


Figure 3.25: % cell viability of 3T3 cells **A)** after 24 hrs treatment with Fe NWs, **B)** after 48 hrs treatment with Fe NWs, **C)** after 24 hrs treatment with Pt NWs, **D)** after 48 hrs treatment with Pt NWs

This corresponds to a concentration of ~2400, ~1200, ~600, ~300, ~150 NWs/cell for Fe NWs and the concentrations for Pt NWs corresponded to ~11200, ~5600, ~2800, ~1400, ~700 NWs/cell. These concentrations are much greater compared to the targeted concentrations in potential biomedicine applications. These high concentrations were chosen to investigate the effects of the NW composition on the NW platforms short-term acute toxicity.

Fe NW and Fe-Fe_3O_4 NW have been assessed in the literature for biocompatibility and was considered to have low toxicity. Song *et. al.* tested high concentrations (10000 NWs/Cell) of polycrystalline Fe NWs (50 nm diameter and 5 µm length) over a 72 hrs period on HeLa cells and found a high cell viability of 80% (126). However, after 24 hrs and 48 hrs treatment, Fe NWs displayed a significant decrease in cell viability of 3T3 cells, 30% and 20% respectively at the highest tested concentration of 32 µg/ml (2400 NWs/Cell).

This could be accounted for due to the difference in cell lines tested, the difference in crystallinity (single crystal) and the different dimensions of Fe NWs (40nm diameter and 2.8µm length) as smaller particles tend to have greater cytotoxicity (136). Single crystal Fe NWs was shown to have greater toxicity compared to polycrystalline Fe NWs by Ivanov *et. al.* likely due to the prevention of intracellular dissolution of the NWs due to the passivation provided by the Fe oxide shell (78,177).

Using phase contrast microscopy, the morphology of the 3T3 cells showed shrinkage and a change in shape to round and oval which was not present in untreated cells after 24 hrs and 48 hrs (**Figure 3.26**). It can be concluded that Fe NWs significantly decreased the % cell viability of 3T3 cells and can therefore be considered cytotoxic at these relatively high concentrations. The image clearly shows that Fe NWs was internalised by the cells.

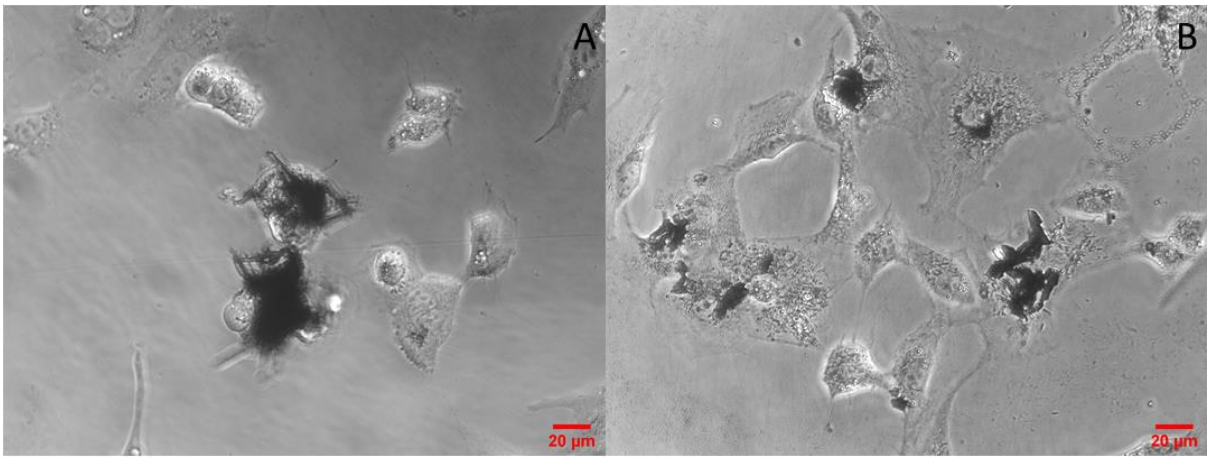


Figure 3.26: Phase contrast images of 3T3 cells after **A)** 48 hrs treatment with Fe NWs, **B)** 48 hrs treatment with Pt NWs. Scale bar: 20 µm

Pt (II) complexes such as cisplatin have been widely used for cancer therapeutics with good effect. They do however have major drawbacks due to their non-selectivity bringing about severe adverse effects and drug resistance. Pt (0) such as in nanoparticles have also been examined to evaluate their cytotoxicity and was suggested to cause oxidative stress which leads to a loss in cell viability (189).

The effect of the change in morphology of Pt (0) nanoparticles towards a NW anisotropy on cytotoxicity was evaluated in this research as well. The cell viability for 3T3 cells treated with Pt NWs showed no significant decrease and stayed at ≥90% except at the highest concentration of 320 µg/mL at the 24 hrs time point. At 48 hrs, the cells at the same concentration showed significant recovery with a cell viability of >90 % and cell morphology looking healthy as shown in **Figure 3.26** indicating that Pt NWs was not cytotoxic to 3T3 cells at these high concentrations even though they were clearly internalised by the cells.

3.8.6.2 Cytotoxicity Assessment of the Synthesised NWs

To assess the cytotoxic activity of the synthesised NWs against testicular cancer. Tera-1 cells treated with the synthesised NW platforms were incubated with varying concentrations for 24 hrs and 48 hrs and the %viability was tested using XTT assay (**Figure 3.27**). The concentrations chosen for treatment with Fe NWs was 32, 16, 8, 4, and 2 µg/mL while the concentrations chosen for the Pt NWs was 320, 160, 80, 40, and 20 µg/mL. The same concentrations as used for 3T3 was chosen to have comparative results to the cytotoxic

activity for the different cell lines. These concentrations expressed as NWs/Cell for Fe NWs are: ~1600, ~800, ~400, ~200, and ~100 NWs/Cell; Pt NWs: ~8800, ~4400, ~2200, ~1100, ~550 NWs/Cell.

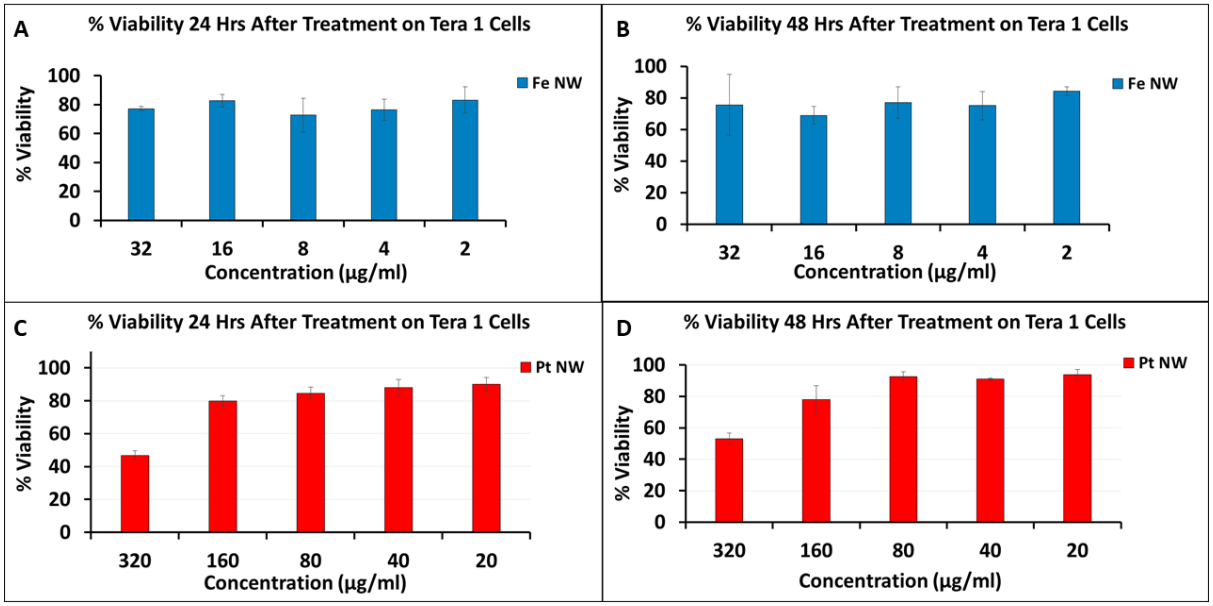


Figure 3.27: % cell viability of Tera-1 cells **A)** after 24 hrs treatment with Fe NWs, **B)** after 84 hrs treatment with Fe NWs, **C)** after 24 hrs treatment with Pt NWs, **D)** after 48 hrs treatment with Pt NWs.

Both Fe NWs and Pt NWs clearly demonstrated that they are internalised by the Tera-1 cells (**Figure 3.28**). Pt NWs displayed inherent toxicity against the Tera-1 cell in a dose dependent manner for higher concentrations. Fe NWs however, displayed a constant decrease of cell viability of ~20% at both 24 hrs and 48 hrs. The cells treated with Fe NWs also showed a slight change in morphology of the treated cells displaying a more rounded shape.

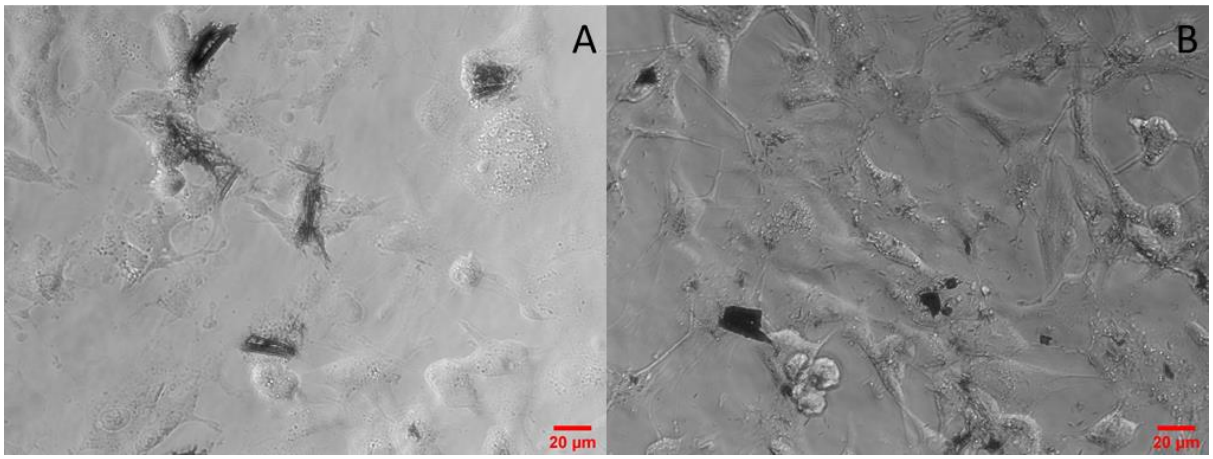


Figure 3.28: Phase contrast images of Tera-1 cells after **A)** 48 hrs treatment with Fe NWs, **B)** 48 hrs treatment with Pt NWs. Scale bar: 20 µm

Pt NWs revealed significant cytotoxic activity at a high concentration of 320 µg/mL and had a high IC_{50} of 354 µg/mL at 48 hrs. Pt NWs also showed a slight cell recovery at 48 hrs for lower concentrations (**Figure 3.27).** It should be noted that the chosen concentrations tested for both 3T3 and Tera-1 are far greater than what was the envisioned concentrations in the bloodstream and healthy tissue. However, due to the nature of MTD, it was anticipated that these concentrations will be reached at the target site.

3.9 Concluding Remarks

Fe and Pt NWs were successfully synthesised. Fe NWs displayed Single Fe crystal structure with an amorphous magnetite coating creating a core shelled structure. Fe NWs presented the most promising magnetic properties for MTD. Fe NWs displayed clear ferromagnetic behaviour with large M_S and Hc. However, Fe NWs was not bioactive against Tera-1. Therefore, the most promising application of Fe NWs is in the future development of a nanocarrier for a selective release actively targeted drug delivery system. Pt NWs exhibited a polycrystalline structure and displayed inherent bioactivity against Tera-1 cells at high concentrations. Pt NWs displayed a high IC_{50} of 354 µg/mL at 48 hrs. Pt NWs however, displayed unfavourable competing magnetic characteristics that were not suitable for MTD.

CHAPTER 4.

Modulation of Fe NWs and Pt NWs to enable multifunctionality through the Development of Fe/Pt Composite NWs

4.1 Introduction

Despite recent advances in cancer therapeutics, cancer retains high mortality and incidence rates (27,190). Most chemotherapeutic approaches primary targets are intracellular (191). Current chemotherapy delivery methods widely disperse the drugs throughout the body. Thus, leading to severe and a high quantity of adverse reactions experienced by patients (192). This drawback elicits a change in strategies used for cancer therapeutics. Moving towards image-guided (80,193), targeted delivery systems (194), which concentrate actives at required sites. Thus, steering away from extensively dispersing the actives throughout the body, which leads to a wide range of severe adverse reactions.

The previous chapter discussed the synthesis of Fe and Pt NWs with the aim of creating a magnetically active NW that was selectively active against TC. Pt NWs displayed inherent selective cytotoxic activity against Tera-1 cells, but their magnetic properties were not suitable for MTD. Fe NWs on the other hand were not bioactive against Tera-1 cells and were cytotoxic to 3T3 cells. Their magnetic properties were however advantages towards MTD.

This chapter will briefly review the contemporary methods used in the modulation of regular NWs. Thereafter this chapter will explore two modulation methods with the aim of modulating Pt NWs with Fe creating Pt/Fe composites. The purpose being the coalescence of the inherent cytotoxic activity of Pt (0) NWs on Tera-1 cells with the ferromagnetic behaviour of Fe NWs. The first modulation method was a cost-effective novel synthesis technique not requiring ALD by utilising template electrodeposition to synthesise a Fe/Pt composite with a core shell structure. This Fe/Pt composite will consist of a Pt core and Fe shell (Fe coated Pt NW). The second type of Fe modulation to create a Fe/Pt composite evaluated in this chapter was an alloy consisting of both Fe and Pt (Fe-Pt NW). The NWs will be characterised to determine their structure and magnetic properties. Their cytotoxic activity will then be evaluated on Tera-1 and 3T3 cells.

4.2 Basis for the Synthesis of Regular and Modified NWs Using Template Electrodeposition as Established in the Literature

Magnetic NWs can be synthesised in various forms, from regular NWs with a single element and consistent diameters to multi-layered NWs alternating between a magnetic element and a non-magnetic element. Each form of NWs possesses their own unique properties which can be tailored to a desired application.

Although the method and synthesis of regular NWs of a single element was discussed in chapter three, regular NWs can also comprise of metallic alloys. Though multiple synthesis techniques can be used to synthesise regular Magnetic NWs, template electrodeposition remains a simple cost-effective technique. Alloy Magnetic NWs can be synthesised in a single electrolytic bath and its composition and crystal structure can be tailored by adjusting the electrodeposition conditions such as adjusting the concentration, temperature, and pH of the electrolytic bath or the deposition current or potential (195). One of the primary advantages of regular Magnetic NWs is that the shape anisotropy aligns the magnetic moments along the long axis of the magnetic NWs, positively influencing the magnetic properties.

Multi-layered Magnetic NWs holds distinctive physical properties which make them advantages in biomedical applications. There are two main methods of synthesising multi-layered magnetic NWs using template electrodeposition. Namely, using single or dual electrolytic baths, the latter of which has a longer history that goes back to 1921 (196,197). In a dual electrolytic bath system, each bath was used to deposit a singular element (layer) and the template was rotated between the two. The disadvantage of this method was the continuous transfer of the template between the two baths introduces contaminates. In the single bath method, both layers are deposited from a single electrolyte that contain the ions needed to be reduced to form each layer (156). In this method, the layers are formed using pulsed electrodeposition techniques by pulsing either current or potential. Each ion that needs to be reduced has their own reduction potential with one being more positive (element A) than the other which is more negative (element B). When element A is reduced at its reduction potential a pure layer of element A will be formed as the potential is not sufficient to reduce element B. When the system is pulsed at the reduction potential of element B, both element A and B will be deposited forming an alloy. The composition of this alloy can be tailored by adjusting the concentration of element A so that the layer is element B rich (140). Multi-layered NWs such as Ni/Cu and Fe/Au have been successfully synthesised using single bath template electrodeposition (198,199).

Core-shell Magnetic NWs consist of an inner central structure (core) encapsulated with another material (shell). Multiple methods have been used to synthesise core-shell Magnetic NWs including ALD, Vapour-Liquid-Solid (VLS) and template electrodeposition. There are multiple strategies used to synthesise core-shell Magnetic NWs using template electrodeposition. One strategy is to use ALD to create the shell in the nanopores and then electrodeposition to deposit the core (200). Another strategy that uses a two-step process as well is to coat the inner surface of the nanopores in a AAO template creating nanotubes using methods such as sol-gel or electrodeposition. Thereafter the core is electrodeposited completing the core-shell structure (201,202). A third strategy used to synthesise core-shell Magnetic NWs is to electrodeposit metallic NWs and thereafter release them from the AAO template. The released NWs are thereafter coated with a metal using chemical reactions (203).

Diameter modulated NWs are NWs whose diameters are intentionally changed in a controlled manner to create NWs with alternating larger and smaller diameters along the long axis of the NW. This type of modulation is achieved by modifying the diameter of the nanopores in the AAO template during the adonisation process creating areas with larger and smaller diameters. Electrodeposition is thereafter carried out in these modulated AAO templates (204).

4.3 Methods and Materials

4.3.1 Materials

The experimental materials used during this chapter are the same as those listed in Chapter 3, Section 3.7.1.

4.3.2 Synthesis of Fe coated Pt NW

A novel three step synthesis method was used to create an Fe coated core-shell NW. A distinctive advantage of this method described was greater control of the diameters of the core of the NW. This property can be exploited in tailoring the magnetic and cytotoxic properties of the NW.



Figure 4.1: Schematic of the longitudinal cross-section of the prototype Fe coated Pt NWs depicting the layout of the core shell structure

4.3.2.1 Step One of Fe Coated Pt NW Synthesis: Deposition of Pt into the Channels of the AAO Template

Fe coated Pt NWs was synthesised in a multistep process. The first step involved synthesising Pt NWs through the deposition of Pt into the AAO template as explained in Chapter 3, Section 3.7.2.2.

4.3.2.2 Step Two of Fe Coated Pt NW Synthesis: Pore Widening of the AAO Template Nanopores with Deposited Pt

The diameter of the nanopores within the AAO template was then increased utilising the method employed by Liyuan *et. al.* (149). The Pt Deposited AAO templates thoroughly cleaned and wetted by sonicating them for 10 s. The AAO templates were then submerged in 5% H_3PO_4 for a given time at 25°C to partially dissolve the AAO template creating a wider pore diameter.

4.3.2.3 Step Three of Fe Coated Pt NW Synthesis: Deposition of Fe in the Space Created During the Pore Widening Step

The space created between the Pt NW and AAO nanopores was then deposited with Fe using pulsed templated electrodeposition in the following electrolytic bath: 12% w/v $FeSO_4(7H_2O)$, 7.5% w/v Na_2SO_4, 2.5% w/v HBO_3 and 1% w/v ascorbic acid.

4.3.3 Synthesis of Alloy Fe-Pt NW

Fe-Pt NWs was prepared by pulsed template electrodepositing in an electrolytic bath containing both Pt (IV) and Fe (II) ions. The electrolyte was composed of the following: 12% w/v $FeSO_4(7H_2O)$, 7.5% w/v Na_2SO_4, 2.5% w/v H_3BO_3, 1% w/v $C_6H_8O_6$, 1% w/v H_2PtCl_6 and

7% $HClO_4$. The NW were synthesized using pulsed electrodeposition alternating between -1.1V and -0.35V.



Figure 4.2: Schematic of the longitudinal cross-section of the prototype Fe-Pt NWs depicting the layout of the core shell structure

4.3.4 Release of the Synthesised Fe/Pt Composite NW Platforms from AAO Template

The NWs were released from the AAO template using the method previously described. Briefly, the Au contact layer was removed using 32% HCl, minimising contact time. The AAO templates were then dissolved using 1M NaOH for 1.5 hrs and sonicated to ensure the complete release the synthesised NWs. The released NWs were then collected using centrifugation, washed three times with ethanol before finally storing in ethanol as well to prevent further oxidation of Fe.

4.3.5 Quantification of Synthesised Fe/Pt Composite NW Platforms Using ICP-OES

ICP-OES (Shimadzu ICPE-9820) was used to quantify the concentration of the prepared stock solutions of Fe coated Pt NWs and Fe-Pt NWs used during *in vitro* studies. The same protocol described in Chapter 3; Section 3.7.4.1 was used. In brief, 100ul of NW suspension was aliquoted together with 300 µl of Aqua Regia into a volumetric flask and left at room temperature for 60 minutes to ensure complete dissolution. The solution was then diluted to 20 ml and ran using the ICP-OES.

4.3.6 Morphological Characterisation of Synthesised Fe/Pt Composite NW Platforms Using TEM and HRTEM

Pt NWs and Fe coated Pt NWs were prepared for TEM analyse as described previously in Chapter 3, Section 3.7.4.2. In summary, the sample was diluted with ethanol from the stock solution the magnetic NWs and then ultrasonicating it for 30 s using sonic vibra cell, (MO, USA). A drop of this suspension was adsorbed onto a carbon coated copper grid with a filter

paper being used to absorb excess sample. The copper grid was then be left overnight to air dry. The samples were then analysed using a TEM (FEI Tecnai T12 TEM) at MMU and HRTEM (JEM-2100). EDX analyses was also performed on the FEI Tecnai T12 TEM to determine elemental composition.

4.3.7 Determination of the Crystalline Properties of the Synthesised Fe/Pt Composite NW Platforms Using Powder XRD

The crystalline phases of Fe coated Pt NWs and Fe-Pt NWs was analysed within the AAO template by studying the powder X-ray diffraction patterns taken from a MiniFlex 600 benchtop X-ray diffractometer (Rigaku, Tokyo, Japan) with Cu Kα radiation (λ = 1.54060 Å). The X-ray tube was set-up at a voltage of 40kV and a current of 15mA. The region $30° \leq 2\theta \leq 90°$ was evaluated.

4.3.8 Determination of the Outer Surface Composition of the Synthesised Fe/Pt Composite NW Platforms Using Raman Spectroscopy

Raman spectroscopy was used to determine the composition of the outer oxide amorphous layer. The obtained peaks were referenced against known Fe oxide peaks from the literature. The Fe coated Pt NWs and Fe-Pt NWs was pipetted onto a clean glass microscope slide and allowed to air dry. Thereafter it was analysed using a *Horiba LabRAM HR* Raman spectrometer with an *Olympus BX41* microscope attachment using a 0.4mW power laser. A 514.5 nm wavelength used from a Lexel Model 95-SHG argon ion laser.

4.3.9 Study of the Effects of Fe Modulation on the Magnetic Properties of the Fe/Pt Composite NW Platforms Using VSM

A vibrating sample magnetometer (VSM) (Quantum Design DynaCool, 12 T Physical Property Measurement System (PPMS)) was employed to study the magnetic properties of the Fe/Pt composite NWs. The readings will be taken with the applied field parallel and transverse to the wire axis of the NWs embedded in the AAO template as previously done. The magnetic moments measurements were taken at room temperature, 300 K and the magnetic field was swept across a range of ± 10000 Oe.

4.3.10 Cytotoxicity and Cellular Internalisation Analysis of the Fe/Pt Composite NW Platforms

Cell viability was measured using XTT assay as discussed previously. Briefly, The Cell lines were cultured, seeded, and treated as in 96-well plates at the following densities: 3T3-5000 Cells/Well and Tera-1-6000 Cells/Well. After treatment with five concentrations of Fe coated Pt NWs or Fe-Pt NWs, the cells were incubated at 37°C and 5% CO_2 for 24 hrs and 48 hrs for XTT analyses. For cellular internalisation, the cells were incubated for 48 hrs. Thereafter, the cells were washed with PBS thrice to remove the free floating non-internalised NWs. The cells were then imaged using phase contrast system (Olympus CKX53) to investigate the interactions of the NWs on the cells.

4.4 Results and Discussion

4.4.1 Synthesis, Morphological Analysis, and Stability of Fe Coated Pt NWs

The novel synthesis method adopted to synthesise Fe coated Pt NWs consisted of three stages. In stage one, Pt NW arrays embedded in the nanopores of the AAO template was synthesised. This was achieved employing method described for synthesising Pt NWs in Chapter 3, Section 3.7.2.2. **Figure 4.3** is the Current vs Time graph monitoring the growth of Fe coated Pt NWs in stage one. The graph indicates no overgrowth has occurred.

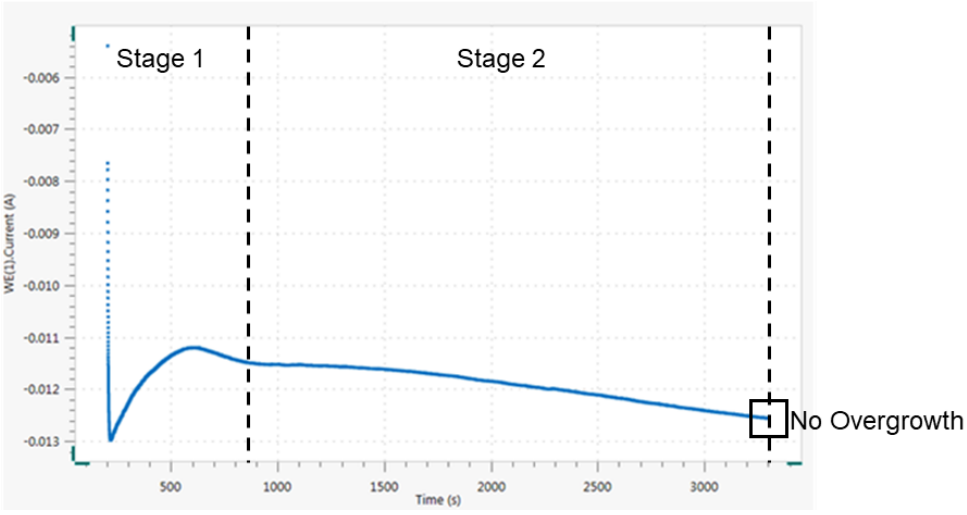


Figure 4.3: Image of Current vs Time graph monitoring the growth of Pt in the nanopores of the AAO template.

Stage two of the synthesis of Fe coated Pt NWs entailed the partial dissolution of the AAO template resulting in the widening of the nanopores within the AAO template. The structural integrity of the AAO template and Au contact layer was maintained in this stage. **Figure 4.4** clearly depicts the successful controlled dissolution of the AAO template. The surface image of the AAO template portraying the nanopore diameter after deposition of Pt and after exposure to the phosphoric acid resulting in pore widening.

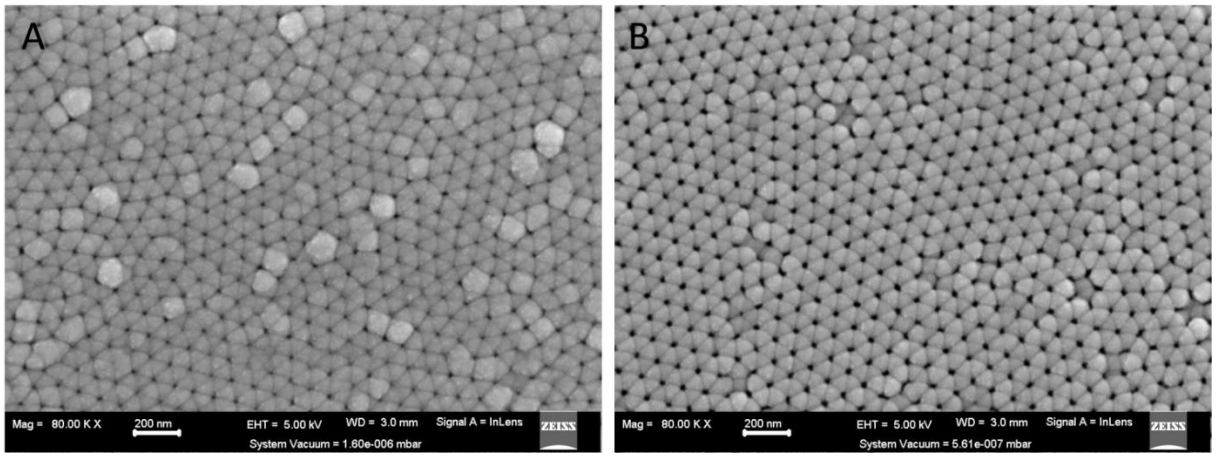


Figure 4.4: SEM image showing surface view of AAO template **A)** after Pt deposition, **B)** after controlled AAO dissolution for nanopore widening. Scale bar: **A)** 200nm, **B)** 200nm.

In stage three of Fe coated Pt NWs synthesis. The area exposed by the partial dissolution of the AAO template was filled with Fe. A pulsed electrodeposition technique was employed to achieve this. The voltage was pulsed at -1.1 V for 15 s and spaced between 30 s at 0 V (**Figure 4.5**). Pulsed electrodeposition was chosen to allow for the recovery of the Fe^{2+} ions within the nanopores. The NWs were then further processed by releasing the NWs using 1 M NaOH to completely dissolve the AAO template. A stock solution of Fe coated Pt NWs was prepared by washing the released NWs thrice and storing them in 99% ethanol.

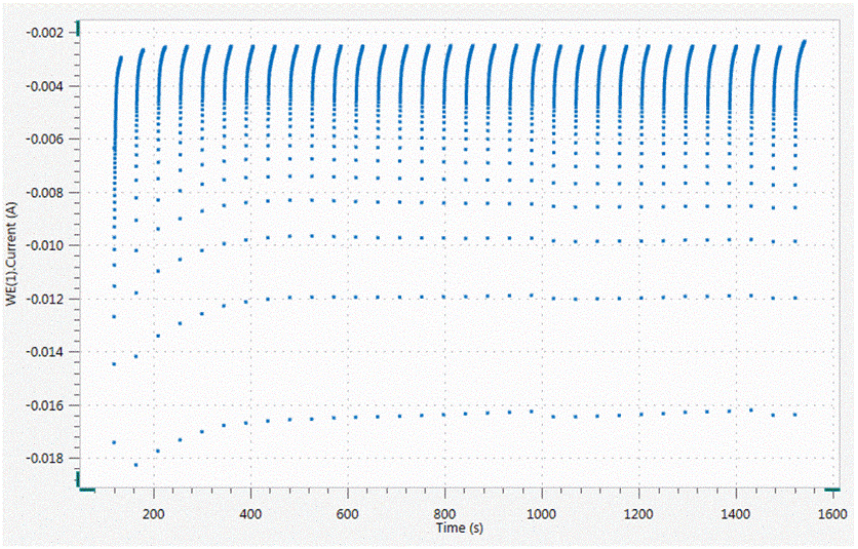


Figure 4.5: Image of Current vs Time graph monitoring the growth of Fe coating the Pt NWs in the widened nanopores of the AAO template.

TEM and HRTEM images of Fe coated Pt NWs was analysed using ImageJ software to assess its dimensions (**Figure 4.6**). An average length of 2.2 µm (SD= 1.0/ Min=0.303 µm /Max= 5.827 µm) and average diameter of 54±4.0nm (SD= 4.0 / Min=41.929 nm /Max= 69.121 nm) was found. The diameter of Fe coated Pt NWs was significantly larger compared to Pt NWs (39±2.0). This was due to the pore widening step after the initial Pt deposition in the AAO template which created the space necessary to deposit the Fe in a controlled manner.

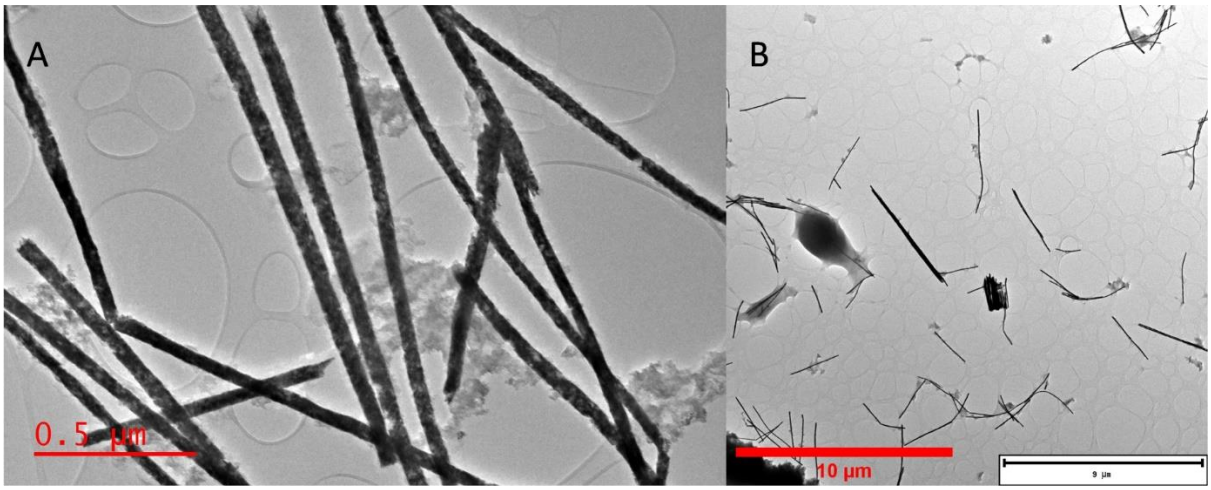


Figure 4.6: Image of **A)** HRTEM, **B)** TEM; low magnification images of Fe coated Pt NWs showing its morphology and length distribution. Scale Bar: **A)** 0.5 µm, **B)** 10 µm (red scale bar)

Figure 4.6 (A) depicts the low magnification HRTEM image of Fe coated Pt NWs. It clearly depicts the successful synthesis of NW with large aspect ratios, variable lengths, and nominal diameters. The average length of 2.2 µm was ideal for the intended biomedical application. Some unwashed contaminants from the AAO template are seen as well (**Figure 4.6 (B)**).

The variation in length was accounted for by the inconsistent breakage of the NWs when sonicating. The observed morphology along the diameters of the Fe coated Pt NWs shows a non-uniform surface. This discrepancy in the diameters was likely due to minor imperfections in the AAO template caused by the controlled dissolution when widening the nanopores.

The High magnification HRTEM and TEM images of Fe coated Pt NWs correspond to **Figure 4.7 (A)** and **Figure 4.7 (B)** respectively. The surface of the NW showed an undulating form which was advantages for coating adherence and increasing drug loading capacity due to the increased attachment points and surface area respectively. The image depicts a clear polycrystalline nature with no clear grain boundaries due to the high electron density. The boundary between the Pt and Fe was not visible likely due to Pt sharing its electron density with the Fe. Fe coated Pt NWs consisted of an outer amorphous shell caused by the oxidation of Fe. The outer shell of Fe coated Pt NWs was not smooth and continuous as Fe NWs described in chapter three. The amorphous layer was very rough and resembled amorphous spots on the NW surface.

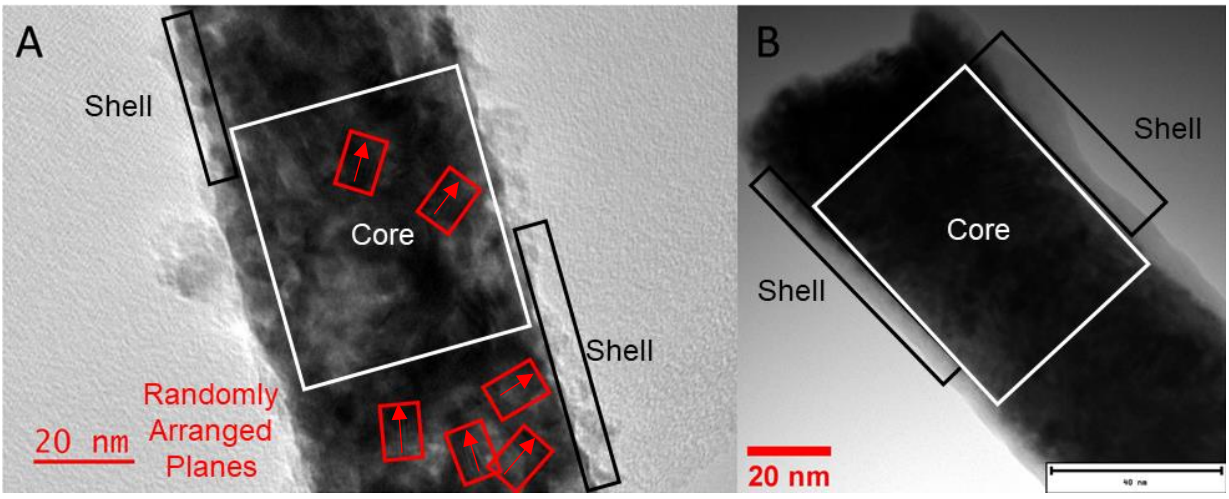


Figure 4.7: Image of **A)** HRTEM, **B)** TEM; high magnification images of Fe coated Pt NWs showing its morphology, outer oxide layer, core shell and polycrystalline structure. Scale bar: **A)** 20 nm **B)** 20 nm (red bar)

As the Pt and Fe components were not distinct from each other, EDX analysis was performed to confirm the coating of the Pt NWs with Fe. The EDX spectrum was acquired from a single NW that was isolated on the grid and not a clumped together with other NWs (**Figure 4.8 (A)**). The EDX spectrum detected Fe, Pt, O, C, and Cu (**Figure 4.8 (B)**). The C and copper can be accounted for as it come from the grid that Fe coated Pt NWs was dispersed on for EDX analyses. The O would likely be present on the observed outer amorphous layer while the Pt and Fe would form part of the NW structure.

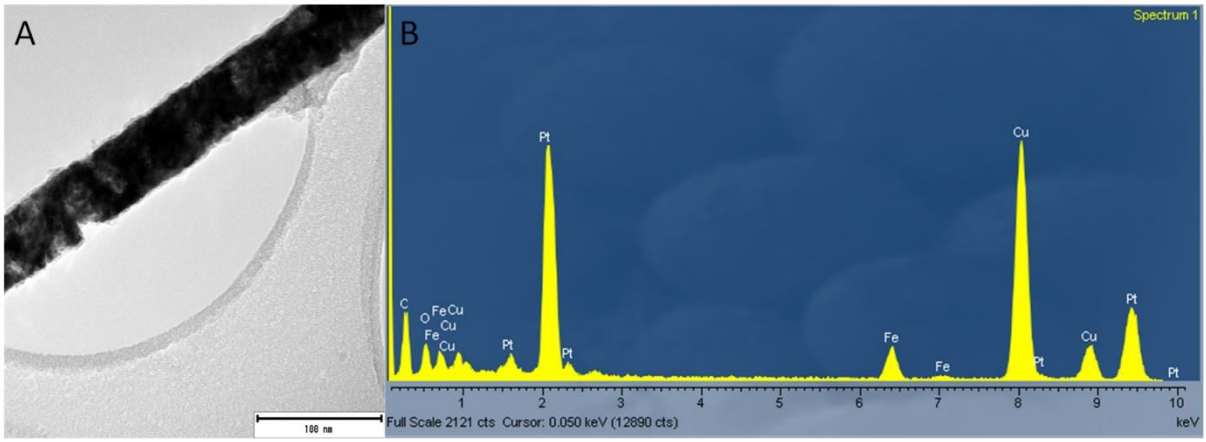


Figure 4.8: A) TEM image where EDX spectrum was taken for Fe coated Pt NWs, **B)** EDX spectrum of Fe coated Pt NWs showing the presence of Pt, Fe, and O from Fe coated Pt NWs and C and Cu from the grid used in sample preparation.

The zeta potential of Fe coated Pt NWs was measured to assess its physical stability. The NWs need to stay uniformly dispersed for a sufficient period to ensure correct and uniform dosing during future treatments. The zeta potential of Fe coated Pt NWs was -34.6±1.1 mV which was considered as physically stable (205). Fe coated Pt NWs however, sedimented after a few hours. This was likely due to the competing electrostatic, gravitational, and magnetic forces. This effect was reversible through light agitation of the NW suspension.

4.4.2 Synthesis, Morphological Analysis, and Stability of Fe-Pt NWs

An Fe-Pt alloy NW was synthesised by combining the electrolytic baths of Fe NWs and Pt NWs and pulsing the deposition voltage between -1.1 V and -0.35 V. The previously established electrochemical cell set up as described in Chapter 3, Section 3.4 was used to deposit Fe-Pt NWs as it fabricated reproducible uniform NW growth. **Figure 4.9** is the Current vs Time graph monitoring the growth of Fe-Pt NWs. The pulse stages in synthesis of Fe-Pt

NWs are shown, and the graph depicts no overgrowth occurred during synthesis. Fe-Pt NWs was then released from the AAO template by submerging the template in 1 M NaOH and sonicating it to ensure complete release of nanowires.

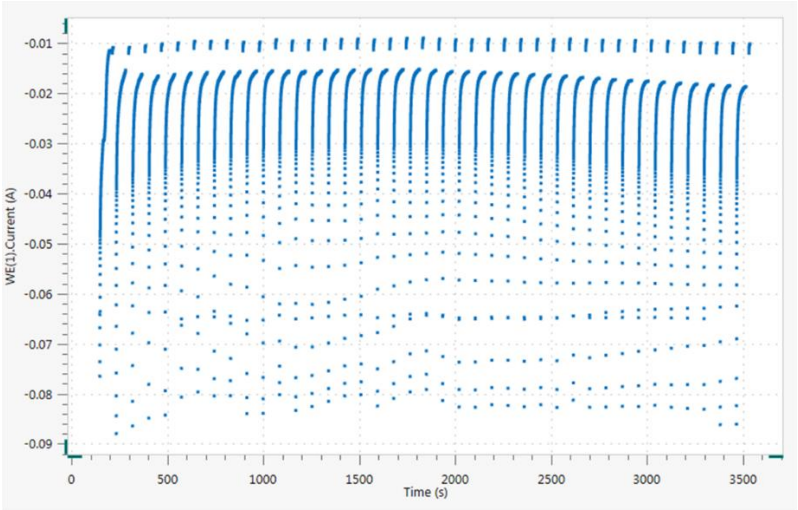


Figure 4.9: Current vs Time graph monitoring the growth of Fe-Pt NWs in the nanopores of the AAO template.

TEM images of Fe-Pt NWs (**Figure 4.10 (B)**) was then analysed to determine the average length and diameter of Fe-Pt NWs. Fe-Pt NWs displayed the largest average length of 3.1 µm (SD= 1.8 / Min= 0.557 µm /Max= 8.446 µm) compared to Fe NWs, Pt NWs, and Fe coated Pt NWs. The average length was within the desired range making it suitable for the intended biomedical purpose. The average diameter of Fe-Pt NWs was 41±3.0 nm (SD= 2.6 / Min=35.4 nm /Max= 48.3 nm).

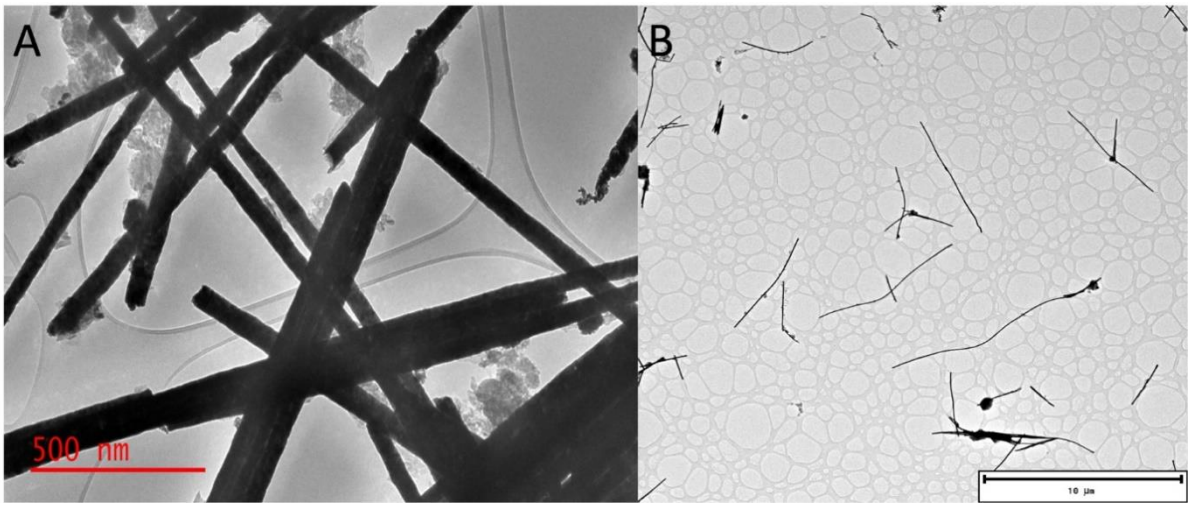


Figure 4.10: A) HRTEM, **B)** TEM; low magnification images of Fe coated Pt NWs showing its morphology and length distribution. Scale bar: **A)** 500 nm, **B)** 10 µm.

The low magnification HRTEM image (**Figure 4.10 (A)**) shows the successful synthesis of Fe-Pt NWs as a high aspect ratio NW with nominal diameters. Fe-Pt NWs had the highest electron density compared to Fe NWs, Pt NWs, and Fe coated Pt NWs. Some contaminate residues can be seen, however, these will most likely be removed in the six washing steps prior to cell treatment. The NWs displayed a smooth surface and a variation of NW length due to the NW release process. Fe-Pt NWs showed one NW that had a change in diameter. However, most of the NWs maintain their nominal diameter along their length.

The high magnification images of Fe-Pt NWs (**Figure 4.11**) depicted a core shell structure. Fe-Pt NWs displayed a polycrystalline structure with a thin amorphas layer coating the NW. The crystallite planes were randomly arranged and the interplanar spacing was nonconstant. The average thickness of the outer oxide layer was 2.3±0.4 nm which was thinner than that of Fe NWs (3.9±0.5nm).

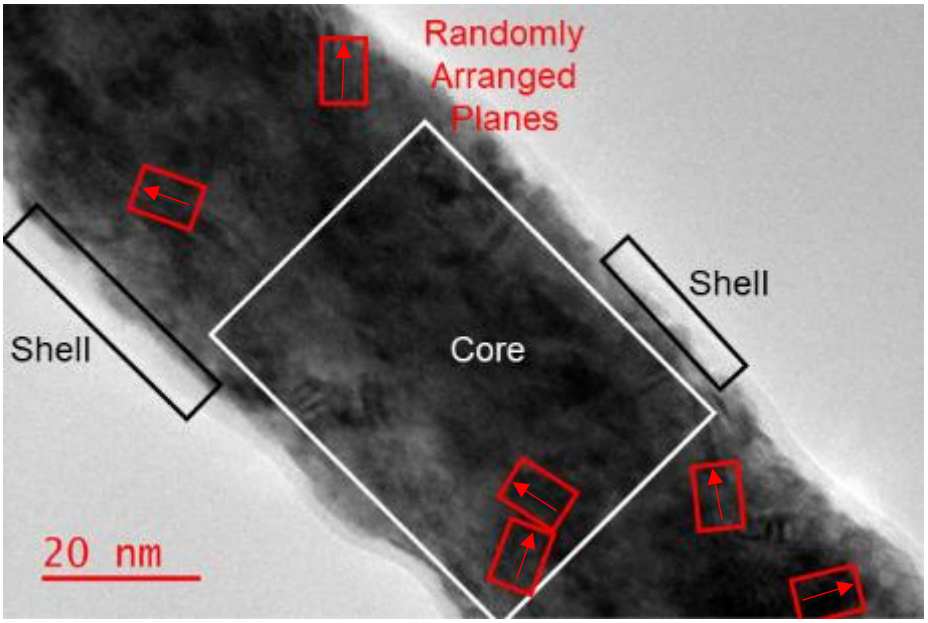


Figure 4.11: High magnification HRTEM image of Fe-Pt NWs showing its morphology, outer oxide layer, core shell and polycrystalline structure.

The physical stability of Fe-Pt NWs was then assessed by measuring its zeta potential. A uniformly dispersed suspension was vital to safe and consistent biomedical applications. The zetapotential was measured at -24.6±1.7 mV. Given the smaller magnetic moments and larger zetapotential, Fe-Pt NWs displayed greater stability compared to Fe NWs.

4.4.3 Analysis of the Crystalline Structure, Crystallite Size, and Interplanar Spacing of Fe/Pt Composite NWs Using Powder XRD

The crystallite structure of Fe coated Pt NWs and Fe-Pt NWs was analysed by studying the powder XRD patterns of the Fe/Pt Composite NW platforms. The crystal structure was confirmed, and the crystallite size and d-value were estimated using the obtained data. **Figure 4.12 (A)** and **Figure 4.12 (B)** shows the XRD diffractograms obtained from the Fe Coated Pt NWs and Fe-Pt NWs respectively, and **Table 4.1** summarises the calculated crystallite size (Scherrer equation) and d-value (Bragg's law).

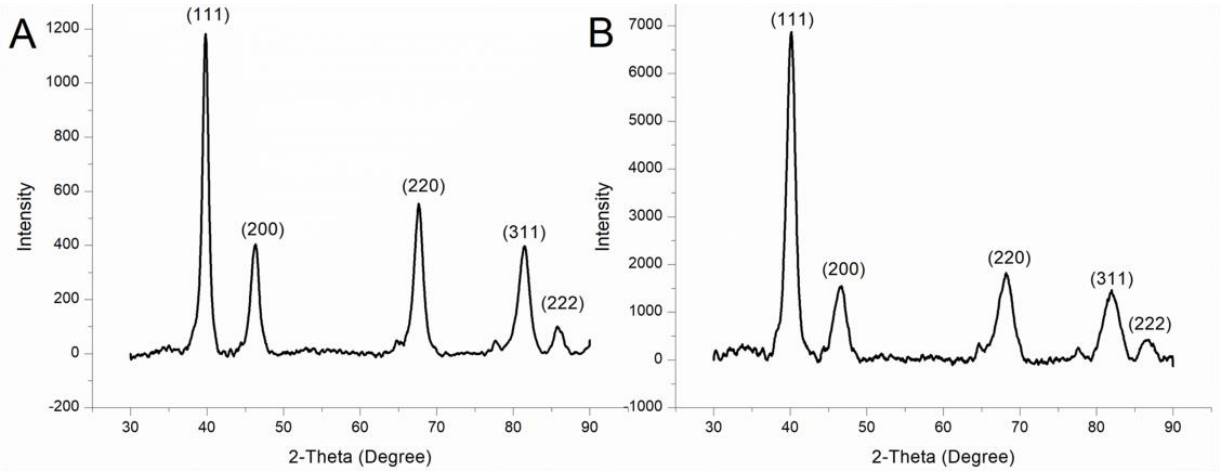


Figure 4.12: Image showing powder XRD diffractogram obtained for **A)** Fe coated Pt NWs and **B)** Fe-Pt NWs.

Fe coated Pt NWs which contained both Fe and Pt showed only five peaks which correspond to a cubic crystal system for Pt as was observed for Pt NWs in chapter three. This can be accounted for due to Pt being the majority constituent of Fe coated Pt NWs and that the first step in the synthesis of Fe coated Pt NWs was identical to Pt NWs causing the same crystal structure to occur. The observed peaks for Fe coated Pt NWs were at 2 θ values of 39.80°, 46.26°, 67.66°, 81.39° and 85.9° corresponding to hkl values of (111), (200), (220), (311), and (222).

Fe-Pt NWs was deposited in an electrolyte bath containing Pt (IV) and Fe (II) leading to an alloy formation indexed to Iron Platinum ((Fe3Pt17)0.2). The key peaks observed in the data for Fe-Pt NWs were at 2 θ values of 40.09°, 46.50°, 68.10°, 81.95°, and 86.67° corresponding to (111), (200), (220), (311), and (222) planes of a cubic crystal system. Fe coated Pt NWs and Fe-Pt NWs had minor peaks at ≈77° due to the presence of Au coated onto the back of the AAO template.

The estimated crystallite sizes were smaller than the diameter of Pt NWs (39 nm), Fe coated Pt NWs (50 nm), and Fe-Pt NWs (41 nm) indicating that these NWs are polycrystalline as well as confirmed by the HRTEM. Since individual crystallites have a minimum of one magnetic domain Fe coated Pt NWs, and Fe-Pt NWs can be considered to have a complex multi-domain state.

Table 4.1: Summary of obtained XRD data and interpretation using Scherrer equation for crystallite size and Braggs law for d-value.

NW Platform	Composition	2 θ	β (FWHM)	Crystallite Size (nm)	d (Å)	h k l
Fe coated Pt NWs	Pt	39.8	1.06482	7.02	2.26	111
	Pt	46.3	1.38333	5.28	1.96	200
	Pt	67.7	1.2606	5.23	1.38	220
	Pt	81.4	1.83388	3.28	1.18	311
	Pt	85.9	1.47306	3.95	1.13	222
Fe-Pt NWs	$(Fe_3 Pt_{17})0.2$	40.1	1.46095	5.11	2.25	111
	$(Fe_3 Pt_{17})0.2$	46.5	2.03405	3.59	1.95	200
	$(Fe_3 Pt_{17})0.2$	68.1	2.42422	2.72	1.38	220
	$(Fe_3 Pt_{17})0.2$	81.9	2.47224	2.43	1.17	311
	$(Fe_3 Pt_{17})0.2$	86.7	1.79009	3.23	1.12	222

4.4.4 Analysis of the Outer Surface Composition of the Fe/Pt Composite NWs Using Raman Spectroscopy

An outer oxide layer was observed on both Fe coated Pt NWs and Fe-Pt NWs as observed by the HRTEM. This oxide layer was developed during the release process of the NWs from the AAO template. This layer was naturally formed when the Fe from Fe coated Pt NWs and Fe-Pt NWs was in the basic NaOH solution or exposed to air. The oxide coating formed impacts the magnetic properties and the attachment potential for coatings and small molecules used in engineered smart delivery. The composition of the oxide layer was then determined using Raman Spectroscopy by referencing the obtained peaks with the known peaks of Fe oxides found in the literature.

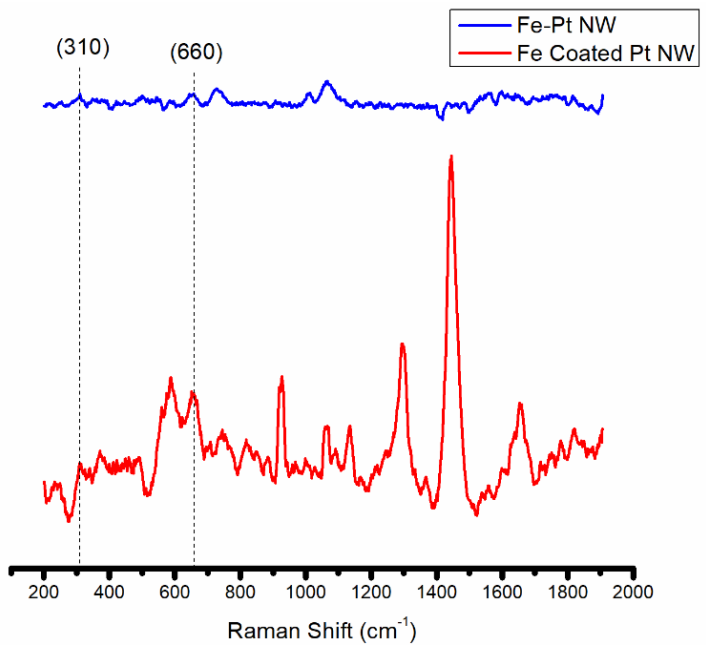


Figure 4.13: Raman spectrum obtained for Fe coated Pt NWs and Fe-Pt NWs.

Fe coated Pt NWs was very Fluorescent which made it difficult to obtain a clear Raman spectrum (**Figure 4.13**). This was due to the florescence masking the low Raman scattered photons which leads to a low signal to noise ratio. However, peaks at 309 cm^{-1} (E_g) and 658 cm^{-1} (A_{1g}) were observed. Combined with the presence of O on the EDX analyses (**Figure 4.8**) of Fe coated Pt NWs; this indicates that the imaged outer amorphous layer was proposedly magnetite as was in Fe NWs.

Fe-Pt NWs presented very low intensity peaks at 310 cm^{-1} (E_g) and 658 cm^{-1} (A_{1g}) suggesting the outer oxide layer comprising of magnetite as well (**Figure 4.13**). The low intensity of the peak could have been brought about by the oxide layer thickness (2.3 nm) which was below the detection limit of the *Horiba LabRAM HR* Raman spectrometer with an *Olympus BX41* microscope attachment.

4.4.5 Study of Magnetic Properties and Determination of MTD Suitability of Fe Coated Pt NWs and Fe-Pt NWs Using VSM

The goal of this study was to engineer a NW platform capable of MTD. This necessitates that the synthesised NW platform be attracted towards a magnetic field with a sufficient Ms at low magnetic fields. The nanowire platform therefore needs to display either ferromagnetic or

superparamagnetic behaviour. This would allow the NW platform to be entrapped and removed from the capillary system and transferred to the target area as desired.

Fe coated Pt NWs was analysed for its response to a magnetic field. **Figure 4.14** shows the normalised M-H loops focused on the hysteresis loops of Fe coated Pt NWs parallel and transverse to the applied magnetic field. **Figure 4.14** is zoomed in to 5000 Oe to facilitate the viewing of the magnetic behaviour at a higher resolution. In the parallel orientation, the long field scan ± 10000 Oe showed a combination of competing interactions, that being diamagnetism and ferromagnetism. Ferromagnetism was responsible for the hysteresis loop while the diamagnetism was attributed to the Au coated AAO template. The diamagnetism causes a decrease in the induced magnetisation with increasing applied magnetic field and vice versa. Clear soft magnetic behaviour was evident in the hysteresis loop for the parallel orientation for field sweeps in the range ±4000 Oe. A square ratio of M_R/M_S = 0.62 was observed. For the transverse orientation a hysteresis loop was also found with a square ratio of M_R/M_S = 0.2. The magnetic easy axis of Fe coated Pt NWs was therefore in the parallel axis as was in Fe NWs. The following values have been deduced for Fe coated Pt NWs using the combined mass of Fe and Pt in the unit conversions, M_S= 7.62 X 10^2 A/m, M_R 4.21 X 10^2 A/m, and Hc = 476 Oe. Both Fe and Pt were assumed to contribute to the dipole moment. The magnetisation of Fe coated Pt NWs was fully saturated at a low field of 1800 Oe in the magnetic easy axis. The low M_s was due to the low proportion of Fe compared to Pt in Fe coated Pt NWs (206). The proportion of Pt to Fe for Fe coated Pt NWs as determined using ICP-OES was 132:1. The ratio of Fe to Pt, hence M_s can be easily increased by increasing the nanopore size of the AAO template by increasing the contact time with the phosphoric acid in the pore widening step during Fe coated Pt NWs synthesis. And thereafter increasing the total deposition time for Fe in the third step of Fe coated Pt NWs synthesis.

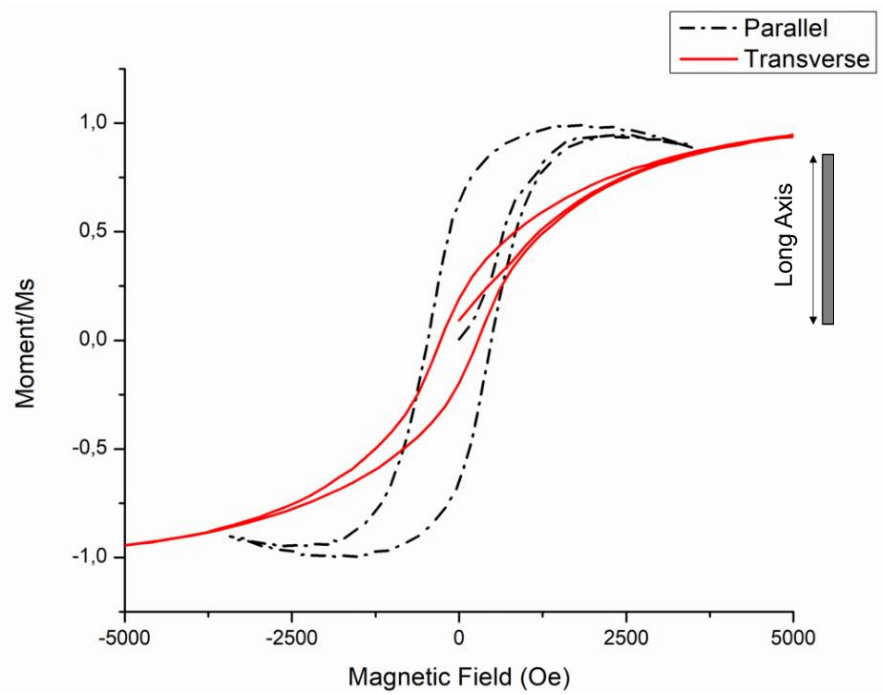


Figure 4.14: M-H loop of Fe coated Pt NWs within the AAO template in the parallel and transverse orientation.

Figure 4.15 shows the M-H loops of Fe-Pt NWs. The transverse orientation shows paramagnetic behaviour. Paramagnetic materials are slightly attracted to a magnetic field. The parallel orientation shows a very interesting response as the M-H loop resembles that of two competing ferromagnetic grains or nanowires of varying dimensions. The M-H loop for the parallel orientation has the same profile as a superconductor reported by Gokhfeld et al (207). Superconductors are repelled from magnetic fields making. The combination of the competing interactions makes Fe-Pt NWs not suitable for MTD due to fidelity in the signal to noise ratio and response.

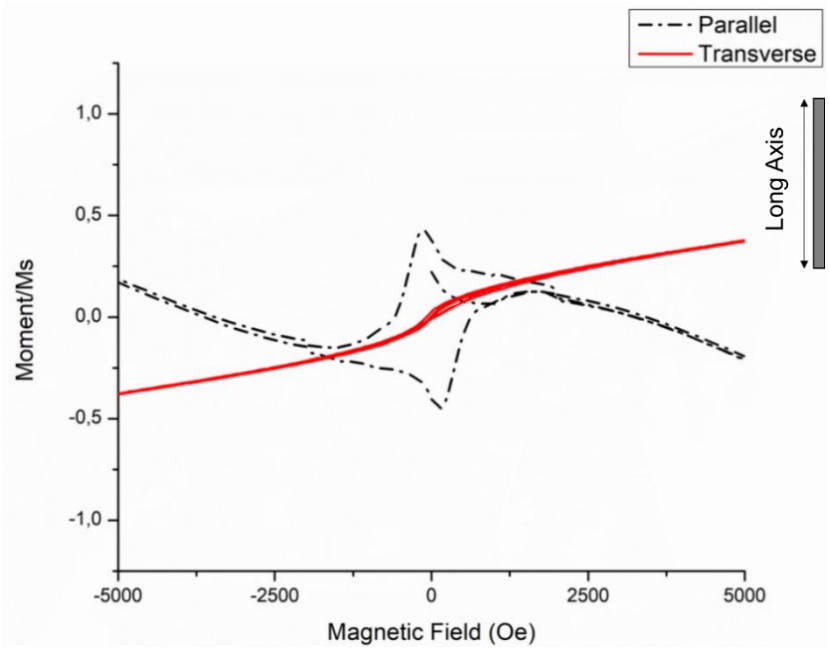


Figure 4.15: M-H loop of Fe coated Pt NWs within the AAO template in the parallel and transverse orientation.

The modulation of Pt NWs with Fe was successful in changing the magnetic properties. Fe coated Pt NWs displayed ferromagnetic behaviour in the parallel and transverse orientation and thus behaved as a soft magnetic material for a polycrystalline ferromagnetic material. The magnetic properties of Pt NWs were thus successfully changed to ferromagnetic behaviour with the coating of the Pt with Fe.

4.4.6 Cytotoxicity Evaluation and Cellular Internalisation of the Fe/Pt Composite NW Platforms

The biocompatibility of Fe coated Pt NWs and Fe-Pt NWs was assessed by the colorimetric XTT assay which was used to measure the %viability of cells. This was achieved by the tetrazolium salt in the XTT assay being bio-reduced only in the presence of metabolically active cells to the formazan dye. Allowing for the precise measurement of viable cells. The change in cell viability between treated and untreated cells was used to determine the toxicity of the NW platforms.

4.4.6.1 Cell Viability After Fe Coated Pt NWs and Fe-Pt NWs Treatment on Mouse Fibroblasts (3T3) to Determine Biocompatibility

The %viability was measured 24 hrs and 48 hrs after treatment on a non-cancerous mouse fibroblast. The concentrations for treatment used for Fe coated Pt NWs, and Fe-Pt NWs were 320, 160, 80, 40, and 20 µg /mL. This corresponds to a concentration for Fe coated Pt NWs of ~6400, ~3200, ~1600, ~800 and ~400 NWs/Cell while Fe-Pt NWs corresponded to ~7200, ~3600, ~1800, ~900, and ~450 NWs/Cell. These concentrations are much greater compared to the targeted concentrations in potential biomedicine applications. High concentrations of Fe coated Pt NWs and Fe-Pt NWs were chosen to investigate the effects of Fe alloy and Fe coating on the NW platforms short-term acute toxicity

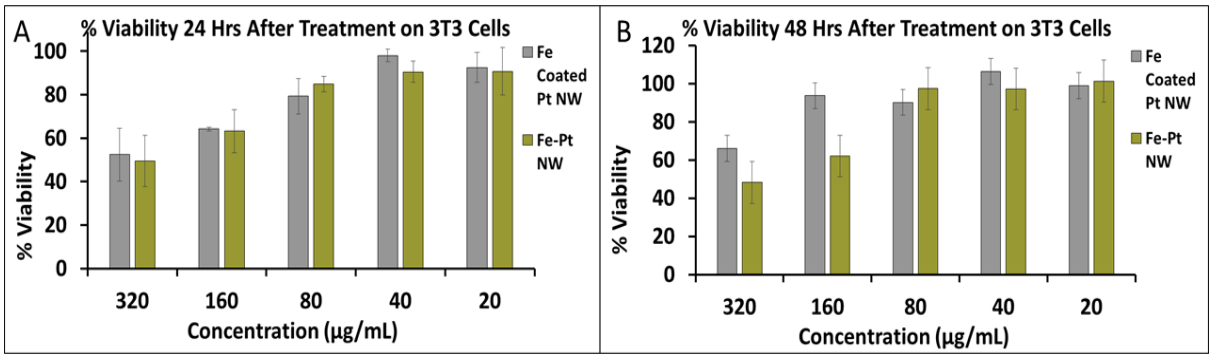


Figure 4.16: % cell viability of 3T3 cells treated with Fe coated Pt NWs and Fe-Pt NWs after **A)** 24 hrs, **B)** 48 hrs.

Coating Pt nanowires with Fe had a slight influenced the cell viability of treated cells as shown by the results for Fe coated Pt NWs (**Figure 4.16**). At 24 hrs after treatment with Fe coated Pt NWs, the cell viability significantly decreased at concentrations 160 and 320 µg/mL. After 48 hrs, the cells treated with 160 µg/mL of Fe coated Pt NWs rebounded to ≥90%. At concentration 320 µg/mL however, the cell viability stayed below 70% although there was an increase in %viability compared to 24 hrs. Fe coated Pt NWs was also shown to be internalised by the cells.

NWs composed of an Fe-Pt alloy showed the greatest cytotoxic activity as shown by the results for Fe-Pt NWs even though the phase contrast images suggest that they internalised the least number of NWs. At both time intervals, Fe-Pt NWs displayed greater toxicity at the higher concentrations of 160 and 320 µg/mL. At concentrations 80, 40, and 20 µg/mL, for both

24 hrs and 48 hrs incubation after treatment with Fe-Pt NWs, there was a negligible decrease in cell viability indicating that at these concentrations, Fe-Pt NWs was biocompatible.

4.4.6.2 Determination of the Suitability of Fe Coated Pt NWs and Fe-Pt NWs as a Therapeutic Agent for TC by Evaluating Cell Viability Employing Tera-1 Cells

The cytotoxic activity Fe/Pt composite NW was assessed against testicular cancer. Fe coated Pt NWs and Fe-Pt NWs treated Tera-1 cells were incubated with varying concentrations for 24 hrs and 48 hrs. The concentrations chosen for treatment was 320, 160, 80, 40, and 20 µg /mL. The same concentrations as used for 3T3 was chosen to have comparative results to the cytotoxic activity for the different cell lines. These concentrations expressed as NWs/Cell for Fe coated Pt NWs: ~5600, ~2800, ~1400, ~700, ~350 NWs/Cell; and Fe-Pt NWs: ~6400, ~3200, ~1600, ~800 and ~400 NWs/Cell.

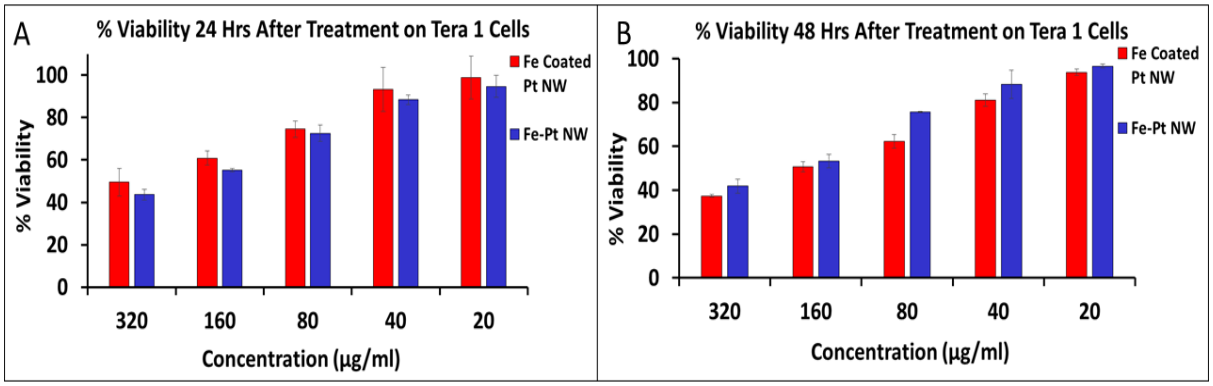


Figure 4.17: % cell viability of Tera-1 cells treated with Fe coated Pt NWs and Fe-Pt NWs after **A)** 24 hrs, **B)** 48 hrs.

Both Fe coated Pt NWs and Fe-Pt NWs demonstrated cellular internalised by the Tera-1 cells (**Figure 4.18**) and displayed inherent toxicity against the Tera-1 cell in a dose dependent manner. Fe coated Pt NWs had the best performing cytotoxic activity and had the lowest IC_{50}, of 165 µg/mL at 48 hrs, when compared to the Pt NWs and Fe coated Pt NWs. The toxicity of Fe coated Pt NWs showed a dose and time dependent trend with the cell viability decreasing for increasing concentrations and incubation time (**Figure 4.17**).

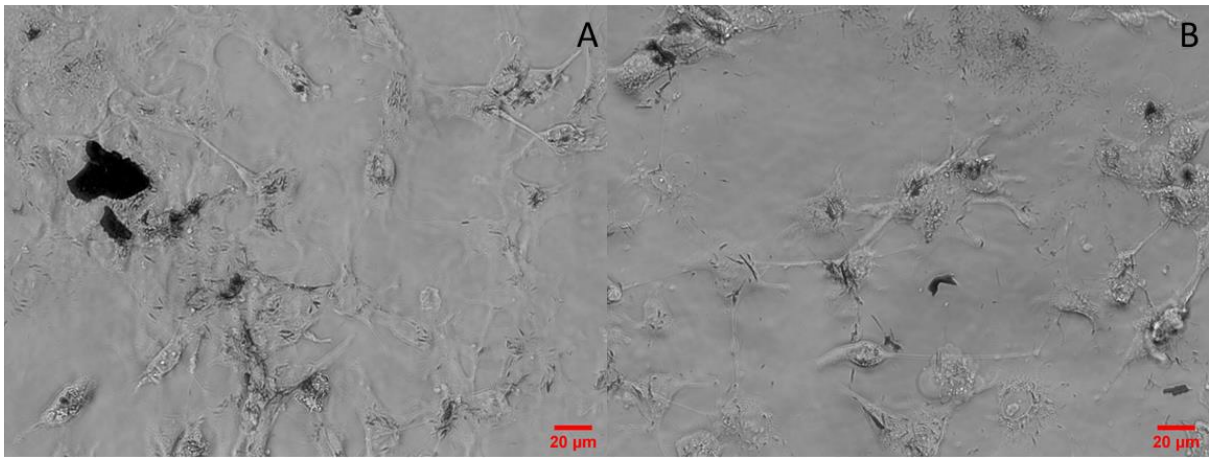


Figure 4.18: Phase contrast images of Tera-1 cells after **A)** 48 hrs treatment with Fe NWs, **B)** 48 hrs treatment with Pt NWs. Scale bar: **A)** 20 µm, **B)** 20 µm

Fe-Pt NWs presented an IC_{50} of 207 µg/mL at 48 hrs which was superior to Pt NWs but was inferior when compared to Fe coated Pt NWs. The cell viability did not appear to be influenced by a longer exposure but showed dose dependent toxicity. As previously mentioned, it should be noted that the concentrations tested for both biocompatibility and cytotoxicity are much larger than what was the projected concentrations in the bloodstream and healthy tissue. However, due to the nature of MTD, it was anticipated that these concentrations will be reached at the target site.

4.5 Concluding Remarks

A novel synthesis method for coating Pt NW with Fe was explored and successfully synthesised to form Fe coated Pt NWs. Fe coated Pt NWs displayed desirable ferromagnetic properties with a significant Ms. Fe coated Pt NWs was deemed biocompatible when tested against mouse fibroblasts. Fe coated Pt NWs displayed the most significant cytotoxic activity against Tera-1 cells with an IC_{50}, of 165 µg/mL at 48 hrs which was around twice the potency of Pt NWs. Fe-Pt NWs composed of a polycrystalline Fe-Pt alloy NW that was majority Pt. M-H hysteresis loop resembled that of a superconductor which was not ideal for MTD. Fe-Pt NWs displayed an IC_{50} of 207 µg/mL at 48 hrs against Tera-1 cells which was superior then Pt NWs as well.

CHAPTER 5.
CONCLUSIONS, RECOMMENDATIONS, AND FUTURE PROSPECTS

5.1 Conclusions

The application of Magnetic NWs in cancer therapeutics has great potential for improving cancer therapeutics. Four NW platforms were developed during this research each with their unique properties. Fe coated Pt NWs has proven to be a promising option in improving TC therapeutics as shown by the cytotoxicity and VSM analyses. Template electrodeposition was successfully utilised in the synthesis of NW platforms. A single Fe crystal structured NW core with an outer magnetite shell was synthesised creating Fe NWs. Fe NWs demonstrated clear ferromagnetic behaviour with large M_S and H_C. The single crystal Fe comprised Fe NWs revealed significant cytotoxic activity against mouse fibroblast. This contrasts the behaviour of the polycrystalline counterpart which is biocompatible at high concentrations as shown in literature.

A polycrystalline structured Pt NW (Pt NWs) was the second platform synthesised using template electrodeposition. Pt NWs showed inherent bioactivity against Tera-1 cells at high concentrations with a calculated IC_{50} of 354 µg/mL at 48 hrs. Pt NWs however, displayed unfavourable magnetic characteristics. When the applied field was parallel to the long axis of Pt NWs, diamagnetic behaviour was observed. Interestingly, when the magnetic field was applied transverse to the long axis of the NW, Pt NWs displayed superparamagnetic behaviour with large moments. Due to the competing behaviours, Pt NWs was deemed not suitable for MTD.

The next platform synthesised employed a novel synthetic method developed in this research. Pt NWs were coated with Fe creating Fe coated Pt NWs. Fe coated Pt NWs was deemed suitable for MTD application due to the desirable ferromagnetic properties and significant Ms. When tested against mouse fibroblasts Fe coated Pt NWs was deemed biocompatible. Fe coated Pt NWs presented the most considerable cytotoxic activity against Tera-1 cells with an IC_{50} of 165 µg/mL at 48 hrs which was around twice the potency of Pt NWs. Fe coated Pt NWs can therefore be regarded as a selective, targeted multifunctional potential therapeutic option for TC.

The fourth platform synthesised (Fe-Pt NWs) composed of a polycrystalline Fe-Pt alloy NW with a majority Pt composition. The M vs H hysteresis loop of Fe-Pt NWs did not resemble any basic magnetic properties. It however resembled that of a superconductor. Fe-Pt NWs was therefore deemed not suitable for MTD as well. When treating Tera-1 cells, Fe-Pt NWs displayed an IC_{50} superior to Pt NWs of 207 µg/mL at 48 hrs.

5.2 Recommendations and Future Prospects

The use of magnetic NWs in cancer therapeutics is increasing in interest. The potential applications of Magnetic NWs include magnetic hyperthermia, magnetic actuation, contrast agents for MRI and MTD (15,57,65,208). Due to the high M_S of Fe NWs, a promising application is for Fe NWs to act as a nanocarrier for active targeted drug delivery systems. The agglomeration caused by the high M_R and low zeta potential can be combated by an engineered coating. The potential application utilising the magnetic properties of Fe NWs besides MTD involve magnetic hyperthermia, magnetic actuation, and as contrast agents for MRI. Magnetic hyperthermia and magnetic actuation will allow for multimodal cell death inducing system independent of chemotherapeutic drugs. Combined with the potential of Fe NWs to act as a MRI contrast agent, a complete theragnostic system can be designed aligning to the paradigm shift towards personalised medicine.

Pt NWs demonstrated inherent cytotoxic activity towards Tera-1 cells at high concentrations. Pt is a well-known photosensitiser and can convert energy from NIR laser irradiation to heat. The cytotoxic efficacy of Pt NWs can therefore be enhanced through the application of photothermal therapy for a bimodal cell death inducing system combining the inherent activity of Pt NWs and hyperthermia.

Although Fe coated Pt NWs displayed effective inherent cytotoxic capabilities against Tera-1 cells, biocompatibility when tested against mouse fibroblasts and applicable magnetic properties for MTD, it also possesses the greatest potential as a platform to base future therapeutic systems upon. Due to the presence of Fe and Fe oxide, which is a T2 contrast agent, Fe coated Pt NWs possesses potential as an MRI contrast agent allowing for theragnostic systems to be designed.

As Fe NWs, Fe coated Pt NWs also has great potential as a nanocarrier for chemotherapeutic agents and for applications such as magnetic hyperthermia and magnetic actuation. The large surface area and undulating surface is suitable and advantages for coating and drug loading.

The shape anisotropy and ferromagnetic properties of Fe coated Pt NWs are advantages for both magnetic hyperthermia and magnetic actuation. As in Pt NWs, the presence of Pt allows for the application of photothermal therapy as well.

As Fe coated Pt NWs, Fe-Pt NWs displayed significant inherent cytotoxic capabilities against Tera-1 cells and biocompatibility when tested against mouse fibroblasts. Due to the superconducting properties of Fe-Pt NWs, it was not suitable for MTD. The superconducting nature of Fe-Pt NWs make it an attractive option in nanophotonics.

To advance this research, the inherent multifunctionalities (contrast agent efficiency, induced cell death through hyperthermia and magnetic actuation, and cellular internalisation efficiency) need to be characterised for each of the synthesised platforms. The multifunctional NW platforms can be used to treat any solid tumour cancers or localised diseases. The exact mechanism of action for the Pt NWs and Fe/Pt NW composites will need to be determined. Comprehensive preclinical studies in an *in vivo* model needs to be undertaken for the progression of this research. The aim of which is to assess the effectiveness of the platforms to accumulate the NWs at the desired site trough MTD and to determine the pharmacokinetics of the platforms. A biocompatibility assessment is also required in the preclinical studies to ascertain the safety of the NW platforms during treatment.

REFERENCES

1. Kamran SC, Seisen T, Markt SC, Preston MA, Trinh QD, Frazier LA, et al. Contemporary treatment patterns and outcomes for clinical stage IS testicular cancer. Eur Urol. 2018;73(2):262–70.
2. Park JS, Kim J, Elghiaty A, Ham WS. Recent global trends in testicular cancer incidence and mortality. Medicine (Baltimore). 2018;97(37).
3. Oldenburg J, Fosså SD, Nuver J, Heidenreich A, Schmoll H-J, Bokemeyer C, et al. Testicular seminoma and non-seminoma: ESMO Clinical Practice Guidelines for diagnosis, treatment and follow-up†. Ann Oncol. 2013;24(SUPPL.6):vi125–32.
4. Gaddam SJ, Chesnut GT. Testicle cancer. StatPearls. 2021;
5. Jacobsen NEB, Foster RS, Donohue JP. Retroperitoneal lymph node dissection in testicular cancer. Surg Oncol Clin N Am. 2007;16(1):199–220.
6. Rogers MJ, Walsh TJ. Male infertility and risk of cancer. Semin Reprod Med. 2017;35(03):298–303.
7. Machen GL, Sandlow JI. Causes of male infertility. Male Infertil. 2020;3–14.
8. Gurevich M, Bishop S, Bower J, Malka M, Nyhof-Young J. (Dis)embodying gender and sexuality in testicular cancer. Soc Sci Med. 2004;58(9):1597–607.
9. Skoogh J, Steineck G, Cavallin-Ståhl E, Wilderäng U, Håkansson UK, Johansson B, et al. Feelings of loss and uneasiness or shame after removal of a testicle by orchidectomy: a population-based long-term follow-up of testicular cancer survivors. Int J Androl. 2011;34(2):183–92.
10. Schepisi G, De Padova S, De Lisi D, Casadei C, Meggiolaro E, Ruffilli F, et al. Psychosocial issues in long-term survivors of testicular cancer. Front Endocrinol (Lausanne). 2019;0(FEB):113.
11. Alsharif NA, Martiinez-Banderas A, Merzaban J, Ravasi T, Kosel J. Biofunctionalizing Magnetic Nanowires Toward Targeting and Killing Leukemia Cancer Cells. IEEE Trans Magn. 2019;55(2).
12. Nana ABA, Marimuthu T, Kondiah PPD, Choonara YE, Du Toit LC, Pillay V. Multifunctional magnetic nanowires: Design, fabrication, and future prospects as cancer therapeutics. Cancers (Basel). 2019;11(12):1956.
13. Martínez-Banderas AI, Aires A, Teran FJ, Perez JE, Cadenas JF, Alsharif N, et al. Functionalized magnetic nanowires for chemical and magneto-mechanical induction of cancer cell death. Sci Rep. 2016;6(1):1–11.
14. Pondman KM, Bunt ND, Maijenburg AW, Van Wezel RJA, Kishore U, Abelmann L, et al. Magnetic drug delivery with FePd nanowires. J Magn Magn Mater. 2015;380:299–306.
15. Martínez-Banderas AI, Aires A, Plaza-García S, Colás L, Moreno JA, Ravasi T, et al. Magnetic core-shell nanowires as MRI contrast agents for cell tracking. J Nanobiotechnology. 2020;18(1):1–12.
16. Egolf PW, Shamsudhin N, Pané S, Vuarnoz D, Pokki J, Pawlowski AG, et al. Hyperthermia with rotating magnetic nanowires inducing heat into tumor by fluid friction. J Appl Phys. 2016;120(6).

17. Abed A, Derakhshan M, Karimi M, Shirazinia M, Mahjoubin-Tehran M, Homayonfal M, et al. Platinum nanoparticles in biomedicine: Preparation, anti-cancer activity, and drug delivery vehicles. Front Pharmacol. 2022;13:163.

18. Bae YH, Park K. Targeted drug delivery to tumors: Myths, reality and possibility. J Control Release. 2011;153(3):198.

19. Kutova OM, Guryev EL, Sokolova EA, Alzeibak R, Balalaeva I V. Targeted delivery to tumors: Multidirectional strategies to improve treatment efficiency. Cancers 2019, Vol 11, Page 68. 2019;11(1):68.

20. Matsumura Y, Maeda H. A New concept for macromolecular therapeutics in cancer chemotherapy: mechanism of tumoritropic accumulation of proteins and the antitumor agent smancs. Cancer Res. 1986;46(12 Part 1).

21. Danhier F. To exploit the tumor microenvironment: Since the EPR effect fails in the clinic, what is the future of nanomedicine? J Control Release. 2016;244(Pt A):108–21.

22. Heidarshenas B, Wei H, Ali Moghimi Z, Hussain G, Baniasadi F, Naghieh G. Nanowires in magnetic drug targeting.

23. Snow-Lisy DC, Samplaski MK, Labhasetwar V, Sabanegh ES. Drug delivery to the testis: current status and potential pathways for the development of novel therapeutics. Drug Deliv Transl Res 2011 15. 2011;1(5):351–60.

24. Gao ZG, Fain HD, Rapoport N. Controlled and targeted tumor chemotherapy by micellar-encapsulated drug and ultrasound. J Control Release. 2005;102(1):203–22.

25. Schenck JF. Safety of strong, static magnetic fields. J Magn Reson Imaging. 2000;12:2–19.

26. Wang Y, Zhao R, Wang S, Liu Z, Tang R. In vivo dual-targeted chemotherapy of drug resistant cancer by rationally designed nanocarrier. Biomaterials. 2016;75:71–81.

27. Pan Y, Xue P, Liu S, Zhang L, Guan Q, Zhu J, et al. Metal-based hybrid nanoparticles as radiosensitizers in cancer therapy. Colloid Interface Sci Commun. 2018;23:45–51.

28. Rackwitz T, Debus J. Clinical applications of proton and carbon ion therapy. Semin Oncol. 2019;46(3):226–32.

29. Chen XZ, Hoop M, Shamsudhin N, Huang T, Özkale B, Li Q, et al. Hybrid magnetoelectric nanowires for nanorobotic applications: Fabrication, magnetoelectric coupling, and magnetically assisted in vitro targeted drug delivery. Adv Mater. 2017;29(8).

30. Doucey MA, Carrara S. Nanowire sensors in cancer. Trends Biotechnol. 2019;37(1):86–99.

31. Jones RS, Draheim RR, Roldo M. Silver nanowires: Synthesis, antibacterial activity and biomedical applications. Appl Sci 2018, Vol 8, Page 673. 2018;8(5):673.

32. Wang Z, Wu A, Ciacchi LC, Wei G. Recent advances in nanoporous membranes for water purification. Nanomater 2018, Vol 8, Page 65. 2018;8(2):65.

33. Irshad MI, Ahmad F, Mohamed NM. A review on nanowires as an alternative high density magnetic storage media. AIP Conf Proc. 2012;1482(1):625.

34. Bayrak T, Jagtap NS, Erbe A. Review of the electrical characterization of metallic nanowires on DNA templates. Int J Mol Sci 2018, Vol 19, Page 3019. 2018;19(10):3019.

35. Esteban-Fernández De Ávila B, Ramírez-Herrera DE, Campuzano S, Angsantikul P,

Zhang L, Wang J. Nanomotor-enabled pH-responsive intracellular delivery of caspase-3: Toward rapid cell apoptosis. ACS Nano. 2017;11(6):5367–74.

36. Assunção-Silva RC, Gomes ED, Silva NA, Salgado AJ. Nanoengineered biomaterials for spinal cord regeneration. Nanoeng Biomater Regen Med. 2019;167–85.

37. Pondman KM, Maijenburg AW, Celikkol FB, Pathan AA, Kishore U, Haken B Ten, et al. Au coated Ni nanowires with tuneable dimensions for biomedical applications. J Mater Chem B. 2013;1(44):6129–36.

38. Lisjak D, Mertelj A. Anisotropic magnetic nanoparticles: A review of their properties, syntheses and potential applications. Prog Mater Sci. 2018;95:286–328.

39. Banerjee S, Dan A, Chakravorty D. Review synthesis of conducting nanowires. J Mater Sci 2002 3720. 2002;37(20):4261–71.

40. Biswas A, Bayer IS, Biris AS, Wang T, Dervishi E, Faupel F. Advances in top–down and bottom–up surface nanofabrication: Techniques, applications & future prospects. Adv Colloid Interface Sci. 2012;170(1–2):2–27.

41. Mu Q, Yan B. Editorial: Nanoparticles in cancer therapy-novel concepts, mechanisms, and applications. Front Pharmacol. 2019;9(JAN):1552.

42. Fernandes C, Suares D, Yergeri MC. Tumor microenvironment targeted nanotherapy. Front Pharmacol. 2018;9.

43. Latorre A, Couleaud P, Aires A, Cortajarena AL, Somoza Á. Multifunctionalization of magnetic nanoparticles for controlled drug release: A general approach. Eur J Med Chem. 2014;82:355–62.

44. Hoosen Y, Pradeep P, Kumar P, … LDT-I journal of, 2018 U. Nanotechnology and glycosaminoglycans: Paving the way forward for ovarian cancer intervention. mdpi.com. 2018;19(3).

45. Qin W, Zheng Y, Qian BZ, Zhao M. Prostate cancer stem cells and nanotechnology: A focus on Wnt signaling. Front Pharmacol. 2017;8(MAR).

46. Date AA, Hanes J, Ensign LM. Nanoparticles for oral delivery: Design, evaluation and state-of-the-art. J Control release. 2016;240:504.

47. Din FU, Aman W, Ullah I, Qureshi OS, Mustapha O, Shafique S, et al. Effective use of nanocarriers as drug delivery systems for the treatment of selected tumors. Int J Nanomedicine. 2017;12:7291.

48. Guo D, Ji X, Wang H, Bin S, Chu B, Shi Y, et al. Silicon nanowire-based multifunctional platform for chemo-photothermal synergistic cancer therapy. J Mater Chem B. 2018;6(23):3876–83.

49. Tan H, Huang Y, Xu J, Chen B, Zhang P, Ye Z, et al. Spider toxin peptide lycosin-I functionalized gold nanoparticles for in vivo tumor targeting and therapy. Theranostics. 2017;7(12):3168–78.

50. Chen CW, Syu WJ, Huang TC, Lee YC, Hsiao JK, Huang KY, et al. Encapsulation of Au/Fe3O4 nanoparticles into a polymer nanoarchitecture with combined near infrared-triggered chemo-photothermal therapy based on intracellular secondary protein understanding. J Mater Chem B. 2017;5(29):5774–82.

51. Li T, Liu H, Xi G, Pang Y, Wu L, Wang X, et al. One-step reduction and PEIylation of PEGylated nanographene oxide for highly efficient chemo-photothermal therapy. J Mater Chem B. 2016;4(17):2972–83.

52. Sensenig R, Sapir Y, MacDonald C, Cohen S, Polyak B. Magnetic nanoparticle-based approaches to locally target therapy and enhance tissue regeneration in vivo. Nanomedicine. 2012;7(9):1425–42.

53. Liu YL, Chen D, Shang P, Yin DC. A review of magnet systems for targeted drug delivery. J Control Release. 2019;302:90–104.

54. Shen S, Wu Y, Liu Y, Wu D. High drug-loading nanomedicines: Progress, current status, and prospects. Int J Nanomedicine. 2017;12:4085–109.

55. Zhu H, Deng J, Yang Y, Li Y, Shi J, Zhao J, et al. Cobalt nanowire-based multifunctional platform for targeted chemo-photothermal synergistic cancer therapy. Colloids Surfaces B Biointerfaces. 2019;180:401–10.

56. Su Y, Wei X, Peng F, Zhong Y, Lu Y, Su S, et al. Gold nanoparticles-decorated silicon nanowires as highly efficient near-infrared hyperthermia agents for cancer cells destruction. ACS Publ. 2012;12(4):1845–50.

57. Lin W-SS, Lin H-MM, Chen H-HH, Hwu Y-KK, Chiou Y-JJ. Shape effects of iron nanowires on hyperthermia treatment. 2013;2013.

58. Fernandez-Roldan JA, Serantes D, Del Real RP, Vazquez M, Chubykalo-Fesenko O. Micromagnetic evaluation of the dissipated heat in cylindrical magnetic nanowires. Appl Phys Lett. 2018;112(21).

59. Contreras MF, Zaher A, Perez JE, Ravasi T, Kosel J. Magnetic nanowires and hyperthermia: How geometry and material affect heat production efficiency. 2015 IEEE Int Magn Conf INTERMAG 2015. 2015;1–1.

60. Alonso J, Khurshid H, Sankar V, Nemati Z, Phan MH, Garayo E, et al. FeCo nanowires with enhanced heating powers and controllable dimensions for magnetic hyperthermia. J Appl Phys. 2015;117(17):17–113.

61. Spirou S V, Basini M, Lascialfari A, Sangregorio C, Innocenti C. Magnetic hyperthermia and radiation therapy: radiobiological principles and current practice. mdpi.com. 2018;8(6).

62. Choi DSD, Kim YK, Choi DSD, Park J, Kim S, Gracias DH, et al. Hyperthermia with magnetic nanowires for inactivating living cells. 2008;8(5).

63. Hopkins X, Gill WA, Kringel R, Wang G, Hass J, Acharya S, et al. Radio frequency-mediated local thermotherapy for destruction of pancreatic tumors using Ni–Au core–shell nanowires. Nanotechnology. 2016;28(3).

64. Contreras MF, Sougrat R, Zaher A, Ravasi T, Kosel J. Non-chemotoxic induction of cancer cell death using magnetic nanowires. Int J Nanomedicine. 2015;10:2141–53.

65. Fung AO, Kapadia V, Pierstorff E, Ho D, Chen Y. Induction of cell death by magnetic actuation of nickel nanowires internalized by fibroblasts. J Phys Chem C. 2008;112(39):15085–8.

66. Zablotskii V, Lunov O, Novotná B, Churpita O, Trošan P, Holáň V, et al. Down-regulation of adipogenesis of mesenchymal stem cells by oscillating high-gradient magnetic fields and mechanical vibration. Appl Phys Lett. 2014;105(10).

67. Serrà A, Vázquez-Mariño G, García-Torres J, Bosch M, Vallés E, Serrà A, et al. Magnetic actuation of multifunctional nanorobotic platforms to induce cancer cell death. Wiley Online Libr. 2018;2(2).

68. Nielsch K, Wehrspohn RB, Barthel J, Kirschner J, Gösele U, Fischer SF, et al. Hexagonally ordered 100 nm period nickel nanowire arrays. Appl Phys Lett.

2001;79(9):1360.

69. Alia SM, Pylypenko S, Dameron A, - A, Wei Wang X, Tao Fei G, et al. Tuning the magnetic anisotropy of Co–Ni nanowires: Comparison between single nanowires and nanowire arrays in hard-anodic aluminum oxide membranes. iopscience.iop.org. 2012;23(46):465709.

70. Ferré R, Ounadjela K, George J. Magnetization processes in nickel and cobalt electrodeposited nanowires. Phys Rev B - Condens Matter Mater Phys. 1997;56(21):14066–75.

71. Krekhno R V, Safronov AP, Beketov - I V, Reza Yasemian A, Almasi Kashi M, Ramazani - A, et al. Magnetic particle hyperthermia: nanoparticle magnetism and materials development for cancer therapy. iopscience.iop.org. 2006;18(38):2919–34.

72. Glöckl G, Hergt R, Zeisberger M, Dutz S, Nagel S, Weitschies W. The effect of field parameters, nanoparticle properties and immobilization on the specific heating power in magnetic particle hyperthermia. J Phys Condens Matter. 2006;18(38).

73. Kossatz S, Grandke J, Couleaud P, Latorre A, Aires A, Crosbie-Staunton K, et al. Efficient treatment of breast cancer xenografts with multifunctionalized iron oxide nanoparticles combining magnetic hyperthermia and anti-cancer drug delivery. Breast Cancer Res. 2015;17(1).

74. Gao W, Kagan D, Pak S, Clawson C, Campuzano S, Chuluun-Erdene E, et al. Cargo-towing fuel-free magnetic nanoswimmers for targeted drug delivery. Wiley Online Libr. 2012;8(3):460–7.

75. Gao W, de Ávila BEF, Zhang L, Wang J. Targeting and isolation of cancer cells using micro/nanomotors. Adv Drug Deliv Rev. 2018;125:94–101.

76. Liu XL, Fan HM. Innovative magnetic nanoparticle platform for magnetic resonance imaging and magnetic fluid hyperthermia applications. Curr Opin Chem Eng. 2014;4:38–46.

77. Bose RJC, Lee SH, Park H. Biofunctionalized nanoparticles: An emerging drug delivery platform for various disease treatments. Drug Discov Today. 2016;21(8):1303–12.

78. Ivanov YYP, Alfadhel A, Alnassar M, Perez JE, Vazquez M, Chuvilin A, et al. Tunable magnetic nanowires for biomedical and harsh environment applications. Sci Rep. 2016;6:24189.

79. Isaac A, Banderas M. A combined chemical and magneto-mechanical induction of cancer cell death by the use of functionalized magnetic iron nanowires. 2016;

80. Sneider A, Vandyke D, Paliwal S, Rai P. Remotely triggered nano-theranostics for cancer applications. Nanotheranostics. 2017;1(1):1–22.

81. Lee N, Hyeon T. Designed synthesis of uniformly sized iron oxide nanoparticles for efficient magnetic resonance imaging contrast agents. Chem Soc Rev. 2012;41(7):2575–89.

82. Shore D, Pailloux SL, Zhang J, Gage T, Flannigan DJ, Garwood M, et al. Electrodeposited Fe and Fe-Au nanowires as MRI contrast agents. Chem Commun. 2016;52(85):12634–7.

83. Bañobre-López M, Bran C, Rodríguez-Abreu C, Gallo J, Vázquez M, Rivas J. A colloidally stable water dispersion of Ni nanowires as an efficient: T 2-MRI contrast agent. J Mater Chem B. 2017;5(18):3338–47.

84. Staňo M, Fruchart O. Magnetic nanowires and nanotubes. In: Brück E, editor.

Handbook of Magnetic Materials. 27th ed. Elsevier; 2018. p. 155–267.

85. Sumanth Kumar D, Jai Kumar B, Mahesh HM. Quantum Nanostructures (QDs): An Overview. Synth Inorg Nanomater. 2018;59–88.

86. Li X, Sun L, Wang H, Xie K, Long Q, Lai X, et al. Synthesis of cobalt nanowires in aqueous solution under an external magnetic field. Beilstein J Nanotechnol. 2016;7(1):990–4.

87. Zhao ZJ, Hwang SH, Jeon S, Jung JY, Lee J, Choi DG, et al. Effects of polymer surface energy on morphology and properties of silver nanowire fabricated via nanoimprint and E-beam evaporation. Appl Surf Sci. 2017;420:429–38.

88. Datta A, Sangle A, Hardingham N, Cooper C, Kraan M, Ritchie D, et al. Structure and thermoelectric properties of Bi2-xSbxTe3 nanowires grown in flexible nanoporous polycarbonate templates. Materials (Basel). 2017;10(5).

89. Demeo D, Macnaughton S, Sonkusale S, Vandervelde TE. Electrodeposited Copper oxide and Zinc Oxide core-shell Nanowire photovoltaic cells. In: Hashim AA, editor. Nanowires - Implementations and Applications. 2011.

90. Yu Y, Li J, Wang J, Wu X, Yu C, Xu T, et al. Orientation growth and magnetic properties of electrochemical deposited nickel nanowire arrays. mdpi.com. 2019;9(2).

91. Serrà A, Vallés E. Advanced electrochemical synthesis of multicomponent metallic nanorods and nanowires: Fundamentals and applications. Appl Mater Today. 2018;12:207–34.

92. Oviroh PO, Akbarzadeh R, Pan D, Alfred R, Coetzee M, Jen T-C. New development of atomic layer deposition: Processes, methods and applications. Taylor Fr. 2019;20(1):465–96.

93. Martín-Palma RJ, Lakhtakia A. Vapor-deposition techniques. Eng Biomimicry. 2013;383–98.

94. Kuppusami P, Raghunathan VS. Status of pulsed laser deposition: Challenges and opportunities. Surf Eng. 2006;22(2):81–3.

95. De Teresa JM, Fernández-Pacheco A, Córdoba R, Serrano-Ramón L, Sangiao S, Ibarra MR. Review of magnetic nanostructures grown by focused electron beam induced deposition (FEBID). J Phys D Appl Phys. 2016;49(24).

96. Nguyen DM, Bich HN, Hai Anh PD, Ai-Le PH, Bui QB. Vertical copper oxide nanowire arrays attached three-dimensional macroporous framework as a self-supported sensor for sensitive hydrogen peroxide detection. Arab J Chem. 2020;13(2):3934–45.

97. Pirouzfar A, Seyyed Ebrahimi SA. Optimization of sol-gel synthesis of CoFe2O4 nanowires using template assisted vacuum suction method. J Magn Magn Mater. 2014;370:1–5.

98. Hamdana G, Südkamp T, Descoins M, Mangelinck D, Caccamo L, Bertke M, et al. Towards fabrication of 3D isotopically modulated vertical silicon nanowires in selective areas by nanosphere lithography. Microelectron Eng. 2017;179:74–82.

99. Ferreira JM, Souza KP, Queiroz FM, Costa I, Tomachuk CR. Electrochemical and chemical characterization of electrodeposited zinc surface exposed to new surface treatments. Surf Coatings Technol. 2016;294:36–46.

100. Loto CA. Electroless nickel plating–a review. Silicon. 2016;8(2):177–86.

101. Asadian E, Ghalkhani M, Shahrokhian S. Electrochemical sensing based on carbon

nanoparticles: A review. Sensors Actuators, B Chem. 2019;293:183–209.

102. Jamkhande PG, Ghule NW, Bamer AH, Kalaskar MG. Metal nanoparticles synthesis: An overview on methods of preparation, advantages and disadvantages, and applications. J Drug Deliv Sci Technol. 2019;53.

103. Ghosh S. Electroless copper deposition: A critical review. Thin Solid Films. 2019;669:641–58.

104. Possin GE. A Method for forming very small diameter wires. Rev Sci Instrum. 2003;41(5):772.

105. Pérez-Page M, Yu E, Li J, Rahman M, Dryden DM, Vidu R, et al. Template-based syntheses for shape controlled nanostructures. Adv Colloid Interface Sci. 2016;234:51–79.

106. Gontad F, Caricato AP, Cesaria M, Resta V, Taurino A, Colombelli A, et al. Decoration of silica nanowires with gold nanoparticles through ultra-short pulsed laser deposition. Appl Surf Sci. 2017;418:430–6.

107. Li H, Guan L, Xu Z, Zhao Y, Sun J, Wu J, et al. Synthesis and characterization of amorphous SiO 2 nanowires via pulsed laser deposition accompanied by N 2 annealing. Appl Surf Sci. 2016;389:705–12.

108. Nikov RG, Dikovska AO, Atanasova GB, Avdeev G V., Nedyalkov NN. Magnetic-field-assisted formation of oriented nanowires produced by pld in open air. Appl Surf Sci. 2018;458:273–80.

109. Qiu Z, Gong H, Yang X, Zhang Z, Han J, Cao B, et al. Phosphorus concentration dependent microstructure and optical property of zno nanowires grown by high-pressure pulsed laser deposition. J Phys Chem C. 2015;119(8):4371–8.

110. Shkurmanov A, Sturm C, Hochmuth H, Grundmann M. Growth kinetics of ultrathin ZnO nanowires grown by pulsed laser deposition. Procedia Eng. 2016;168:1156–9.

111. Nikov RG, Dikovska AO, Avdeev G V., Amoruso S, Ausanio G, Nedyalkov NN. PLD fabrication of oriented nanowires in magnetic field. Appl Surf Sci. 2019;471:368–74.

112. Contreras MFMMF, Ravasi T, Kosel J, Conference JK-2nd ME, 2014 U, Kosel J. Targeted cancer cell death induced by biofunctionalized magnetic nanowires. Middle East Conf Biomed Eng MECBME. 2014;47–50.

113. Sun D, Kang S, Liu C, Lu Q, Cui L, Sci BH-IJE, et al. Effect of zeta potential and particle size on the stability of SiO2 nanospheres as carrier for ultrasound imaging contrast agents. electrochemsci.org. 2016;11(10):8520–9.

114. Hussain M, Xie J, Hou Z, Shezad K, Xu J, Wang K, et al. Regulation of drug release by tuning surface textures of biodegradable polymer microparticles. ACS Publ. 2017;9(16):14391–400.

115. Zhang H, Xu H, Wu M, Zhong Y, Wang D, Jiao Z. A soft-hard template approach towards hollow mesoporous silica nanoparticles with rough surfaces for controlled drug delivery and protein adsorption. J Mater Chem B. 2015;3(31):6480–9.

116. Peng F, Su Y, Wei X, Lu Y, Zhou Y, Zhong Y, et al. Silicon-nanowire-based nanocarriers with ultrahigh drug-loading capacity for in vitro and in vivo cancer therapy. Angew Chemie - Int Ed. 2013;52(5):1457–61.

117. Wang J, Kumeria T, Bezem MT, Wang J, Sailor MJ. Self-reporting photoluminescent porous silicon microparticles for drug delivery. ACS Appl Mater Interfaces. 2018;10(4):3200–9.

118. Lorenz MR, Holzapfel V, Musyanovych A, Nothelfer K, Walther P, Frank H, et al. Uptake of functionalized, fluorescent-labeled polymeric particles in different cell lines and stem cells. Biomaterials. 2006;27(14):2820–8.

119. Murugan K, Choonara YEY, Kumar P, Bijukumar D, du Toit LC, Pillay V, et al. Parameters and characteristics governing cellular internalization and trans-barrier trafficking of nanostructures. 2015;10(1):2191–206.

120. Chithrani BD, Ghazani AA, Chan WCW. Determining the size and shape dependence of gold nanoparticle uptake into mammalian cells. Nano Lett. 2006;6(4):662–8.

121. Fröhlich E. The role of surface charge in cellular uptake and cytotoxicity of medical nanoparticles. Int J Nanomedicine. 2012;7:5577–91.

122. Behzadi S, Serpooshan V, Tao W, Hamaly MA, Alkawareek MY, Dreaden EC, et al. Cellular uptake of nanoparticles: Journey inside the cell. Chem Soc Rev. 2017;46(14):4218–44.

123. Panzarini E, Mariano S, Carata E, Mura F, Rossi M, Dini L. Intracellular transport of silver and gold nanoparticles and biological responses: an update. mdpi.com. 2018;19(5).

124. Awaad A, Nakamura M, Ishimura K. Imaging of size-dependent uptake and identification of novel pathways in mouse Peyer's patches using fluorescent organosilica particles. Nanomedicine Nanotechnology, Biol Med. 2012;8(5):627–36.

125. Prina-Mello A, Diao Z, Coey JMD. Internalization of ferromagnetic nanowires by different living cells. J Nanobiotechnology. 2006;4.

126. Meng-Meng S, Song MM, Song WJ, Bi H, Wang J, Wu WL, et al. Cytotoxicity and cellular uptake of iron nanowires. Biomaterials. 2010;31(7):1509–17.

127. Choi D, Fung A, Moon H, Ho D, Chen Y, Kan E, et al. Transport of living cells with magnetically assembled nanowires. Biomed Microdevices. 2007;9(2):143–8.

128. Poland CA, Byrne F, Cho W-S, Prina-Mello A, Murphy FA, Davies GL, et al. Length-dependent pathogenic effects of nickel nanowires in the lungs and the peritoneal cavity. Taylor Fr. 2011;6(8):1–13.

129. Wong PK. Mutagenicity of heavy metals. Bull Environ Contam Toxicol. 1988;40(4):597–603.

130. Žužek Rožman K, Pečko D, Šturm S, Maver U, Nadrah P, Bele M, et al. Electrochemical synthesis and characterization of Fe 70Pd 30 nanotubes for drug-delivery applications. Mater Chem Phys. 2012;133(1):218–24.

131. Donaldson K, Tran CL. An introduction to the short-term toxicology of respirable industrial fibres. Mutat Res - Fundam Mol Mech Mutagen. 2004;553(1–2):5–9.

132. Magrez A, Kasas S, Salicio V, Pasquier N, Seo JW, Celio M, et al. Cellular toxicity of carbon-based nanomaterials. Nano Lett. 2006;6(6):1121–5.

133. Rahong S, Yasui T, Kaji N, Baba Y. Recent developments in nanowires for bio-applications from molecular to cellular levels. Lab Chip. 2016;16(7):1126–38.

134. Jahangirian H, Kalantari K, Izadiyan Z, Rafiee-Moghaddam R, Shameli K, Webster TJ. A review of small molecules and drug delivery applications using gold and iron nanoparticles. Int J Nanomedicine. 2019;14:1633–57.

135. Safi M, Yan M, Guedeau-Boudeville M-AA, Elè Ne Conjeaud H, Garnier-Thibaud V, Boggetto N, et al. Interactions between magnetic nanowires and living cells: uptake,

toxicity, and degradation. ACS Nano. 2011;5(7):5354–64.

136. Perez JE, Contreras MF, Vilanova E, Felix LP, Margineanu MB, Luongo G, et al. Cytotoxicity and intracellular dissolution of nickel nanowires. Nanotoxicology. 2016;10(7):871–80.

137. Liu J, Yu M, Zhou C, Zheng J. Renal clearable inorganic nanoparticles: A new frontier of bionanotechnology. Mater Today. 2013;16(12):477–86.

138. Price PM, Mahmoud WE, Al-Ghamdi AA, Bronstein LM. Magnetic drug delivery: Where the field is going. Front Chem. 2018;6(DEC):619.

139. Dulińska-Litewka J, Łazarczyk A, Hałubiec P, Szafrański O, Karnas K, Karewicz A. Superparamagnetic iron oxide nanoparticles-current and prospective medical applications. Materials (Basel). 2019;12(4).

140. Mukhtar A, Wu K, Cao X, Gu liyuan. Magnetic nanowires in biomedical applications. Nanotechnology. 2020;31(43):433001.

141. Keshoju K, Xing H, Sun L. Magnetic field driven nanowire rotation in suspension. Appl Phys Lett. 2007;91(12):123114.

142. A Hultgren MTCCGMDR, Hultgren A, Tanase M, Chen CS, Meyer GJ, Reich DH. Cell manipulation using magnetic nanowires. J Appl Phys. 2003;93(10).

143. N Gao HWEY, Gao N, Wang H, Yang EH. An experimental study on ferromagnetic nickel nanowires functionalized with antibodies for cell separation. Nanotechnology. 2010;21(10):8.

144. The Editors of Encyclopaedia. magnetic field strength. In Encyclopedia Britannica; 2020.

145. Nave CR. Magnetic properties of solids [Internet]. Hyperphysics. Atlanta, Georgia 30302-5060: Georgia State University; 2012.

146. Britannica TE of E. magnetic susceptibility | physics |. In Britannica; 2006.

147. McHenry ME, Laughlin DE. Magnetic properties of metals and alloys. Phys Metall Fifth Ed. 2014;1:1881–2008.

148. Hultgren A, Tanase M, Felton EJ, Bhadriraju K, Salem AK, Chen CS, et al. Optimization of yield in magnetic cell separations using nickel nanowires of different lengths. Biotechnol Prog. 2005;21(2):509–15.

149. Gu L, Cao X, Mukhtar A, Wu K. Structural characterization and magnetic properties of core–shell Fe@Fe3O4 nanowires. Appl Phys A Mater Sci Process. 2020;126(6):458.

150. Sun L, Hao Y, Chien CL, Searson PC, Searson PC. Tuning the properties of magnetic nanowires. IBM J Res Dev. 2005;49(1):79–102.

151. McBain SC, Yiu HHP, Dobson J. Magnetic nanoparticles for gene and drug delivery. Int J Nanomedicine. 2008;3(2):169.

152. Arora A. Optical and electric field control of magnetism. Institutional Repository of the University of Potsdam. University of Potsdam; 2018.

153. Tauxe L. Essentials of paleomagnetism. 2010;506.

154. Contreras MF. Magnetic nanowires as materials for cancer cell destruction. King Abdullah University of Science and Technology; 2015.

155. Bahadur D, Giri J. Biomaterials and magnetism. Sadhana 2003 283. 2003;28(3):639–

56.

156. Nasirpouri F. Template electrodeposition of nanowires arrays. Springer Ser Surf Sci. 2017;62:187–259.

157. Penner RM, Martin CR. Preparation and electrochemical characterization of ultramicroelectrode ensembles. Anal Chem. 1987;59(21):2625–30.

158. Singh A, Philipose U. Understanding the mechanisms that affect the quality of electrochemically grown semiconducting nanowires. Semicond - Growth Charact. 2017;

159. Blanco S, Vargas R, Mostany J, Borrás C, Scharifker BR. Modeling the growth of nanowire arrays in porous membrane templates. J Electrochem Soc. 2014;161(8):E3341–7.

160. Bloch K, Pardesi K, Satriano C, Ghosh S. Bacteriogenic platinum nanoparticles for application in nanomedicine. Front Chem. 2021;9:32.

161. Hullo M, Grall R, Perrot Y, Mathé C, Ménard V, Yang X, et al. Radiation enhancer effect of platinum nanoparticles in breast cancer cell lines: In vitro and in silico analyses. Int J Mol Sci. 2021;22(9).

162. Manikandan M, Hasan N, Wu HF. Platinum nanoparticles for the photothermal treatment of Neuro 2A cancer cells. Biomaterials. 2013;34(23):5833–42.

163. Bendale Y, Bendale V, Paul S. Evaluation of cytotoxic activity of platinum nanoparticles against normal and cancer cells and its anticancer potential through induction of apoptosis. Integr Med Res. 2017;6(2):141–8.

164. Gurunathan S, Jeyaraj M, Kang M-H, Kim J-H. Anticancer properties of platinum nanoparticles and retinoic acid: Combination therapy for the treatment of tuman neuroblastoma cancer. Int J Mol Sci. 2020;21(18):6792.

165. Sukhanova A, Bozrova S, Sokolov P, Berestovoy M, Karaulov A, Nabiev I. Dependence of nanoparticle toxicity on their physical and chemical properties. Nanoscale Res Lett. 2018;13.

166. Zhao X, Ng S, Heng BC, Guo J, Ma L, Tan TTY, et al. Cytotoxicity of hydroxyapatite nanoparticles is shape and cell dependent. Arch Toxicol. 2013;87(6):1037–52.

167. Bhattacharya R, Mukherjee P. Biological properties of “naked” metal nanoparticles. Adv Drug Deliv Rev. 2008;60(11):1289–306.

168. Gao J, Liang G, Zhang B, Kuang Y, Zhang X, Xu B. FePt@CoS2 yolk-shell nanocrystals as a potent agent to kill HeLa cells. J Am Chem Soc. 2007;129(5):1428–33.

169. Jacob JA, Salmani JMM, Chen B. Magnetic nanoparticles: Mechanistic studies on the cancer cell interaction. Nanotechnol Rev. 2016;5(5):481–8.

170. Zeng X, Sun J, Li S, Shi J, Gao H, Sun Leong W, et al. Blood-triggered generation of platinum nanoparticle functions as an anti-cancer agent. Nat Commun 2020 111. 2020;11(1):1–12.

171. Pawar AA, Sahoo J, Verma A, Lodh A, Lakkakula J. Usage of platinum nanoparticles for anticancer therapy over last decade: a review. Part Part Syst Charact. 2021;38(10):2100115.

172. Choi DS, Fung AO, Moon H, Villareal G, Chen Y, Ho D, et al. Detection of Neural Signals with Vertically Grown Single Platinum Nanowire-Nanobud. J Nanosci Nanotechnol. 2009;9(11):6483–6.

173. Jin YH, Daubinger P, Fiebich BL, Stieglitz T. A novel platinum nanowire-coated neural electrode and its electrochemical and biological characterization. Proc IEEE Int Conf Micro Electro Mech Syst. 2011;1003–6.

174. Magrez A, Horváth L, Smajda R, Salicio V, Pasquier N, Forró L, et al. Cellular toxicity of TiO2-based nanofilaments. ACS Nano. 2009;3(8):2274–80.

175. Riss TL, Moravec RA, Niles AL, Duellman S, Benink HA, Worzella TJ, et al. Cell viability assays. Assay Guid Man. 2016;

176. Aslantürk ÖS. In vitro cytotoxicity and cell viability assays: Principles, advantages, and disadvantages. In: Larramendy ML, Soloneski S, editors. Genotoxicity - A Predictable Risk to Our Actual World. IntechOpen; 2017.

177. Raphael MP, Christodoulides JA, Qadri SN, Simpkins BS, Byers JM. Magnetic moment degradation of nanowires in biological media: real-time monitoring with SQUID magnetometry. Nanotechnology. 2010;21(28):285101.

178. de Faria DLA, Venâncio Silva S, de Oliveira MT. Raman microspectroscopy of some iron oxides and oxyhydroxides. J Raman Spectrosc. 1997;28(11):873–8.

179. Sharma M, Kuanr BK. Electrodeposition of ferromagnetic nanostructures. Electroplat Nanostructures. 2015;

180. Wu Z, Liu Y, Deng C, Zhao H, Zhao R, Chen H. The critical role of boric acid as electrolyte additive on the electrochemical performance of lead-acid battery. J Energy Storage. 2020;27:101076.

181. Martínez-Banderas AI, Aires A, Quintanilla M, Holguín-Lerma JA, Lozano-Pedraza C, Teran FJ, et al. Iron-based core-shell nanowires for combinatorial drug delivery and photothermal and magnetic therapy. ACS Appl Mater Interfaces. 2019;11(47):43976–88.

182. Qu F, Yang M, Shen G, Yu R. Electrochemical biosensing utilizing synergic action of carbon nanotubes and platinum nanowires prepared by template synthesis. Biosens Bioelectron. 2007;22(8):1749–55.

183. Terohid SAA, Heidari S, Jafari A, Asgary S. Effect of growth time on structural, morphological and electrical properties of tungsten oxide nanowire. 2018;124(8):1–9.

184. Park CY, Kim EH, Kim JH, Lee YM, Kim JH. Novel semi-alicyclic polyimide membranes: Synthesis, characterization, and gas separation properties. Polymer (Guildf). 2018;151:325–33.

185. Yin H, Zhao S, Zhao K, Muqsit A, Tang H, Chang L, et al. Ultrathin platinum nanowires grown on single-layered nickel hydroxide with high hydrogen evolution activity. Nat Commun 2015 61. 2015;6(1):1–8.

186. Shebanova ON, Lazor P. Raman study of magnetite (Fe3O4): laser-induced thermal effects and oxidation. J Raman Spectrosc. 2003;34(11):845–52.

187. Singh AK, Mandal K. Effect of aspect ratio and temperature on magnetic properties of permalloy nanowires. J Nanosci Nanotechnol. 2014;14(7):5036–41.

188. Crangle J V., Goodman GM. The magnetization of pure iron and nickel. Proc R Soc London A Math Phys Sci. 1971;321:477–91.

189. Gurunathan S, Jeyaraj M, La H, Yoo H, Choi Y, Do JT, et al. Anisotropic platinum nanoparticle-induced cytotoxicity, apoptosis, inflammatory response, and transcriptomic and molecular pathways in human acute monocytic leukemia cells. Int J Mol Sci. 2020;21(2):440.

190. Sung H, Ferlay J, Siegel RL, Laversanne M, Soerjomataram I, Jemal A, et al. Global cancer statistics 2020: GLOBOCAN estimates of incidence and mortality worldwide for 36 cancers in 185 countries. CA Cancer J Clin. 2021;71(3):209–49.

191. Faraji AH, Wipf P. Nanoparticles in cellular drug delivery. Bioorganic Med Chem. 2009;17(8):2950–62.

192. Senapati S, Mahanta AK, Kumar S, Maiti P. Controlled drug delivery vehicles for cancer treatment and their performance. Signal Transduct Target Ther 2018 31. 2018;3(1):1–19.

193. Kim Y-D, Park T-E, Singh B, Maharjan S, Cho K-S, Park K, et al. Image-guided nanoparticle-based siRNA delivery for cancer therapy. Curr Pharm Des. 2015;21(31):4637–56.

194. Sun D, Chen J, Wang Y, Ji H, Peng R, Jin L, et al. Advances in refunctionalization of erythrocyte-based nanomedicine for enhancing cancer-targeted drug delivery. Theranostics. 2019;9(23):6885–900.

195. Yoo E, Samardak AY, Jeon YS, Samardak AS, Ognev A V., Komogortsev S V., et al. Composition-driven crystal structure transformation and magnetic properties of electrodeposited Co–W alloy nanowires. J Alloys Compd. 2020;843:155902.

196. BLUM, W. The structure and properties of alternately electrodeposited metals. Trans Am Electrochem Soc. 1921;40:307.

197. Reyes D, Biziere N, Warot-Fonrose B, Wade T, Gatel C. Magnetic configurations in Co/Cu multilayered nanowires: evidence of structural and magnetic interplay. Nano Lett. 2016;16(2):1230–6.

198. Chen M, Searson PC, Chien CL. Micromagnetic behavior of electrodeposited Ni/Cu multilayer nanowires. J Appl Phys. 2003;93(10):8253.

199. Um J, Zamani Kouhpanji MR, Liu S, Nemati Porshokouh Z, Sung SY, Kosel J, et al. Fabrication of long-range ordered aluminum oxide and Fe/Au multilayered nanowires for 3-D magnetic memory. IEEE Trans Magn. 2020;56(2).

200. Thomas MA, Cui JB. Core-shell nanowire arrays of metal oxides fabricated by atomic layer deposition. J Vac Sci Technol A Vacuum, Surfaces, Film. 2011;30(1):01A116.

201. Martín-García L, Ruiz-Gómez S, Abuín M, Montaña Y, Carmona N, Pérez L. Multifunctional core–shell Co–SiO2 nanowires via electrodeposition and sol–gel techniques. RSC Adv. 2015;5(118):97503–7.

202. Spain E, McCooey A, Dolan C, Bagshaw H, Leddy N, Keyes TE, et al. Electrodeposited gold–copper core–shell nanowires for high sensitivity DNA detection. Analyst. 2014;139(21):5504–8.

203. Kalska-Szostko B, Klekotka U, Satuła D. Core-shell magnetic nanowires fabrication and characterization. Appl Surf Sci. 2017;396:1855–9.

204. Rodríguez LA, Bran C, Reyes D, Berganza E, Vázquez M, Gatel C, et al. Quantitative nanoscale magnetic study of isolated diameter-modulated FeCoCu nanowires. ACS Nano. 2016;10(10):9669–78.

205. Raval N, Maheshwari R, Kalyane D, Youngren-Ortiz SR, Chougule MB, Tekade RK. Importance of physicochemical characterization of nanoparticles in pharmaceutical product development. Tekade RK, editor. Basic Fundamentals of Drug Delivery. Academic Press; 2019. 369–400 p.

206. Cao X, Gu L, Hu S, Mukhtar A, Wu K. Fe/Mn multilayer nanowires as high-performance

T1-T2 dual modal MRI contrast agents. Mater 2021, Vol 14, Page 2238. 2021;14(9):2238.

207. Gokhfeld DM. Analysis of superconductor magnetization hysteresis. J Sib Fed Univ Math Phys. 2018;11(2):219–21.

208. Kianfar E. Magnetic nanoparticles in targeted drug delivery: a review. J Supercond Nov Magn 2021 347. 2021;34(7):1709–35.

Appendix A: Publications

cancers

MDPI

Review

Multifunctional Magnetic Nanowires: Design, Fabrication, and Future Prospects as Cancer Therapeutics

Abu Bakr A. Nana, Thashree Marimuthu, Pierre P. D. Kondiah, Yahya E. Choonara, Lisa C. Du Toit and Viness Pillay *

Wits Advanced Drug Delivery Platform Research Unit, Department of Pharmacy and Pharmacology, School of Therapeutic Sciences, University of the Witwatersrand, Johannesburg, 7 York Road, Parktown 2193, South Africa; abubakr.nana@gmail.com (A.B.A.N.); thashree.marimuthu@wits.ac.za (T.M.); pierre.kondiah@wits.ac.za (P.P.D.K.); yahya.choonara@wits.ac.za (Y.E.C.); lisa.dutoit1@wits.ac.za (L.C.D.T.)

* Correspondence: viness.pillay@wits.ac.za; Tel.: +27-11-717-2274

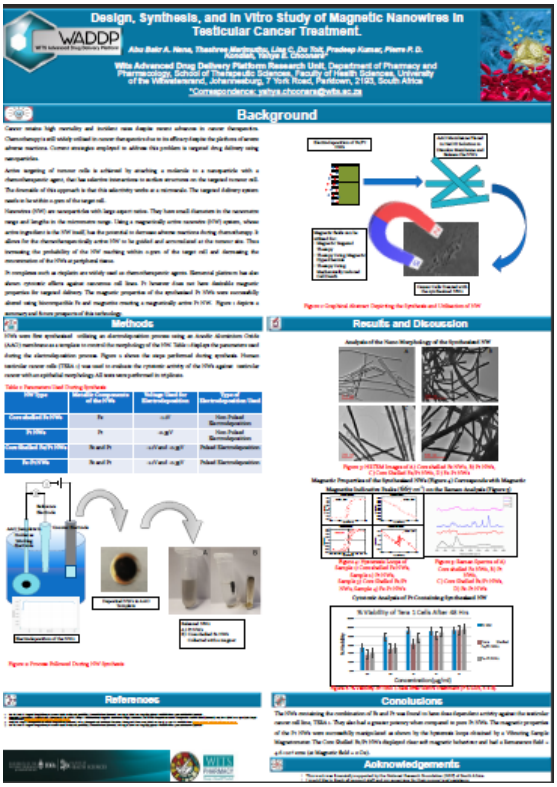
Received: 5 November 2019; Accepted: 25 November 2019; Published: 6 December 2019

check for updates

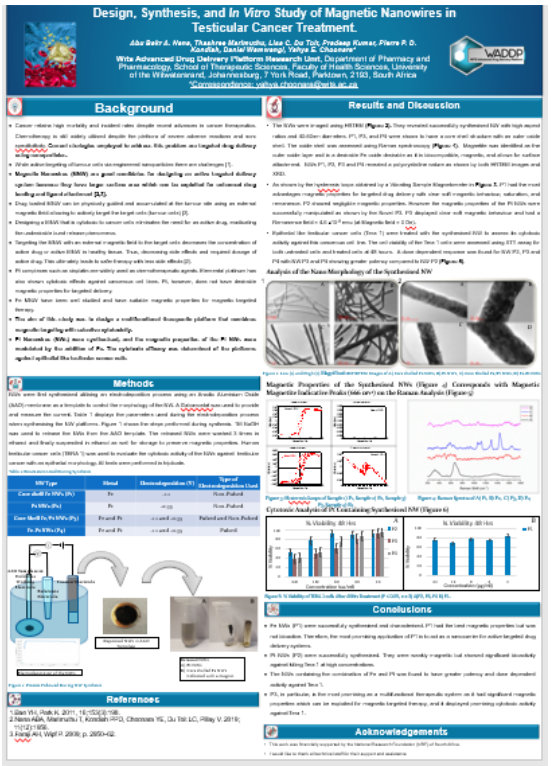
Appendix B: Research Outputs (Oral and Poster Presentations)

Poster:

School of Therapeutic Sciences Biennial Research Day 2021, University of the Witwatersrand, Johannesburg, South Africa, September 14th, 2021.



10th Annual Nanosciences Young Researchers' Symposium (NYRS-2020/21)-National, South Africa, October 7th, and 8th 2021.

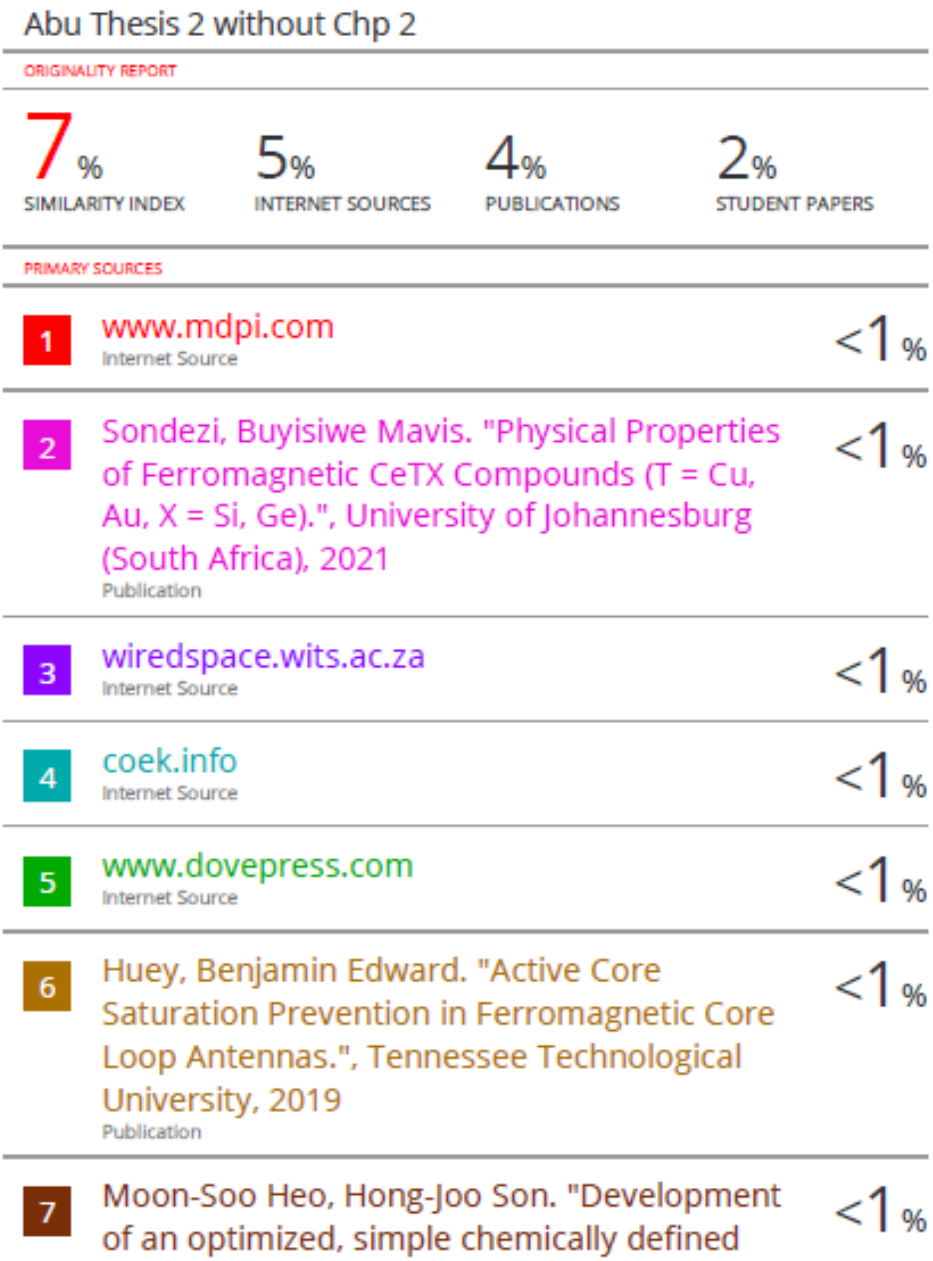


Oral Presentations

BRICS Symposium - International, South Africa, October 7th, and 8th 2021.



Appendix C: Similarity Report



Abu Thesis 2 without Chp 2

ORIGINALITY REPORT

7%	5%	4%	2%
SIMILARITY INDEX	INTERNET SOURCES	PUBLICATIONS	STUDENT PAPERS

PRIMARY SOURCES

1	www.mdpi.com Internet Source	<1%
2	Sondezi, Buyisiwe Mavis. "Physical Properties of Ferromagnetic CeTX Compounds (T = Cu, Au, X = Si, Ge).", University of Johannesburg (South Africa), 2021 Publication	<1%
3	wiredspace.wits.ac.za Internet Source	<1%
4	coek.info Internet Source	<1%
5	www.dovepress.com Internet Source	<1%
6	Huey, Benjamin Edward. "Active Core Saturation Prevention in Ferromagnetic Core Loop Antennas.", Tennessee Technological University, 2019 Publication	<1%
7	Moon-Soo Heo, Hong-Joo Son. "Development of an optimized, simple chemically defined	<1%

	medium for bacterial cellulose production by Acetobacter sp. A9 in shaking cultures", Biotechnology and Applied Biochemistry, 2002 Publication	
8	id.scribd.com Internet Source	<1 %
9	G. Mwendwa, D. Wamwangi, B. Mathe, R. Erasmus, D. Billing, A. Shnier, M. Madhuku. "Elastic and magnetic properties of Tb-MnO based thin films", Journal of Magnetism and Magnetic Materials, 2021 Publication	<1 %
10	Submitted to Queen Mary and Westfield College Student Paper	<1 %
11	Birsan, Marius Stefan. "Methods of Correlating Texture and Magnetic Properties in Electrical Steels", McGill University (Canada), 2021 Publication	<1 %
12	Submitted to Higher Education Commission Pakistan Student Paper	<1 %
13	Katarzyna E Hnida, Svenja Bäβler, Lewis Akinsinde, Johannes Gooth et al. "Tuning the polarity of charge transport in InSb nanowires via heat treatment", Nanotechnology, 2015 Publication	<1 %

14	ris.utwente.nl Internet Source	<1 %
15	vital.seals.ac.za:8080 Internet Source	<1 %
16	Mitchell. "Electrical, Magnetic, and Optical Properties of Materials", An Introduction to Materials Engineering and Science, 11/21/2003 Publication	<1 %
17	Submitted to University of Witwatersrand Student Paper	<1 %
18	digitalcommons.lsu.edu Internet Source	<1 %
19	pubs.rsc.org Internet Source	<1 %
20	Submitted to Liverpool John Moores University Student Paper	<1 %
21	ujcontent.uj.ac.za Internet Source	<1 %
22	www.differencebetween.com Internet Source	<1 %
23	Richard K. Burdick, David J. LeBlond, Lori B. Pfahler, Jorge Quiroz, Leslie Sidor, Kimberly Vukovinsky, Lanju Zhang. "Statistical	<1 %

	Applications for Chemistry, Manufacturing and Controls (CMC) in the Pharmaceutical Industry", Springer Science and Business Media LLC, 2017 Publication	
24	jcpr.kbs-lab.co.kr Internet Source	<1 %
25	publications.aston.ac.uk Internet Source	<1 %
26	publications.lib.chalmers.se Internet Source	<1 %
27	repositories.lib.utexas.edu Internet Source	<1 %
28	uwspace.uwaterloo.ca Internet Source	<1 %
29	kyutech.repo.nii.ac.jp Internet Source	<1 %
30	Fernanda Gabrielle Soares da Silva, Greicy Kelly Cerqueira dos Santos, Sakae Yotsumoto Neto, Rita de Cássia Silva Luz et al. "Self-powered sensor for tannic acid exploiting visible LED light as excitation source", Electrochimica Acta, 2018 Publication	<1 %
31	cyberleninka.org Internet Source	<1 %

32	Submitted to University of Hull Student Paper	<1 %
33	N. S. POSTMA, C. C. HERMSEN, D. J. A. CROMMELIN, J. ZUIDEMA, W. M. C. ELING. " Treatment with recombinant human tumour necrosis factor-α reduces parasitaemia and prevents K173-induced experimental cerebral malaria in mice ", Parasitology, 1999 Publication	<1 %
34	www.ncbi.nlm.nih.gov Internet Source	<1 %
35	Submitted to South Cheshire College Student Paper	<1 %
36	Www.dovepress.com Internet Source	<1 %
37	test.dovepress.com Internet Source	<1 %
38	epubs.surrey.ac.uk Internet Source	<1 %
39	Lafreniere, Philip. "Development of a Novel Framework for the Application of Signature Based Safeguards (SBS) to Pyroprocessing.", The University of New Mexico, 2018 Publication	<1 %
40	Submitted to University of Hong Kong Student Paper	<1 %

41	assets.researchsquare.com Internet Source	<1 %
42	core.ac.uk Internet Source	<1 %
43	Chen Fang. "Functionalized Nanoparticles with Long-Term Stability in Biological Media", Small, 03/30/2009 Publication	<1 %
44	researchbank.rmit.edu.au Internet Source	<1 %
45	ruj.uj.edu.pl Internet Source	<1 %
46	schapelleisstillinnocentaustralia.blogspot.com Internet Source	<1 %
47	D. Sathya Prabhu, V. Devi Rajeswari. " In vitro and in silico analyses of L. on Peroxisome proliferator-activated receptor gamma ", Journal of Cellular Biochemistry, 2018 Publication	<1 %
48	Huiyong Chen, Pyung-Soo Lee, Xueyi Zhang, Dan Lu. "Structure replication and growth development of three-dimensionally ordered mesoporous-imprinted zeolites during confined growth", Journal of Materials Research, 2013 Publication	<1 %

49	Submitted to John Paul College Student Paper	<1 %
50	Submitted to University of Warwick Student Paper	<1 %
51	digital.lib.washington.edu Internet Source	<1 %
52	eprints.uthm.edu.my Internet Source	<1 %
53	os.zhdk.cloud.switch.ch Internet Source	<1 %
54	www.nature.com Internet Source	<1 %
55	Blaz Jelenc. "GENERATING UNIFORM MAGNETIC FIELDS IN TWO DIMENSIONAL POLYGONAL REGIONS", IEEE Transactions on Magnetics, 2020 Publication	<1 %
56	Yang Guangzhi, Bo Chen, Wenqing Zhao, Minghao Xu, Yang Lu, Yuhua Xue, Hui-Juan Zhang. "Nitrogen, Sulfur and Fluorine Tri-Doped Carbon Supporting Cobalt Nanoparticles for Oxygen Reduction Catalysis", Journal of The Electrochemical Society, 2022 Publication	<1 %
	ir.kluniversity.in	

57	Internet Source	<1 %
58	lib.buet.ac.bd:8080 Internet Source	<1 %
59	www.teamhagkull.com Internet Source	<1 %
60	escholarship.org Internet Source	<1 %
61	studentsrepo.um.edu.my Internet Source	<1 %
62	toyama.repo.nii.ac.jp Internet Source	<1 %
63	wrap.warwick.ac.uk Internet Source	<1 %
64	www.frontiersin.org Internet Source	<1 %
65	G. R. Hearne, L. Kapesi, R. M. Erasmus, S. R. Naidoo, R. Warmbier. "Effects of light-ion low-fluence implantation on the pressure response of double-walled carbon nanotubes", Physical Review Materials, 2021 Publication	<1 %
66	Thakkar, Bhumi. "Isolation, Culture and Characterization of Insect Cell Line for In-Vitro	<1 %

http://www.frontiersin.org

	Screening of Insecticides.", Maharaja Sayajirao University of Baroda (India), 2021 Publication	
67	Ye, Ruquan. "Nanomaterials in Diverse Dimensions: Synthesis, Properties and Applications", Rice University Publication	<1 %
68	ir.library.dc-uoit.ca Internet Source	<1 %
69	jci.org Internet Source	<1 %
70	jes.ecsdl.org Internet Source	<1 %
71	nanoscalereslett.springeropen.com Internet Source	<1 %
72	repository.kaust.edu.sa Internet Source	<1 %
73	tel.archives-ouvertes.fr Internet Source	<1 %
74	theses.gla.ac.uk Internet Source	<1 %
75	www.ema.europa.eu Internet Source	<1 %
76	www.freepatentsonline.com Internet Source	<1 %

77	www.science.gov Internet Source	<1 %
78	Han, . "Magnetic Properties of Solids", A Modern Course in the Quantum Theory of Solids, 2012. Publication	<1 %
79	Vashahri-Ghamsari, Saeid. "Quantum Dynamical Phenomena in Non-Hermitian and Magnomechanical Systems", University of Arkansas, 2021 Publication	<1 %
80	Wei Shi, Jin Huang, Ruochen Fang, Mingjie Liu. "Imparting Functionality to the Hydrogel by Magnetic-Field-Induced Nano-assembly and Macro-response", ACS Applied Materials & Interfaces, 2020 Publication	<1 %
81	Yuan Yuan, Changsheng Liu, Jingxiong Lu, Wei Tang, Qi Gan, Huanjun Zhou, Jiangchao Qian, Xun Lu. "In vitro cytotoxicity and induction of apoptosis by silica nanoparticles in human HepG2 hepatoma cells", International Journal of Nanomedicine, 2011 Publication	<1 %

Exclude quotes Off Exclude matches < 3 words

Exclude bibliography On